CRANFIELD UNIVERSITY

LUCA BRONDOLO

COMPARATIVE INVESTIGATION OF LARGE EDDY SIMULATION AND RANS APPROACHES FOR EXTERNAL AUTOMOTIVE FLOWS

SCHOOL OF ENGINEERING
MSc BY RESEARCH

MSc
Academic Year: 2009 - 2011

Supervisor: EVGENIY SHAPIRO
JULY 2011

CRANFIELD UNIVERSITY

SCHOOL OF ENGINEERING
MSc BY RESEARCH

MSc

Academic Year 2009 - 2011

LUCA BRONDOLO

COMPARATIVE INVESTIGATION OF LARGE EDDY SIMULATION AND RANS APPROACHES FOR EXTERNAL AUTOMOTIVE FLOWS

Supervisor: EVGENIY SHAPIRO

JULY 2011

ABSTRACT

This thesis investigates the accuracy and scalability of RANS and LES approaches applied to external automotive aerodynamics. Due to the availability of considerable experimental and computational data available on the Ahmed body, this reference model was chosen for this study. The relative simple geometry of the Ahmed body model is able reproduce the common flow features of a hatch back style vehicle. The 25° slant angle configuration was used as it is a major challenge in terms of flow prediction. The RANS model used included the Standard K-ε, RNG K-ε, Realizable k-ε and K-ω SST. The LES simulations were run with the Smagorinsky-Lilly SGS model. Three grids with different level of refinement were generated. A viscous hybrid mesh approach was used for all the simulations. This type of mesh is commonly used by automotive manufactures and motorsport organizations. The commercial package Fluent 12 was used as a solver.

The K-ω SST and LES models showed good agreement with the experimental data. LES in particular was the only model to predict flow re-attachment over the slant angle as seen on the experimental and computational data available in literature. The richness of the unsteady data available from the LES simulations and correct interpretation of flow topology balance in part the major computational requirements compared to the RANS models. Taking into account the hardware resources available to automotive manufactures, the LES is suitable to be part of the design process.

Keywords:

Automotive,CFD, Turbulence

ACKNOWLEDGEMENTS.

I would like to thank Evgeniy Shapiro at Cranfield University for supervising the project and for his valuable help and feedback throughout the lengths of this MSc. In addition, I would like to thank Adrian Gaylard at Jaguar Land Rover for all his useful advice. Finally, a big thank you goes to my parents and my wife Vanessa for their support throughout the lengths of this MSc.

TABLE OF CONTENTS

LIST OF FIGURES

LIST OF TABLES

NOMENCLATURE

Acronyms

Cd	Drag coefficient
Cl	Lift coefficient
Cp	Pressure Coefficient
Re	Reynolds Number
DNS	Direct Numerical Simulation
LES	Large Eddy Simulation
RANS	Reynolds Average Navier Stokes
STD	Standard K-ε model
RKE	Realizable K-ε model
K-O SST	K-ω Shear Stress Transport model

MUSCL	Monotomic Upwind Sheme for Scalar Conversion Laws
CFL	Courant-Friedrichs-Lewy number
FFT	Fast Fourier Transform
TKE	Turbulent Kinetic Energy
SGS	Sub Grid Scale model
CPU	Central Processing Unit

Greek symbols

ε	Dissipation Rate
λ_T	Taylor micro-scales
η	Small dissipative scale of turbulence motion
ρ	Density
v	Kinematic viscosity
μ	Dynamic viscosity
γ	Ratio of specific heat
τ_{ij}	Viscous stress
τ_n	Kolmogorov time scale

Latin Symbols

l	Integral length scale
E	Total energy
p	Pressure
G_b	Term representing the buoyancy effects

G_k	Generation of turbulent kinetic energy
G_v	Generation of turbulent viscosity
G_ω	Generation of specific dissipation rate
s_{ij}	Stress sensor
S_ω	Source term
U_∞	Freestream velocity
$\mathbf{u}$	Velocity vector
u	Velocity components in x cartesian direction
U'	Fluctuating velocity
Y_k	Dissipation of K
Y_ω	Dissipation of ω

1 Introduction

1.1 Motivation and Objectives

Around 1920 engineers were already applying aerodynamic concepts gained from the aircraft sector to road going vehicles. An example of this was a vehicle known as Tropfenwagen developed by an Austrian aircraft engineer called Edmund Rumpler. The Tropfenwagen was presented at the 1921 Berlin car show. Unusually this vehicle was designed around an aerofoil shape in its plan view contrary to the more common low drag designs where the aerofoil shape was used for the side profile of the vehicle. The efficiency of this design was proved several years later at the VW wind tunnel in 1983, the Topfenwagen obtained a claimed Cd of 0.28 which is quite low also by today's standard. During the 1930s other automotive manufacturers such as Chrysler in America and Tatra in Western Europe were also pushing the boundaries of automotive aerodynamics. Although aerodynamically efficient the unusual shapes of low drag vehicles had a negative impact on their commercial success. The vehicles mentioned above were only rare attempts at producing low drag road vehicles. Automotive manufactures were more interested in creating vehicles with more conservative shapes relatively easy to mass produce. Their main concern was to increase car sales by producing good looking vehicle at affordable prices. It was not until the oil crises of the 1970s that the automotive industry started to focus on vehicle aerodynamics with the aim of producing more efficient vehicle shapes able to reduce drag and hence reducing fuel consumption.

Wind tunnel testing became a crucial element in understanding vehicle aerodynamics and although common wind tunnels used in aeronautics could be adapted for vehicle testing, these started to show several limitations when used for automotive testing. Aeronautic wind tunnels were built to generate uniform flow with low turbulence levels, this was needed in order to simulate flight aerodynamics at high altitude. This was not needed for automotive flow as the turbulence level for ground vehicles tends to be high. Aeronautical bodies tend to be streamlined and they generate a considerable amount of lift which tends

to bend the flow inside the tunnel. Ground vehicles are often not streamlined and by generating flow separation they have the tendency to block the wind tunnel's flow. Due to these differences, automotive manufactures started to build wind tunnels dedicated exclusively to automotive aerodynamic testing. The constant improvements of data acquisition and flow visualization technique were then translated in a better understanding of flow phenomena associated with ground vehicles aerodynamics.

Road vehicles can be considered as bluff bodies. Due to adverse pressure gradients and loss of kinetic energy the flow separates and in some regions re-attaches to the surface of the vehicle. As shown in Figure 1-1 the flow separates at the front edge of the bonnet and re-attaches on the bonnet surface. The flow stays attached over the bonnet and separates where the bonnet meets the windscreen. The flow then re-attaches over the windscreen. These separations are often called quasi-two-dimensional as the vortices' axes are parallel to the separation line. Around the A-pillar and C-pillar regions the flow separation creates cone-like vortices. This type of separation is fully three dimensional.

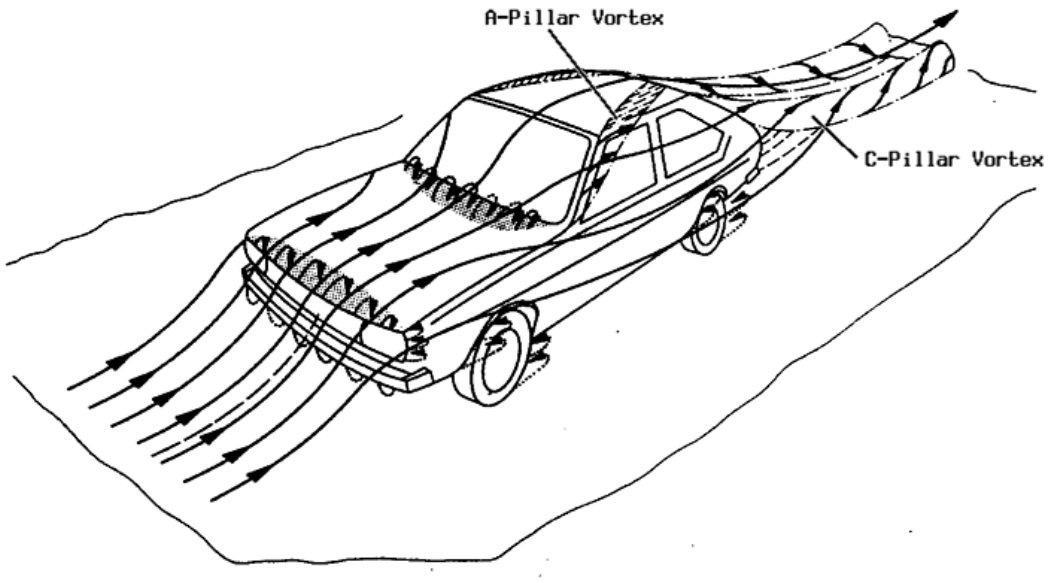

Figure 1-1: Flow topology for a generic vehicle shape after Hucho [1].

Considering the pressure distribution around a generic vehicle shape (figure 1-2) it can be stated that at the front of the vehicle, the Cp value of 1 indicates that there is a stagnation point. The acceleration of the flow over the bonnet makes the pressure coefficient drop until it becomes negative (favourable pressure distribution). Around the windshield the velocity of the flow decreases while the pressure coefficient increases (unfavourable pressure distribution). On the roof, as on the bonnet, the flow accelerates again and the pressure coefficient drops. Towards the end of the vehicle the velocity of the flow decreases and the pressure coefficient increases toward the value of 0. The Cp value is not able to reach the original value of 1 because the flow separates at the end of the vehicle. The non total recovery of the pressure value due to flow separation is responsible for creating form drag.

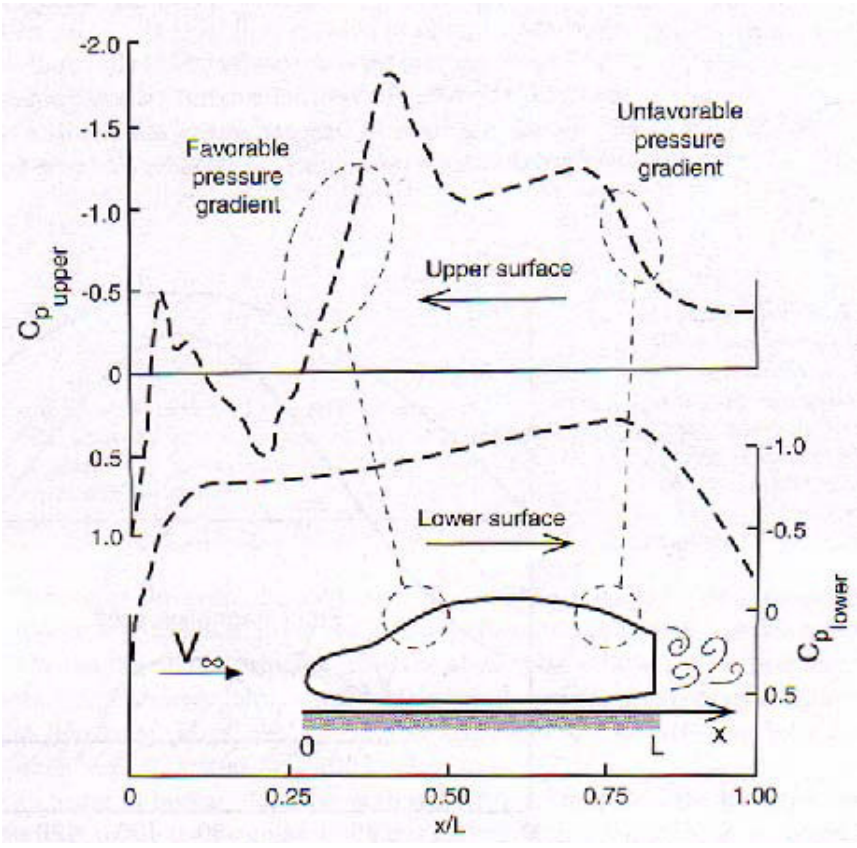

Figure 1-2 Pressure coefficient distribution after Katz [2].

Kleber [3] showed an example of how to integrate CFD into the design process of a car. The complete external surfaces with a simplified underbody of an Opel Astra were simulated using the commercial CFD package Fluent V5 and using the Realizable K-ε turbulence model. The simulation showed a drag coefficient deviation of about 5-10% from wind tunnel data. The study did not show deviation for Cl but the author gives the impression that the figures are far off from the experimental data. The simulation accurately predicted the delta Cd between two geometry changes.

Drage et al [4] used the RSM model in order to evaluate the variation of drag and lift coefficient of BMW X3 vehicle. The CFD software used was Fluent and the experimental tests were performed at the GIE S2A in Paris and at the FIAT wind tunnel in Italy. The vehicle was tested with three different spoiler positions. The simulations were able to predict the drag and lift variation between the different spoiler positions. The authors also mentioned that the absolute values of drag, lift and moments coefficients were also well predicted.

A study conducted by PSA Peugeot Citroen and ANSYS/Fluent France [5] showed the superiority of the LES model against the common RANS method. The model of a simplified Citroen C5 (1/5 scale) was tested in the PSA scale wind tunnel at different yaw angles. The CAD model of the vehicle was used for the CFD simulations. Two volume meshes of around 35 million and 65 million elements were used for the LES and RANS simulations. The RANS model used was the Realizable K-ε. The LES model showed better prediction of aerodynamic forces and moment when compared to the RANS simulations. The Fourier transform analysis of the pressure signal showed a peak frequency very close to the experimental data. The study also showed the applicability of LES in the automotive environment by comparing the hours of computation between the simulations. It was found that when using the coarse grid 26 hours were required for the RANS simulation and 150 hours for the LES simulation. It should also be taken into account that the LES was initialized from a previous RANS simulation.

Large Eddy Simulation has been the subject of academic research for decades now but is rarely adopted in industrial applications. Although the previous study [5] showed LES applied to external automotive aerodynamics, grid resolution and solving time are still limiting the diffusion of LES in the automotive environment. However, the increased computer power available to automotive and motorsport manufactures and the availability of LES on commercial codes such as Fluent might create a departure from the well established RANS approach.

The aim of this research project is to investigate the accuracy and scalability of the RANS and LES approaches applied to external automotive aerodynamics. The automotive test case to be used is the Ahmed model due the high amount of experimental and computational data literature available. Although this geometry is very simple when compared to real car geometry, the flow separation along its backlight angle creates a great challenge in terms of flow prediction. Specifically in the 25° slant angle configuration the standard RANS approach seems unable to reproduce the complex flow topology on the slanted surface. LES give more promising results but at higher computational costs. Due to this the Ahmed body in the 25° angle configuration variant was selected for this study.

More specifically the objectives are:

- To assess the performance of the RANS and LES approaches using the commercial software Fluent 12 against experimental and CFD data available in literature.
- To evaluate the flow prediction of the RANS and LES models against experimental and CFD data.
- To evaluate the computational costs associated with the RANS and LES simulations.

1.2 Turbulence and its modelling

1.2.1 Turbulence

In nature there exists two types of flow: laminar and turbulent. Towards the end of the eighteen hundreds Osborne Reynolds [6] studied the transition between laminar and turbulent flow through practical experiments. Using simple visualization technique such as dye in water flow he observed that at low velocity the dye formed a layer parallel to the surface of the tube. After gradually increasing the velocity he observed that at a certain point the flow behaviour drastically change. The dye did not follow the tube surface anymore but it showed a chaotic motion.

The Reynolds number, named after Osborne Reynolds is a number equal to the ratio between inertial and viscous forces. Experimentally it is possible to observe that the fluid changes behaviour above or below a certain Reynolds number (critical Reynolds number). For low Reynolds number, below the critical Reynolds number, the flow smoothly follows the wall surfaces. The flow properties do not change over time so the flow is also called steady. At higher Reynolds number (above the critical Reynolds number), the fluid particles will tend to have a random and chaotic motion which cannot be described as function of time and space. This type of fully unsteady fluid motion is called turbulent flow. Automotive aerodynamics deals with high Reynolds number, generally speaking over 1×10^6. Due to this the aerodynamics of road vehicles, as with most of the engineering disciplines, deals with turbulent flows.

Turbulent flows are composed by a wide range of rotational structures typically called eddies. Richardson [7] introduced the concept of energy cascade in order to describe the behaviour of the turbulent eddies. According to Richardson the local Reynolds number of largest eddies is comparable to the global Reynolds number of the flow. This happens because the characteristic velocity and length of the largest eddies is the same order of magnitude as the velocity and length scale of the mean flow. Due to their interaction with the mean flow, the large eddies are broken down into smaller eddies so that the kinetic energy is

transferred from larger eddies to smaller eddies. The process is continuously repeated until the smallest eddies are completely dissipated into heat.

The studies conducted by the Russian scientist Kolmogorv [8] showed consistency with Richardson's energy cascade hypothesis. In addition, his work gave a more detailed insight into the scales of turbulence energy transfer. Kolmogorov stated that at high Reynolds number the small scales of turbulence are isotropic formulated. Their behaviour is uniquely dependent on the viscosity ν and energy dissipation rate ε. Due to the work carried out by Kolmogorov the smallest scales of turbulence are called Kolmogorov microscales. Length, time scales and velocity of the Kolmogorov microscales can be expressed as follows [9]:

Length scale ratio $\frac{\eta}{\ell} \approx Re_{\ell}^{3/4}$ (1.1)

Time scale ratio $\frac{\tau}{T} \approx Re_{\ell}^{-1/2}$ (1.2)

Velocity scale ratio $\frac{\upsilon}{\vartheta} \approx Re_{\ell}^{-1/4}$ (1.3)

Kolmogorov also stated that the behaviour of the intermediate scales (between η and ℓ) can be expressed as a function of the energy dissipation rate ε. He also determined that the energy spectrum of these length scales (called inertial subrange) is equal to [9]:

$$E(k) = \alpha k^{-5/3} \varepsilon^{2/3} \quad (1.4)$$

1.2.2 Numerical approaches to turbulence

Due to its random nature and complexity, at present there does not exist a definitive theory on turbulence. Over the years different numerical methods have been developed to deal with turbulence. At present the most well known numerical approaches are: RANS, LES, and DNS. All the models are based on the Navier Stokes equations which are a set of non linear partial differential equations which describe the motion of fluids. Considering an incompressible

flow with constant viscosity, these set of equations can be expressed as follows [9]:

$$\operatorname{div} \mathbf{u} = 0 \tag{1.5}$$

$$\frac{\partial u}{\partial t} + \operatorname{div}(u\mathbf{u}) = -\frac{1}{\rho}\frac{\partial p}{\partial x} + \nu \operatorname{div}\big(\operatorname{grad}(u)\big) \tag{1.6}$$

$$\frac{\partial v}{\partial t} + \operatorname{div}(v\mathbf{u}) = -\frac{1}{\rho}\frac{\partial p}{\partial x} + \nu \operatorname{div}\big(\operatorname{grad}(v)\big) \tag{1.7}$$

$$\frac{\partial w}{\partial t} + \operatorname{div}(w\mathbf{u}) = -\frac{1}{\rho}\frac{\partial p}{\partial x} + \nu \operatorname{div}\big(\operatorname{grad}(w)\big) \tag{1.8}$$

Where **u** is the velocity vector and *u,v,w* are its x-y-z components. Equation 1.5 is the continuity equation, equations 1.6, 1.7 and 1,8 are the x-momentum, y-momentum and z-momentum equations.

1.2.2.1 RANS

Turbulence is an unsteady, time dependent phenomena but in RANS (Reynolds Avarage Navier Stokes) the Navier Stokes equation are time averaged or ensemble averaged in flows where time dependent boundary conditions apply [9]. The set of RANS equations are obtained by applying Reynolds decomposition and time averaging to the Navier Stokes equations. The flow variables are decomposed into mean and fluctuating components:

$$\mathbf{u} = \mathbf{U} + \mathbf{u}' \; ; \; u = U + u' \; ; \; v = V + v' \; ; \; w = W + w' ; \; p = P + p' \tag{1.9}$$

After applying Reynolds decomposition and time averaging to the equations 1.5, 1.6, 1.7 and 1.8, the following equations are then obtained:

$$\operatorname{div} \mathbf{U} = 0 \tag{1.10}$$

$$\frac{\partial U}{\partial t} + \mathrm{div}(U\mathbf{U}) = -\frac{1}{\rho}\frac{\partial P}{\partial x} + \nu\,\mathrm{div}\big(\mathrm{grad}(U)\big) + \frac{1}{\rho}\left[\frac{\partial(-\rho\overline{u'^2})}{\partial x} + \frac{\partial(-\rho\overline{u'v'})}{\partial y} + \frac{\partial(-\rho\overline{u'w'})}{\partial z}\right] \quad (1.11)$$

$$\frac{\partial V}{\partial t} + \mathrm{div}(V\mathbf{U}) = -\frac{1}{\rho}\frac{\partial P}{\partial y} + \nu\,\mathrm{div}\big(\mathrm{grad}(V)\big) + \frac{1}{\rho}\left[\frac{\partial(-\rho\overline{u'v'})}{\partial x} + \frac{\partial(-\rho\overline{v'^2})}{\partial y} + \frac{\partial(-\rho\overline{u'w'})}{\partial z}\right] \quad (1.12)$$

$$\frac{\partial W}{\partial t} + \mathrm{div}(W\mathbf{U}) = -\frac{1}{\rho}\frac{\partial P}{\partial z} + \nu\,\mathrm{div}\big(\mathrm{grad}(W)\big) + \frac{1}{\rho}\left[\frac{\partial(-\rho\overline{u'w'})}{\partial x} + \frac{\partial(-\rho\overline{v'w'})}{\partial y} + \frac{\partial(-\rho\overline{w'^2})}{\partial z}\right] \quad (1.13)$$

The averaging of turbulent fluctuation creates six additional terms $(-\rho\overline{u'^2}, -\rho\overline{v'^2}, -\rho\overline{w'^2}, -\rho\overline{u'v'}, -\rho\overline{u'w'}, -\rho\overline{v'w'})$ called Reynolds stresses. The Reynolds stresses have to be modelled by using turbulence models such as the Spallart-Allmaras, K-ε, K-ω and RSM models. Computational inexpensive when compared to DNS or LES, RANS is still the most common turbulence approach in engineering applications especially when these deal with high Reynolds number flow. This method is the most common approach when dealing with external automotive aerodynamics.

1.2.2.2 LES

LES can be seen as an intermediate step between RANS and DNS. LES maintains the unsteady form of the Navier Stokes and thanks to spatial filtering operations, the larger eddies are separated from the smaller eddies. The large eddies are then solved directly while the effect of the smaller eddies has to be modelled by using a Sub Grid Scale model.

The most common filtering functions are [9]:

Top hat filter:

$$G(\boldsymbol{x}, \boldsymbol{x}', \Delta) = \begin{cases} \frac{1}{\Delta^3} & |\boldsymbol{x} - \boldsymbol{x}'| \leq \Delta/2 \\ 0 & |\boldsymbol{x} - \boldsymbol{x}'| > \Delta/2 \end{cases} \tag{1.14}$$

Gaussian filter:

$$G(\boldsymbol{x}, \boldsymbol{x}', \Delta) = \left(\frac{\gamma}{\pi\Delta^2}\right)^{3/2} \exp\left(-\gamma \frac{|\mathrm{x} - \mathrm{x}'|^2}{\Delta^2}\right) \tag{1.15}$$

Spectral cut-off:

$$G(\boldsymbol{x}, \boldsymbol{x}', \Delta) = \prod_{i=1}^{3} \frac{\sin\left[\frac{x_i - x'_i}{\Delta}\right]}{(x_i - x'_i)} \tag{1.16}$$

Where G is the filtering function and Δ is the cut off width. After filtering the unsteady Navier Stokes equations, the following LES momentum equations are obtained [9]:

$$\frac{\partial(\rho\bar{u})}{\partial t} + \mathrm{div}(\rho\bar{u}\bar{\mathbf{u}}) = \\ = -\frac{\partial\bar{p}}{\partial x} + \mu\,\mathrm{div}\big(\mathrm{grad}(\bar{u})\big) - (\mathrm{div}(\rho\overline{u\mathbf{u}}) - \mathrm{div}(\rho\bar{u}\,\bar{\mathbf{u}})) \tag{1.17}$$

$$\frac{\partial(\rho\bar{v})}{\partial t} + \mathrm{div}(\rho\bar{v}\bar{\mathbf{u}}) = \\ = -\frac{\partial\bar{p}}{\partial y} + \mu\,\mathrm{div}\big(\mathrm{grad}(\bar{v})\big) - (\mathrm{div}(\rho\overline{v\mathbf{u}}) - \mathrm{div}(\rho\bar{v}\,\bar{\mathbf{u}})) \tag{1.18}$$

$$\frac{\partial(\rho\bar{w})}{\partial t} + \mathrm{div}(\rho\bar{w}\bar{\mathbf{u}}) = \\ = -\frac{\partial\bar{p}}{\partial z} + \mu\,\mathrm{div}\big(\mathrm{grad}(\bar{w})\big) - (\mathrm{div}(\rho\overline{w\mathbf{u}}) - \mathrm{div}(\rho\bar{w}\,\bar{\mathbf{u}})) \tag{1.19}$$

The last terms in the three equations arise due to the filtering operations. Using the suffix notations, these terms can be expressed as follow [9]:

$$\mathrm{div}\left(\rho\overline{u_i\mathbf{u}}\right) - \mathrm{div}\left(\rho\overline{u_i}\,\overline{\mathbf{u}}\right) = \frac{\partial\tau_{ij}}{\partial x_j} \tag{1.20}$$

where $\tau_{ij} = \rho\overline{u_i u_j} - \rho\overline{u}_i\overline{u}_j$ (1.21)

τ_{ij} is the sub-grid-scale-stress which has to be modelled using a Sub Grid Scale (SGS) model. The Smagorinksy-Lilly is probably the most well known SGS model. Computationally more expensive than RANS but definitely more affordable than DNS, LES has acquired popularity in recent years due to the exponential rising of computer power available to industries and universities.

1.2.2.3 DNS

In DNS (Direct Numerical simulation) the unsteady Navier Stokes equation are solved directly. DNS aims to resolve all the eddies up to the Kolmogorov micro scales. In order to do that, the mesh resolution has to satisfy the kolmogorov length scale ratio of $Re^{9/4}$ (considering a three dimensional domain).This means that a typical automotive flow problem (Re around 10^6) would require around $10^{27/2}$ grid points. The time step required is also limited by the Kolmogorov length scale ratio so for a Re = 10^6, the simulation should be run for at least 10000 time steps [9]. Due to these factors the computational requirements are prohibitive for external automotive aerodynamics. At present it is mostly an academic tool used to resolve low Reynolds number flow.

1.3 Literature Review

1.3.1 Ahmed's experimental investigation

By using a simplified vehicle body shape and extensive wind tunnel testing S.R. Ahmed et al [10] demonstrated how form drag is dependent from the rear slant angle of the vehicle. The model tested was based on the simplified vehicle geometry used by Morel a few years earlier in 1978. This was a highly simplified vehicle body shape with no wheels and has some resemblance of a hatch back

vehicle configuration. The Ahmed's version had more similar car dimensions. This bluff body was designed to have attached flow over the front part of the geometry and separated flow over the rear (depending on the slant angle used) with a wake generation similar to the one created by the more complex vehicle geometries.

The model had interchangeable rear ends ranging from 0 to 40° with 5 degree increments. The overall dimensions were a length of 1.044 m, a width of 0.389 m and a height of 0.288 m.

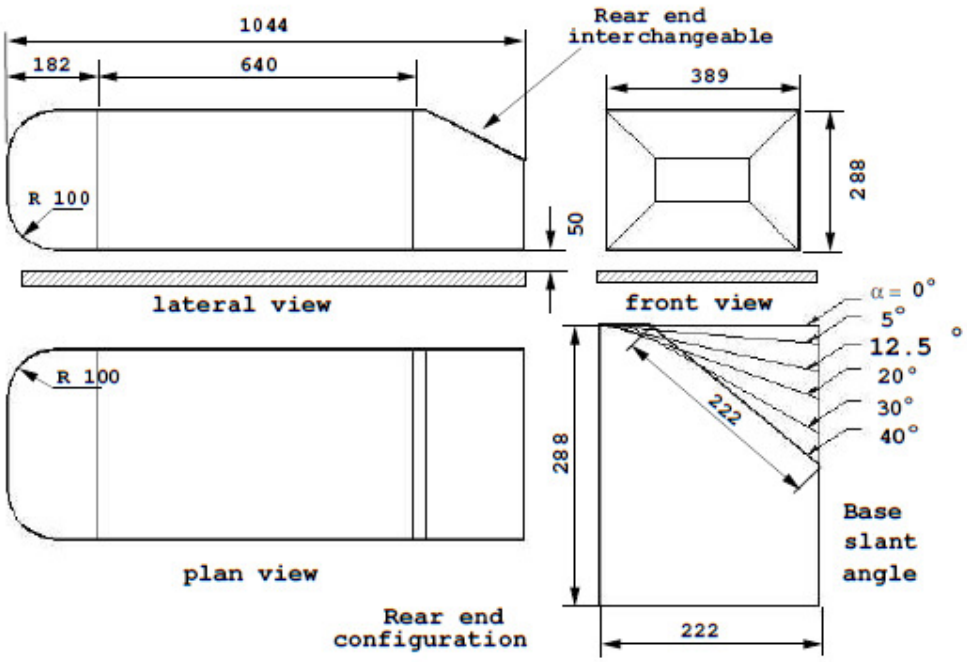

Figure 1-3: Ahmed body geometry specifications [10]

Two subsonic wind tunnels were used for this experiment. Both tunnels had an open test section having a test section length of around 5.8 m. The Braunschweig wind tunnel was used for pressure measurement and flow visualization while the Gottingen tunnel was used for wake survey and pressure measurements.

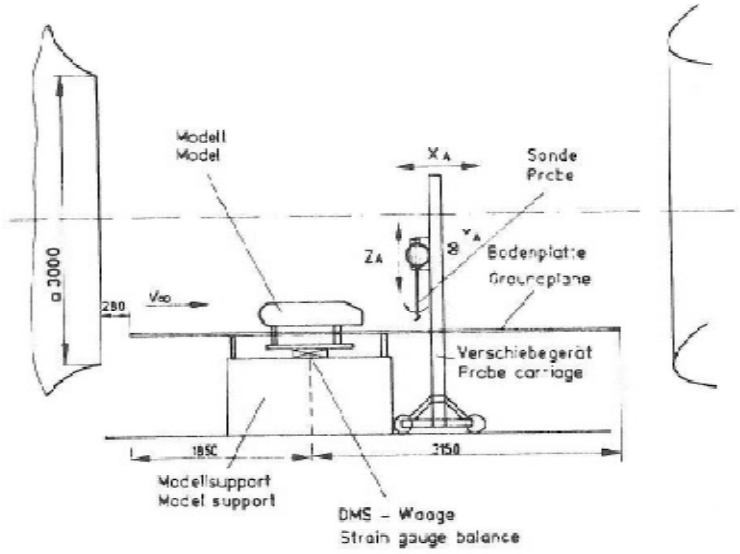

Figure 1-4: Experimental set-up [10].

The model was mounted 50 mm above the ground standing on 4 cylinders. All the different combinations of rear slant were tested with an air speed of 60 m/s. Various pressure readings were obtained along the body and oil flow techniques were adopted in order to visualize flow separation and vortex generation. A directional probe was also used to investigate the rear wake flow. Force measurements were obtained by a strain gauge balance connected to the model by the four cylindrical supporting struts. The drag values were recorded for each of the tested angles in order to analyze the drag contribution of the different rear angle configurations adopted. Lift data was not recorded. The model was also equipped with pressure taps for three different slant angle configurations (5°, 12.5°, 30°). The pressure taps were evenly distributed over one half of the model.

As for the flow around a generic vehicle, the flow stagnates at the front of the vehicle; it then accelerates over the edges and reaches a constant velocity over the top surfaces. The flow then accelerates towards the edge of the back light angle and depending on rear slant angle adopted it eventually separates.

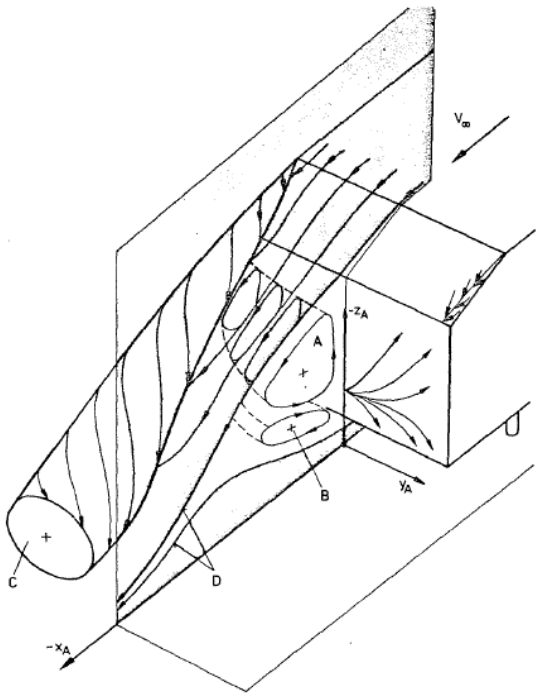

Figure 1-5: Ahmed body rear flow structure [10]

There are two region of flow recirculation (A and B) located at the rear of the model. These seem to be generated by the two horseshoe vortex D. The separation of the shear layer at the edge of the slant angles form the longitudinal vortex C, the intensity of this vortex is determined by the rear slant angle as described in the previous section. Ahmed's noticed that the strength of vortex A depends on the strength of vortex C. So both vortices are strictly correlated to the slant angle used. Consequently the Ahmed model is able to generate different flow behaviour based on the slant angle adopted. In particular the wind tunnel experiments showed substantial changes as a result of the slant angle being below and over 12.5° and below and over 30° Due to this the two angles are often called critical angles. Between 0 and 12.5° the flow remains attached over the rear end. The flow is mainly two dimensional but tends to be three dimensional on the side edges due to the presence of two longitudinal counter rotating vortices. The intensity of these vortices increases as the slant angle increases and due to this the flow became fully three dimensional over 12.5°. At around 25° the vortices are responsible for maintaining attached flow over a portion of the backlight. At this angle the flow separates slightly from the

backlight but re-attaches towards the end of the slant angle section. At 30° the flow is fully separated and the drag coefficient reaches the top value of 0.378 which is the highest of the entire slant angles tested. This high value is due to a pressure drop created by the separation bubble. Beyond this angle the flow is fully separated.

S.R. Ahmed [10] reported the drag coefficient over the three different body sections: front, rear slant end and rear vertical end. These areas are marked Ck, Cs and Cb on the drag breakdown table showed below:

Base slant angle φ	c_W	c_K^*	c_S^*	c_B^*
5^o	0.231	0.016	0.010	0.158
12.5^o	0.230	0.016	0.037	0.122
30^o (High Drag)	0.378	0.016	0.213	0.092
30^o (Low Drag)	0.260	0.019	0.089	0.101

Table 1-1: Ahmed body drag by part contribution

The table show that the total drag (Cw) is heavily influenced by the base slant angle mounted on the model. By analyzing the graph containing the drag coefficient for the different slant angles, the presence of the two critical angles previously described is evident.

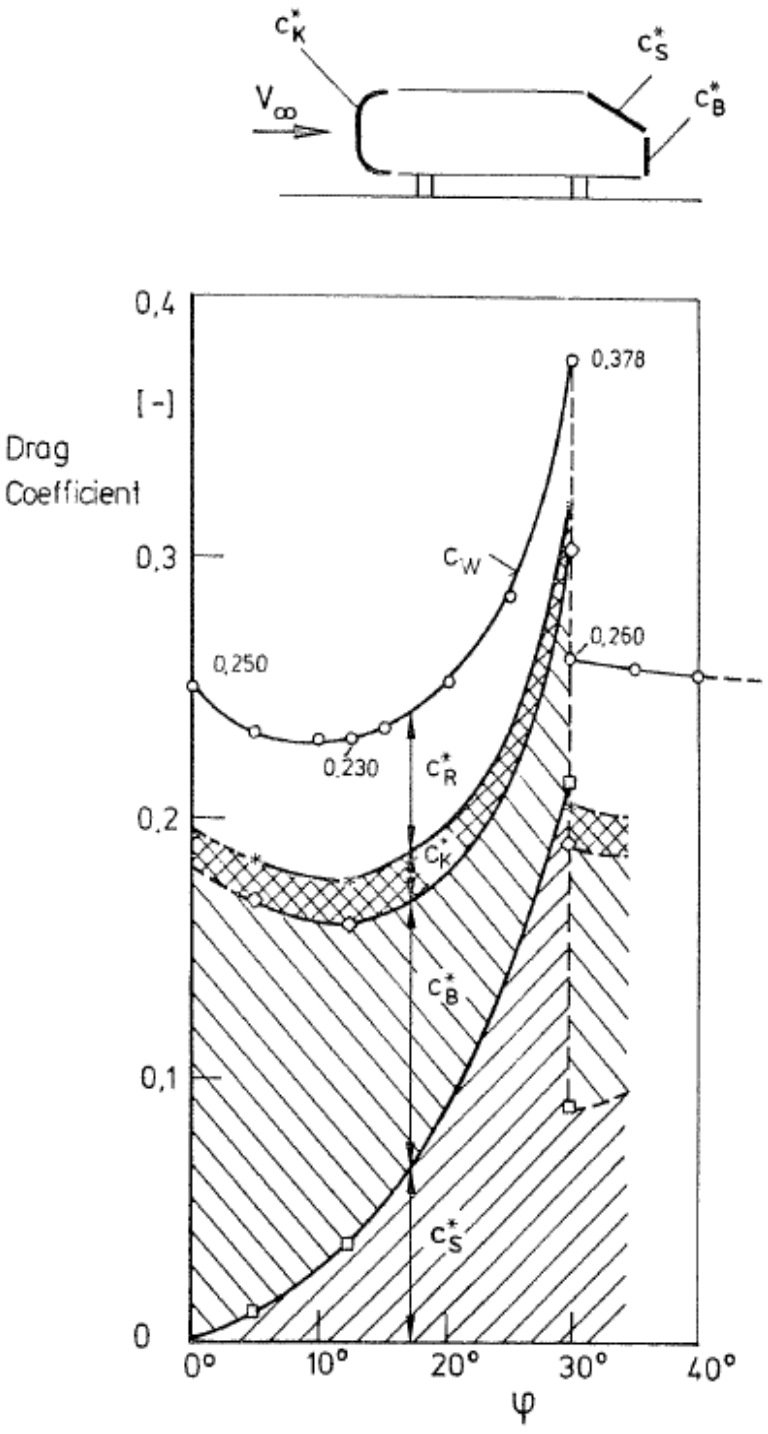

Figure 1-6: Variation of drag coefficient with slant angle adopted [10]

Starting from a value of 0,250 registered at a 0° slant angle the Cd decreases until it reaches its lowest value of 0.230 at 12.5°. After this angle the Cd starts to increase rapidly until it reaches the top value of 0.378 at 30°. After this angle the Cd drops returning the value to around 0,250. The graph shows two different Cd values at 30° as a low and high drag configurations were tested.

1.3.2 Further Ahmed body experimental investigations

A.Spohn and P.Gilleron [11] used a low speed water wind tunnel in order to study in detail the flow separation and flow structures on the Ahmed body. The tunnel used had a rectangular cross section of 0.5 x 0.25 m^2, the wind tunnel wall were made of transparent materials in order to enhance flow visualization. The flow speed used varied from 0.10 m/sec to 0.30 m/s.

The test conducted on the 25° configuration showed flow separation over the front part of the Ahmed body. This separation creates two Kelvin-Helmholtz type vortices.

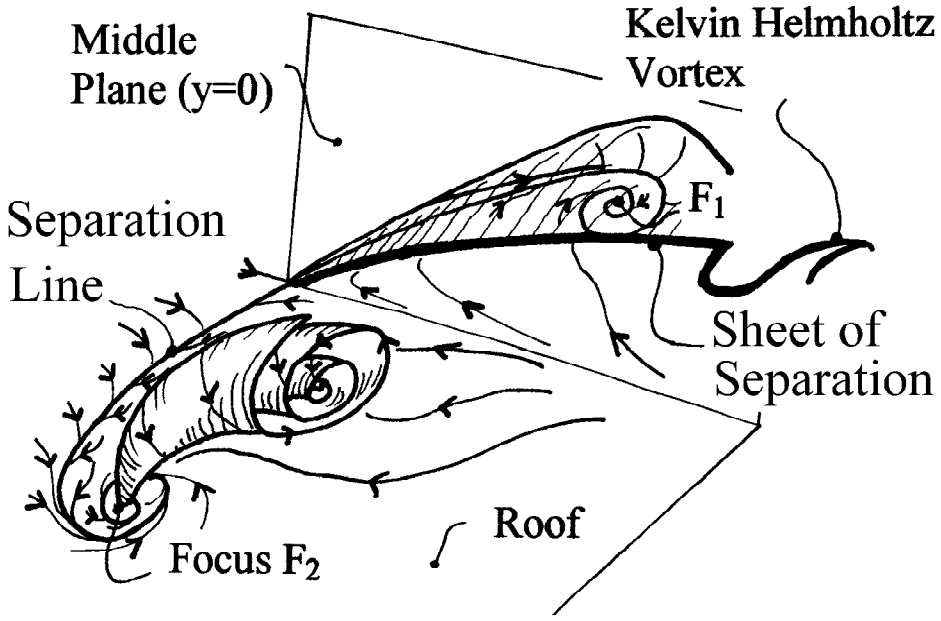

Figure 1-7: Kelvin Helmholtz vortices at the front of the Ahmed body [11]

The separation on the slant angle is more complex than the one originally described by Ahmed as shown in the figure 1-8:

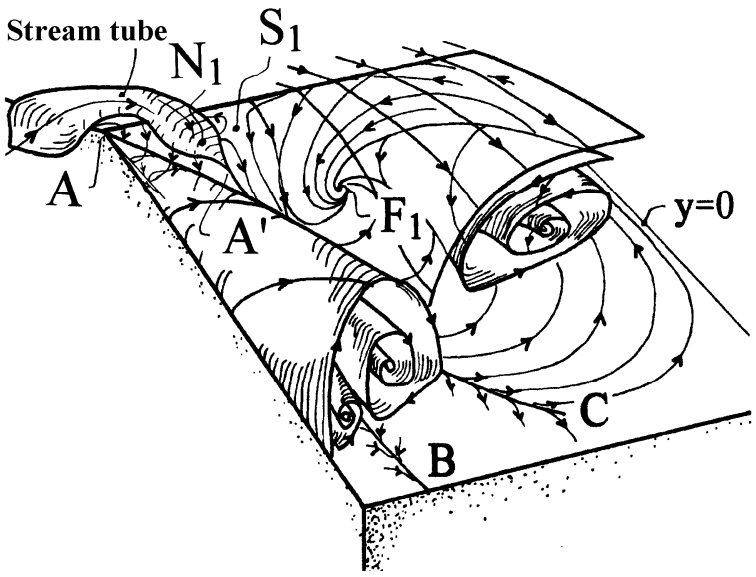

Figure 1-8: Flow structure over Ahmed body the slant angle [11]

The flow is highly unsteady, segment AC indicates the attachment line of the main vortex while segment AB indicates the separation line.

Lienhart and Becker et al. [12] tested the Ahmed body using a conventional wind tunnel. The aim of this study was to collect wind tunnel data which would be used to validate turbulence modelling techniques. This data is currently freely available online on various websites and most of the CFD validations of the Ahmed model are based on this data. The wind tunnel used was the Lehrstuhl für Strömungsmechanik (LSTM) with a 3/4 open test section configuration. The tunnel is able to generate wind speeds up to 55 m/s with turbulence intensity below 0.25%. For this experiment the measurement were obtained with a wind speed of 40 m/s. In the original work carried out by S.R Ahmed the wind speed was set to 60 m/s. The model was tested with two rear slant configuration, 25° and 35° respectively. These two angles were chosen as they are around the critical angle of 30° which is where the flow separation was detected by the Ahmed's experiment.

Laser Doppler Anemometry technology was extensively used for the wake survey of the two slant angle configurations. The measurements were extended to the full Ahmed body width, 21 different planes were used for the measurement grids giving 12,000 discrete measurement positions.

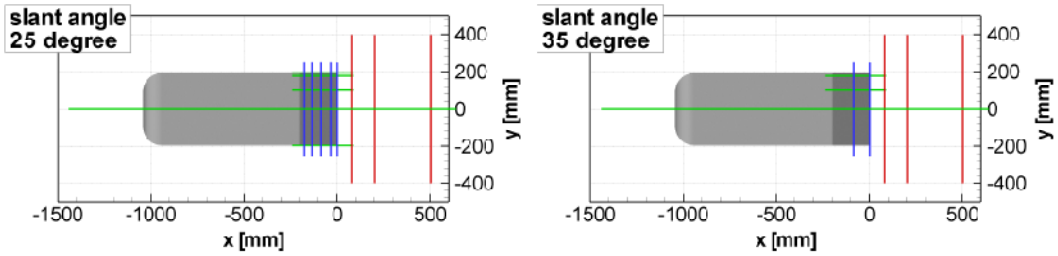

Figure 1-9: Measurement planes location [12]

Inlet boundary condition was also measured using an HWA probe. Velocity profiles upstream of the Ahmed body and on the slant angle were obtained with hot-wires measurements. The Ahmed body rear end was equipped with pressure taps for the two slant angle configurations. Around 500 pressure taps were distributed over one half of the model and a scanivalve system was mounted inside the model. Drag and lift values were not recorded.

The Ahmed's findings were confirmed in this experiment. By using flow visualization technique Lienhart and Becker clearly showed the flow difference between the 25° and 35° configurations:

Figure 1-10: Oil film visualization over the 25°(left) and 35°(right) slant angle [12]

The oil strakes on the 35° angle (right) configuration indicates that the flow is attached while the chaotic oil trace left on the 25° angle is due to flow separation which suggests the creation of the two counter rotating vortices described by Ahmed. Thanks to a two component LDA system Lienhart and Becker were able to demonstrate the presence of these two vortices.

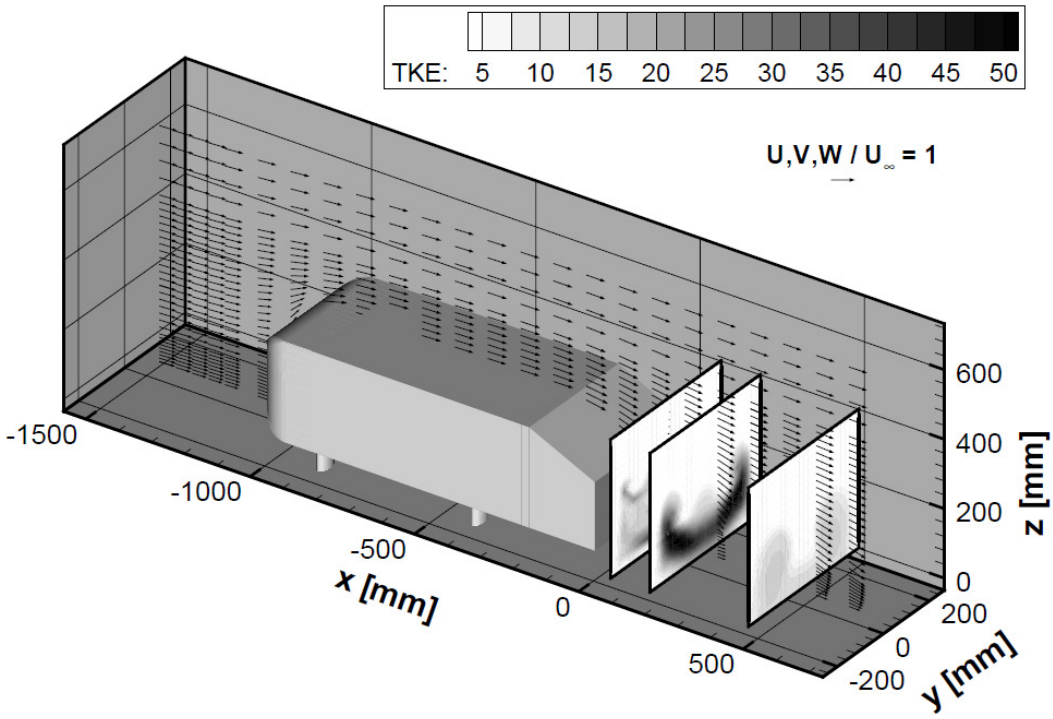

Figure 1-11: Turbulent Kinetic Energy plots behind the Ahmed body [12]

1.3.3 Ahmed body CFD investigations

The amount of experimental data available and the simplicity of the geometry made the Ahmed body an ideal test case for CFD studies. Several CFD codes and turbulence models have been tested based on Ahmed's models with the aim of validating the experimental data obtained from Lienhart and Becker. Due to this most of the CFD data available is for the 25° and 35° rear slant angles. It was common practices to model half of the Ahmed body without the supporting struts in order to significantly reduce the cell count. More recent studies

however have aimed to validate experimental studies with the full Ahmed's body modelled and meshed, supporting struts included.

P.Drage et al [4] performed both CFD simulations and wind tunnel testing (T.U Graz wind tunnel) on the Ahmed body with two rear slant angle configurations. The simulation was performed with the commercial code Fluent and by using the Reynold Stress Model. The mesh was developed with the meshing tool SPIDER. It consisted of 4 prism layers around the body and had an unstructured volume mesh giving a total cell count of 7.7 million cells. This type of meshing approach is very common in the automotive and motorsport sector as the time spent to create a structured grid around real vehicle shapes would prevent engineers from keeping the strict deadlines imposed by vehicle design cycles. For the 25° angle the wind tunnel experiment showed a drag coefficient of 0.299 and a lift coefficient of 0.345, while the CFD simulation gave 0.295 and 0.387 respectively. The RSM model showed an over prediction of the pressure coefficient over the slant angle, when compared to the pressure measurement taken by Lienhart and Becker [12].

S.Kapadia et al [13] conducted a CFD study on the Ahmed body with the 25° slant angle configuration using two different turbulence modelling approaches: Detached eddy simulation and one equation unsteady RANS model. An unstructured grid of 1.7 million cells was generated with Gridgen and COBALT was used as a solver. Although both models predict the presence of the counter rotating vortices, the DES showed a better representation of the unsteady structure at the trailing edge of the Ahmed body. The drag coefficient reached a constant value after approximately 3 seconds of simulation for both DES and RANS. DES showed an average Cd value of 0.2585 while with the RANS approach the drag the average Cd calculated is 0.3272. The simulation was run on a cluster with 256 CPUs, the average CPU time for DES was 6.4382 sec/iteration while for RANS it was 6.3188 sec/iteration.

G.Martinat et al [14] compared different turbulence modelling technique (URANS, DES, DDES) using the 25° slant angle configuration. URANS were also applied to the 35° case. A structured mesh composed of 3.6 millions

elements provided by Chalmers University was used for this study. During the URANS computation only half of the geometry was used. On the 35° configuration the RANS approach obtained mixed results. The Spalart-Allmaras and K-w SST provided a good comparison of U velocity profiles when compared to the experimental result of Lienhart. In the K-ε Chien case, the velocity profile was quite different from the experimental results. It seems that the flow detachment over the slant is overestimated by the K-ε Chien. All the URANS fail to provide good comparisons of velocity profiles using the 25° slant angle configuration. The authors indicated that this could be due to the overestimation of the eddy viscosity.

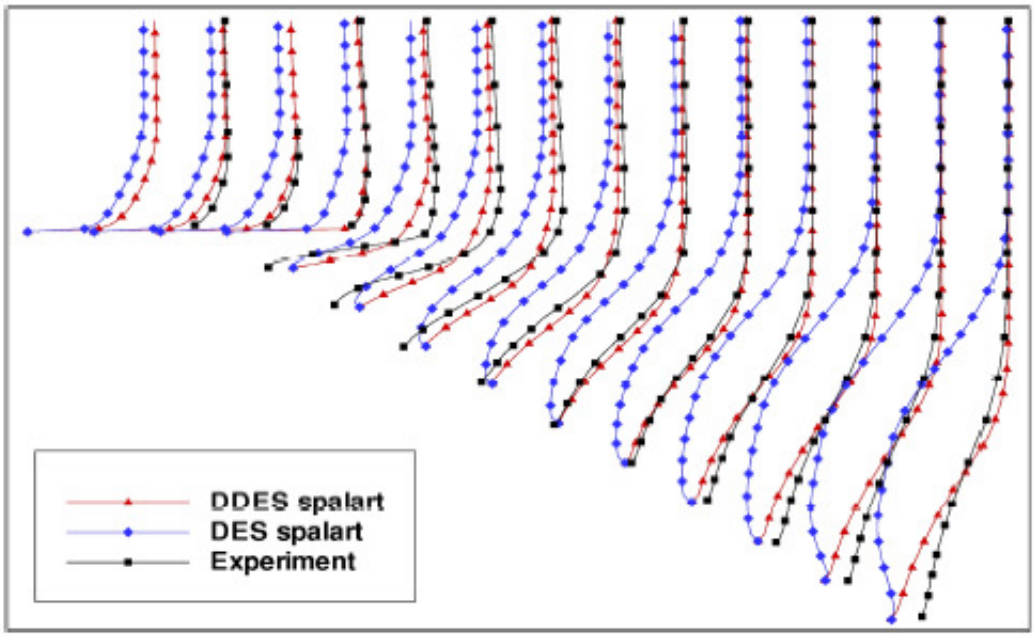

Figure: 1-12 U velocity profiles for the 25° slant angle configuration [14]

DES provided better U velocity profiles than URANS but it was still unable to create a good comparison with the experimental data probably due to the wall refinement used on the Ahmed body. The mesh given by Chalmers University was designed for LES so it was well refined along the wall boundaries. This problem was partially resolved by using a DDES approach. The Delayed Detach Eddy Simulation was designed to avoid the transition from URANS to LES in the shear layer.

C.Hinterberg et al [15] used LES to validate the experimental data of Lienhart and Becker. The solver used was a finite volume code and the commercial software ICEM-CFD was used to generate two structured meshes. The first mesh had cell counts of 8.8 million cells while the second more refined grid was built with 216 blocks reaching 18.5 million cells. A wall function approach similar to Werner Wengle was used for both meshes. The paper presented the results for the 25° slant angle configuration. Drag, lift and pressure coefficients were not reported. The separation and re-attachment of flow along the slope of the Ahmed body was not predicted by this computational study. This was probably due to a poor grid resolution near the wall boundaries. However, the LES was able to capture the main flow structures, the location of the counter rotating vortices is in good agreement with the experimental data. The U velocity profiles for the fine grid also showed good agreement with the experimental results.

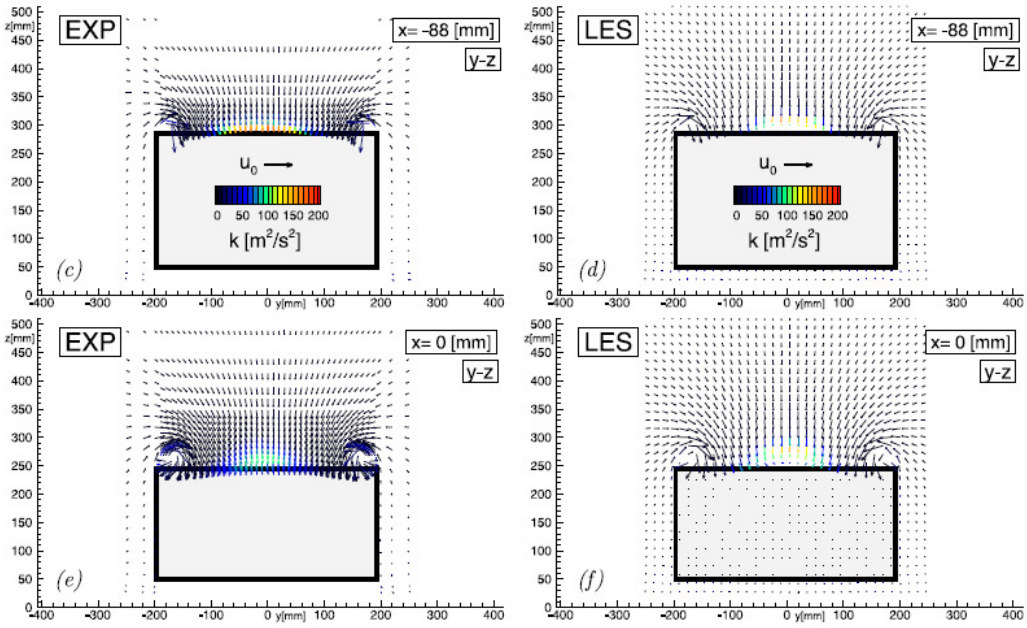

Figure 1-13 Mean velocity vectors coloured by Turbulent Kinetic energy [13]

Krajnovic' and Davidson [16,17] applied LES to the Ahmed body in the 25° configuration using three different mesh resolutions. The coarse, medium and fine grids had 3.5, 9.6 and 16.5 million elements respectively. No wall model was used. In order to reduce the computational requirements needed for LES,

the Reynolds number was reduced to 2 x 10^5. All three simulations were able to visualize flow separation at the front part of the Ahmed body and flow separation over a section of the rear slant angle. It was found that the size of the separation on the slant angle was dependent on the mesh resolution used. All three simulations gave good predictions of velocity profiles, the fine grid showed better agreement with wind tunnel data.

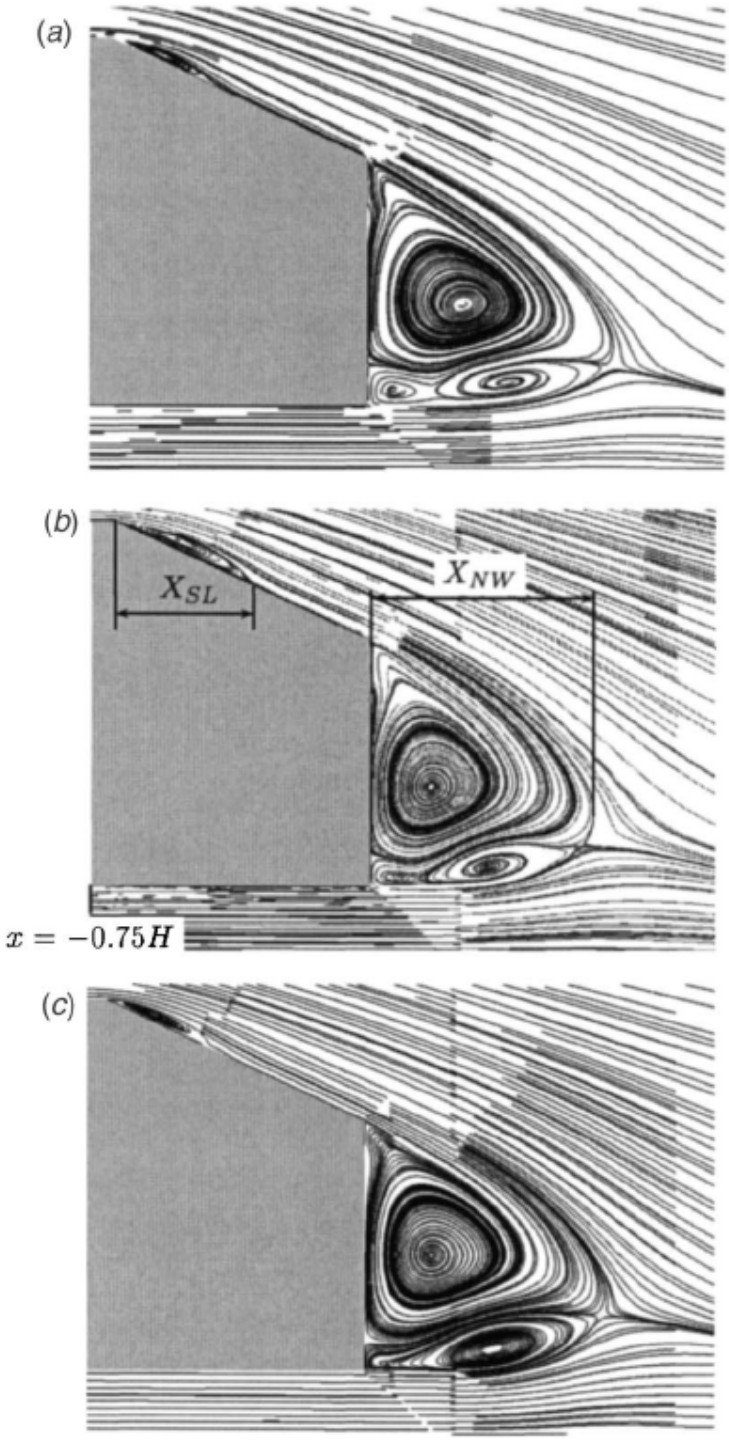

Figure 1-14: Time averaged streamlines on symmetry plane from coarse (top), medium (centre) and fine grid (bottom) [15]

2 Methodology

2.1 SIMPLE

For a compressible flow, pressure can be calculate from density and temperature obtained from the equation of state. For an incompressible flow this is not possible as the density is constant and it is not linked to pressure. This introduces a constraint in the solution: the velocity field has to satisfy continuity if the correct pressure is to be applied to the momentum equations [9].

SIMPLE stand for Semi-Implicit Method for Pressure Linked Equation and it is an algorithm able to resolve the pressure-velocity linkage using an iterative method. This algorithm was presented by Pantakar and Spalding [9] and it calculates the pressure on a guess and correct basis. This method was developed around the staggered grid concept for velocity components introduced by Harlow and Welch [9]. With this method the scalar variable are evaluated at the nodal point while the velocity components are calculated on a staggered grid which is centred to the cell face.

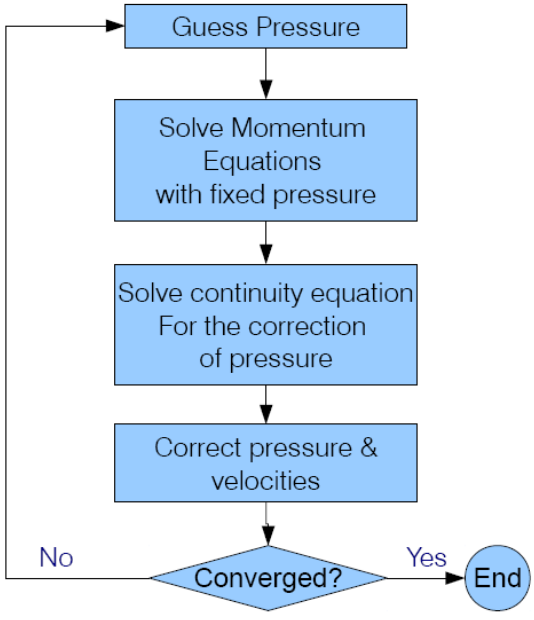

Figure 2-1: SIMPLE Algorithm [18]

2.2 Numerical methods in FLUENT 12

2.2.1 RANS

All the formulas in this section were extracted from the ANSYS FLUENT 12 Theory Manual [19].

2.2.1.1 K-ε Model

This is the most common turbulence model approach used in the engineering field due to its robustness and accuracy applicable to a wide range of flow at low computational cost. In this model two transport equations are used to obtain kinetic energy K and dissipation rate ε. ANSYS Fluent offers three turbulence models based on this approach. The Standard K-ε was the first to be introduced and its formulation was based on original work presented by Launder and Spalding, following this the RNG K-ε and Realizable K-ε were then introduced. The last two versions aimed at improving the performance of the Standard K-ε.

In the RNG model a mathematical technique denominated RNG (renormalization group) is applied to the instantaneous Navier-Stokes equations. Additional terms in the transport equations improve accuracy; analytical formulas are used for Prandtl numbers and for low Reynolds number flow.

The Realizable model is the newest to be introduced. In this model mathematical constrains are applied to the Reynolds stresses in order to have more consistency with the flow physics. New formulations for turbulent viscosity and dissipation rate are applied to this model. These changes should result in improved accuracy when dealing with flow separation and recirculation, which are very common in automotive aerodynamics.

Standard K-ε transport equations

$$\frac{\partial}{\partial t}(\rho k) + \frac{\partial}{\partial x_i}(\rho k u_i) = \frac{\partial}{\partial x_i}\left[\left(\mu + \frac{\mu_t}{\sigma_t}\right)\frac{\partial k}{\partial x_j}\right] + G_k + G_b - \rho\varepsilon - Y_M + S_k \qquad (2.1)$$

$$\frac{\partial}{\partial t}(\rho\epsilon) + \frac{\partial}{\partial x_i}(\rho\epsilon u_i) =$$

$$= \frac{\partial}{\partial x_i}\left[\left(\mu + \frac{\mu_t}{\sigma_\varepsilon}\right)\frac{\partial\,\epsilon}{\partial x_j}\right] + G_{1\epsilon}\frac{\epsilon}{k}(G_k + G_{3\epsilon}G_b) - G_{2\epsilon\rho}\frac{\epsilon^2}{k} + s_\epsilon \quad (2.2)$$

The term G_k represent the production of turbulent kinetic energy and μ_t is the turbulent viscosity calculated with the value of K and ε. The values of various constants C comes from experiments and can be modified by the user. Y_M take into account the effect of compressibility and the S terms are defined by the user.

K-ε RNG transport equations

$$\frac{\partial}{\partial t}(\rho k) + \frac{\partial}{\partial x_i}(\rho k u_i) = \frac{\partial}{\partial x_i}\left[\alpha_k \mu_{eff}\frac{\partial\,k}{\partial x_j}\right] + G_k + G_b - \rho\varepsilon - Y_M + S_k \quad (2.3)$$

$$\frac{\partial}{\partial t}(\rho\varepsilon) + \frac{\partial}{\partial x_i}(\rho\varepsilon u_i) =$$

$$= \frac{\partial}{\partial x_i}\left[\alpha_\epsilon \mu_{eff}\frac{\partial\,\varepsilon}{\partial x_j}\right] + G_{1\epsilon}\frac{\varepsilon}{k}(G_k + G_{3\epsilon}G_b) - G_{2\epsilon\rho}\frac{\varepsilon^2}{k} - R_\in + S_\epsilon \quad (2.4)$$

The two terms α_k and α_ϵ are the inverse effective Prandtl numbers. The constants have the same denomination as the ones used in the standard K-ε model but they have different values.

Realizable K-ε transport equations

$$\frac{\partial}{\partial t}(\rho k) + \frac{\partial}{\partial x_i}(\rho k u_i) = \frac{\partial}{\partial x_i}\left[\left(\mu + \frac{\mu_t}{\sigma_t}\right)\frac{\partial\,k}{\partial x_j}\right] + G_k + G_b - \rho\varepsilon - Y_M + S_k \quad (2.5)$$

$$\frac{\partial}{\partial t}(\rho\varepsilon) + \frac{\partial}{\partial x_i}(\rho\varepsilon u_i) =$$

$$= \frac{\partial}{\partial x_i}\left[\left(\mu + \frac{\mu_t}{\sigma_\varepsilon}\right)\frac{\partial\,\varepsilon}{\partial x_j}\right] + \rho C_1 S_\epsilon - \rho C_2\frac{\epsilon^2}{k + \sqrt{\nu\epsilon}} - G_{1\epsilon}\frac{\epsilon}{k}C_{3\epsilon}G_b + S_\epsilon \quad (2.6)$$

This turbulence model use a different formulation for the eddy viscosity and the model constants have a different values form the standard and RNG K-ε models.

2.2.1.2 K-ω SST

This is a two equation turbulence model developed by Menter [19] with the aim to combine the accuracy of the K-ω model in near wall condition with the behaviour of the K-ε in the far field. In practice this is achieve thanks to a blending function which allows the model to work as K-ω close to the wall region and then switch to a modified K-ε model far from the wall region. SST stands for Shear Stress Transport which means that the transport of turbulent shear stress is taken into account when defining the turbulent viscosity.

The two transport equation used to obtain kinetic energy and specific dissipation rate are:

$$\frac{\partial}{\partial t}(\rho k) + \frac{\partial}{\partial x_i}(\rho k u_i) = \frac{\partial}{\partial x_i}\left(\Gamma_k \frac{\partial k}{\partial x_j}\right) + \widetilde{G_k} - Y_k + S_k \tag{2.7}$$

$$\frac{\partial}{\partial t}(\rho \omega) + \frac{\partial}{\partial x_i}(\rho \omega u_i) = \frac{\partial}{\partial x_i}\left(\Gamma_\omega \frac{\partial \omega}{\partial x_j}\right) + \widetilde{G_\omega} - Y_\omega + D_w + S_\omega \tag{2.8}$$

Where D_w represent the cross diffusion term; Γ_k , Γ_ω represent the effective diffusivity of K and ω respectively.

2.2.2 LES

Instead of time averaging the Navier Stokes equation, LES is obtained by filtering the unsteady Navier Stokes equations. The filtering process acts as a selection criteria between the largest eddies that need to be solve directly and the smallest eddies which are then modelled with a sub grid-scale model. In ANSYS FLUENT the filtering operation is obtained by the finite-volume discretization [19]. This means that eddies larger than the grid size are solved directly while eddies smaller then grid size are modelled.

From the filtering process the following equations are obtained:

$$\frac{\partial \rho}{\partial t} + \frac{\partial}{\partial x_i}(\rho \bar{u}_i) = 0 \tag{2.9}$$

$$\frac{\partial}{\partial t}(\rho \bar{u}_i) + \frac{\partial}{\partial x_i}(\rho \bar{u}_i \bar{u}_j) = \frac{\partial}{\partial x_j}(\sigma_{ij}) - \frac{\partial \bar{p}}{\partial x_i} - \frac{\partial \tau_{ij}}{\partial x_j} \tag{2.10}$$

The term τ_{ij} is defined by the following equation:

$$\tau_{ij} = \rho\overline{u_i u_j} - \rho \bar{u}_i \bar{u}_j \tag{2.11}$$

τ_{ij} is the sub grid-scale stress and needs to be modeled. In the Smagorinsky-Lilly model the eddy viscosity is modelled using the following equation:

$$\mu_t = \rho L_s^2 |\bar{S}| \tag{2.12}$$

Where L_s is computed using the following formula:

$$L_s = \min(kd, C_s \Delta) \tag{2.13}$$

K is the Von Kàrmàn constant, d is the distance to the closest wall, C_s is the Smagorinsky constant which in ANSYS FLUENT is equal to 0.1, Δ depends on the cell size used $(\Delta = V^{1/3})$.

2.2.3 Wall function

Turbulent flows are heavily affected by wall boundaries. The near wall regions can be subdivided in three layers. The layer closer to the wall boundary is called viscous sublayer, in this region the flow is mostly laminar and viscosity is the dominant factor in determining momentum and mass transfer. This is then followed by a buffer layer region where the effect of turbulence has to be taken into account. After that, the outer region can be considered fully turbulent. Turbulence models such as Spalart-Allmaras and Standard K-ω are able to resolve the viscous sub layer if a near wall modelling approach is adopted. A very fine mesh near the wall is needed and due to this (especially considering high Reynolds number) this approach can be computationally prohibitive. Other

turbulent models such as K-ε are only valid for fully turbulent flow so the sub-layer and buffer layer regions cannot be resolved. These two regions are in fact taken into account by using empirical formulas called "wall functions". Thanks to this, a more coarse mesh can be used near the wall and less computational resources are needed for the simulation.

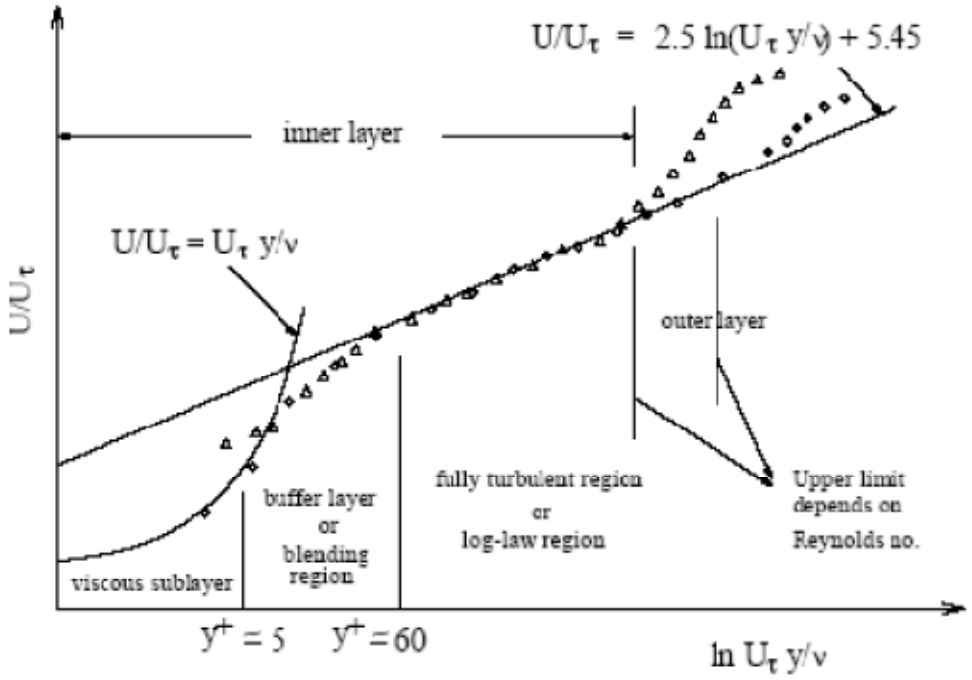

Figure 2-2: Layers in the near wall region [19]

ANSYS FLUENT offers different wall treatment depending on turbulent models and mesh resolution adopted. Due to the high Reynolds number and computational resources available two wall approaches were used for this thesis: Standard wall function and Werner Wengle wall function.

2.2.3.1 Standard Wall Function

This is the simplest standard wall function available, based on the formulation given by Launder and Spalding is still used for industrial flow. The law of the wall is applied to the velocity in the logarithmic region:

$$U^* = \frac{1}{k}\ln(Ey^*) \tag{2.14}$$

$$U^* = \frac{U_p C_\mu^{1/2} k_p^{1/2}}{\tau_\omega/\rho} \tag{2.15}$$

$$y^* = \frac{\rho C_\mu^{1/4} K_P^{1/2} y_P}{\mu} \tag{2.16}$$

ANSYS FLUENT applies the logarithmic law when $y^* > 11.25$. Below this value, the laminar stress-strain relationship is applied so that $U^* = y^*$.

2.2.3.2 LES wall treatment

ANSYS FLUENT allows the use of near wall treatment for LES simulation. This is based on the formulation given by Werner and Wengle :

$$|\tau_\omega| = \begin{cases} \dfrac{2\mu|u_p|}{\Delta z} \\ \rho\left[\dfrac{1-B}{2} A^{\frac{1+B}{1-B}} \left(\dfrac{\mu}{\rho\Delta z}\right)^{1+B} + \dfrac{1+B}{A}\left(\dfrac{\mu}{\rho\Delta z}\right)^{B} |u_p|\right]^{\frac{2}{1+B}} \end{cases} \tag{2.17}$$

Where u_p is the wall parallel velocity, Δz is the near wall control volume length scale, A = 8.3 and B = 1/7

2.2.4 Spatial discretization

ANSYS FLUENT uses the Finite Volume Method in order to disrcetize the turbulence equations introduced in the previous chapter. This means that the flow volume, over which the flow behaviour is calculated, is subdivided into smaller volume called cells. The solver store the scalar value ϕ at the cell centre while the face values $\emptyset_f$ is interpolated from the cell centre value through a procedure denominated Upwind differencing scheme. This means that the flow direction is taken into account during the calculation of the face values.

2.2.4.1 Third Order MUSCL Scheme

This is the spatial discretization scheme used for the RANS calculations. This scheme is obtained from a blend of the second order upwind scheme and the central differencing scheme:

$$\emptyset_f = \theta_{\emptyset f,CD} + (1-\theta)_{\emptyset f,SOU} \tag{2.18}$$

This scheme has to potential to reduce numerical diffusion hence improving spatial accuracy. For this reason it should be more suitable than second order schemes when dealing with complex three dimensional flow structures.

2.2.4.2 Bounded central differencing scheme

In ANSYS FLUENT this is the default scheme when LES is selected due to its low numerical diffusion. This scheme is based on the normalized variable diagram (NVD) approach [19] and the convection boundedness criterion (CBC).

2.2.5 Time discretization

Transient simulations have to be discretize for both space and time. The second order discretization is obtained as follow:

$$\frac{3\,\phi^{n+1} - 4\phi^{n} + \phi^{n-1}}{\Delta t} = F(\phi) \tag{2.19}$$

Where ϕ is a scalar quantity and n store the value at the current time level. $F(\phi)$ can be evaluated using an implicity or explicit time integration. The explicit time integration is only available for the density based solver. The LES simulation in this study used a pressure based solver with implicit time integration. With the implicit method the equation is solved iteratively at each time step before moving to the next one. This scheme is unconditionally stable so that the time step is not limited by the Courant-Friedrich-Lewy condition.

2.3 Grid generation

This CFD study aims to validate different turbulence models compared with the wind tunnel experiment obtained by Lienhart and Becker [12] and by P.Drage et al [4] using the Ahmed body with the 25° slant angle configuration. Both wind tunnel experiments were conducted in a 3/4 open test section with inlet speeds at 40 m/s giving a Reynolds number of around 2.8 million (based on the Ahmed body length). It should be noted that in the original Ahmed's experiment [10] the model was tested using an inlet speed of 60 m/s.

The Ahmed body was generated with the commercial CAD package CATIA V5 using the geometrical specification obtained from the original Ahmed SAE publication [10]. The Ahmed body has a length of 1.044 m, a width of 0.389 m and a height of 0.288 m. The supporting struts used in the experimental test were also modelled. These are composed of four cylinders which elevate the Ahmed body over the ground by 50 mm.

The computational flow domain has a total length of 8.352 m which is equivalent to 8 body lengths. The inflow boundary is located upstream of the model (2 body lengths) while the outflow boundary is located downstream of the model (5 body lengths). The width and height of the domain are equivalent to 2 model lengths giving a blockage ratio of 2.8 %. Overall, the flow domain has the dimension of 8L x 2L x 2L (length x width x height) where L represents the Ahmed body length.

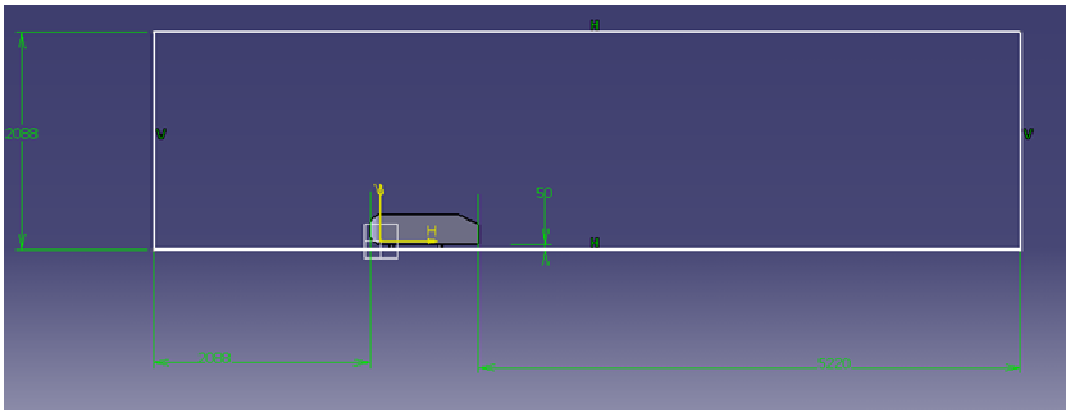

Figure 2-3 CAD geometry of the Ahmed body and flow domain

The mesh strategy adopted can be classified as a viscous hybrid mesh. The first phase consists of creating the surface mesh on the Ahmed body and on the flow domain, using the commercial software ANSA 13. This software is one of the most used meshing tools used in the Automotive and Motorsport environment. The big advantage when compared to traditional meshing packages used in academia such as Gambit and Gridgen is that ANSA allows for a large number of functions that help the user to repair CAD geometries so that complex automotive geometries can be meshed under tight time constraints. The surface mesh is composed of triangular elements. The edge length used on the Ahmed body is 5 mm while for the flow domain an edge length of 100 mm was adopted.

The surface mesh was then imported in TGRID for the volume mesh generation. The volume mesh is composed of prismatic elements around the wall boundaries (Ahmed body and ground). The prismatic elements are generated by extruding the surface mesh. A total of 7 prismatic layers were obtained. The layers are aligned with the incoming flow and are more likely than pyramids elements to capture boundary layer effects. The first layer height is equal to 0.5 mm which in the RANS simulation gave an average Y+ value of approximately 30 on the Ahmed body.

The remaining volume was then filled with hexcore elements. The transition between prisms elements and hexcore was managed automatically by TGRID

by creating pyramids elements on the top of the prismatic layers. The complete automation of the volume mesh has the disadvantage of creating small mesh elements where not needed such as at the top and side surfaces of the domain away from the body. A way to control this would be to increase further the growth ratio of the surface meshes far from the Ahmed body but this will stretch some of the pyramids elements hence the level of skewness will be likely to increase. In order to have a smoother transition between prisms and hexcore elements 1 buffer layer was used. Buffer layers are commonly used in TGRID to control the expansion of the hexcore. Increasing the number of buffer layers guarantee a smooth transition but this inevitably increases the mesh size. A refinement box was created in order to have an increased mesh definition around the Ahmed body and immediately behind it. The box had the overall dimension of 3000 x 1000 x 1000 (X,Y,Z). Three different grids of around 5 (Figure 2-5), 7.7 (Figure 2-6), 12 (Figure 2-7) million elements were generated by decreasing the hexcore maximum cell size and by further hexcore refinement in the refinement box.

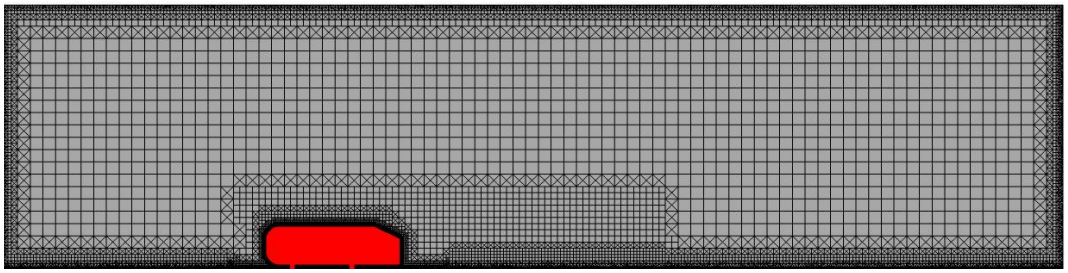

Figure 2-4 Coarse volume mesh

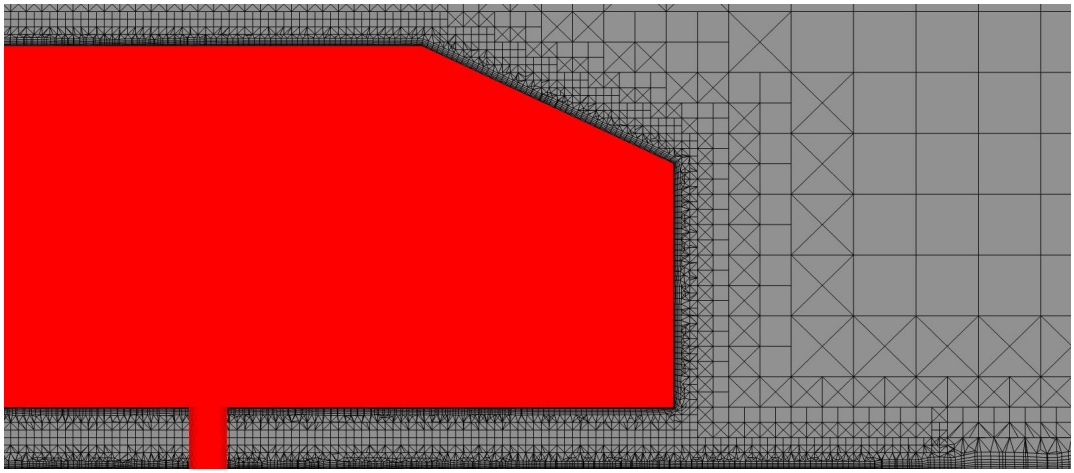

Figure 2-5 Coarse volume mesh detail

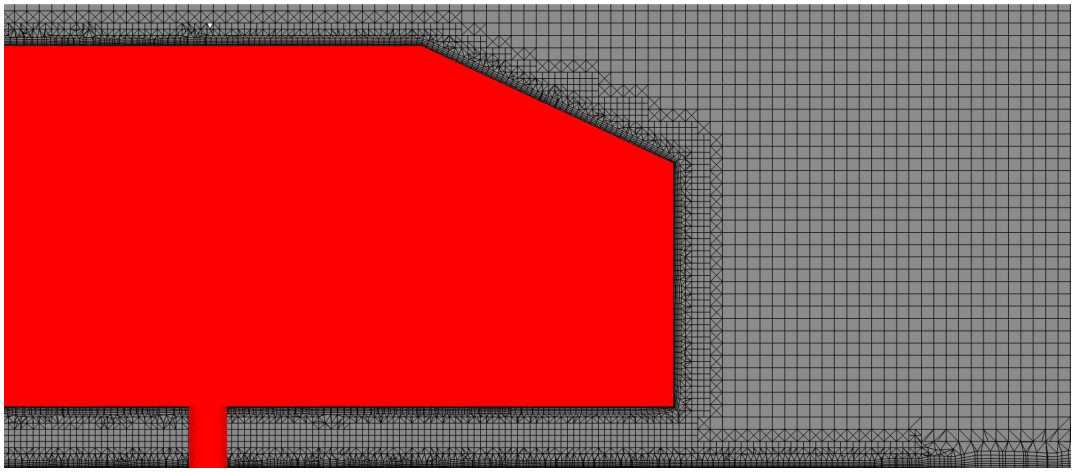

Figure 2-6 Medium volume mesh detail

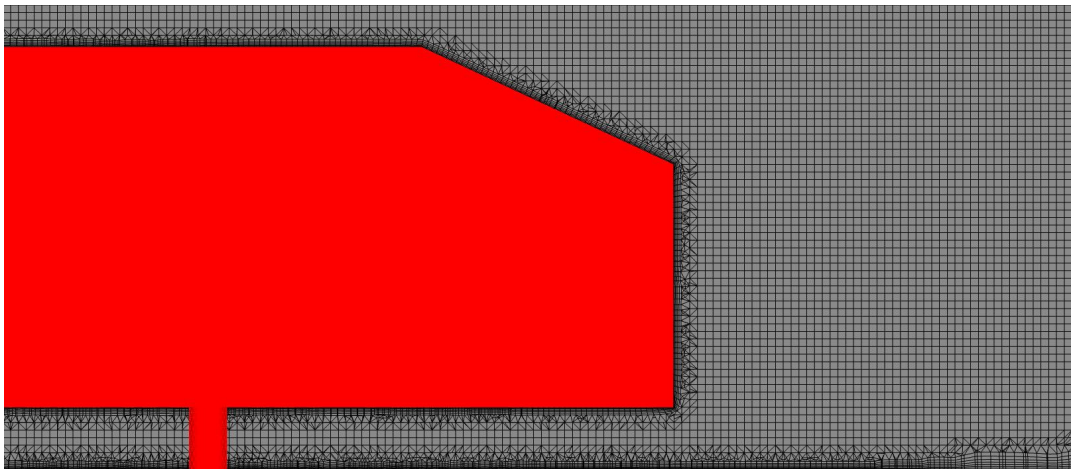

Figure 2-7 Fine volume mesh detail

	AB-03	AB-07	AB-04
Global surface mesh count	703142	703142	703142
Surface mesh elements to be prism	346832	346832	346832
Mesh size on Ahmed body	5 mm	5 mm	5 mm
Mesh size under Ahmed body	5 mm	5 mm	5 mm
Edge length on flow domain	20 mm	20 mm	20 mm
Number of prism layers	7	7	7
First aspect ratio	10	10	10
First layer height	0.5 mm	0.5 mm	0.5 mm
Geometric growth rate	1.2	1.2	1.2
Last aspect ratio	3.34898	3.34898	3.34898
Max hexcore cell length	100 mm	80 mm	100 mm
Buffer layers	1	1	1
Refinement box x	3000 mm	3000 mm	3000 mm
Refinement box y	1000 mm	1000 mm	1000 mm
Refinement box z	1000 mm	1000 mm	1000 mm
Hexcore cell size (refinement volume)	50 mm	12.5 mm	6.25 mm
Total cell count	5145785	7068452	11558543
Skew	0.799538	0.799986	0.840319
Squish	0.724626	0.766619	0.748992

Table 2-1: Volume mesh parameters for the coarse (AB-03), medium (AB-07) and fine grid resolution (AB-04).

3 Results

3.1 RANS simulations grid convergence study

Standard k−ε, RNG k−ε, Realizable k−ε and K-ϖ SST were tested on the three different grid resolutions in order to observe the variation of drag and lift coefficients with different grid refinements. The Drag and lift coefficients together with residuals were monitored and plotted during the simulations. All the simulations were run for 2000 iterations, the simulations based on the fine grid refinement were run up to 5000 iterations in order to assess the stability of drag and lift coefficients.

Observing the Cd convergence plot (Figure 3.1) for the coarse grid, it is possible to notice that the values for K−ε stabilize after about 800 iterations. The Realizable K−ε and K-ϖ SST reach stable results at around 1200 iterations while the RNG k−ε shows some oscillations up to 2000 iterations. The drag value for this turbulence model shows oscillatory behaviour (between 0.33 and 0.34). Looking at the Cl convergence plot (Figure 3.2), the values tend to settle after about 1000 iterations for most of the turbulence models except for the RNG k−ε model. Also in this case the Cl values show oscillations up to 2000 iterations, the values oscillate between 0.3 and 0.34. The reverse average of the Cl values for the RNG k−ε model and K-ϖ SST were also plotted. The graph shows that the K-ϖ SST stabilize just before reaching the 1000 iterations. The Cl values of the RNG k−ε model keep on decreasing until reaching 4000 iterations.

The increased mesh resolution from 5.1 million to 7.2 million elements seems to have a beneficial effect on Cd and Cl convergence (Figure 3.3-3.4). In fact all the turbulence models show convergence after approximately 1200 iterations for both Cd and Cl values. The improved grid resolution decreased the oscillatory behaviour of the RNG k−ε model.

With the fine grid which contains around 12 million elements, the Cd (Figure 3.5) converges after about 1400 iterations while the Cl (Figure 3.6) value

maintains an oscillatory behaviour even after 2000 iterations for all the turbulence models. The simulations were run up to 5000 iterations in order to observe the oscillatory behaviour of the lift coefficients. The Realizable K$-\varepsilon$ shows increased oscillatory behaviour when compared to the other turbulence models. After 2500 iterations the Realizable K$-\varepsilon$ shows periodic oscillation between 0.41 and 0.43. After 3000 iterations the Cl values obtained from the standard K$-\varepsilon$ settles between 0.4 and 0.41. Beyond the 4000 iterations the Cl values of the RNG k$-\varepsilon$ and K-ϖ SST shows a contained oscillatory behaviour. The oscillations are contained between 0.37 and 0.382 for the RNG k$-\varepsilon$ and form 0.35 and 0.363 for the K-ϖ SST model.

For all the RANS simulations on the three different grid resolutions, the residual of continuity (Appendix A) struggle to reach the 10E-03 value. For the simulations on the fine grid the residuals of continuity are around 10E-02. Switching to lower values of relaxation factors did not have beneficial effects on residuals. The poor grid convergence can be caused by the type of mesh used. The viscous hybrid mesh has pyramid elements between the prisms elements and hexcore elements. Due to the presence of different mesh elements and due to the automatic creation of pyramids and hexcore elements it is difficult to control the level of skewness. The fine grid where in general the convergence is poorer than the other two grids shows a higher skewed level that the other two grids. The numerical instability can also be due to the fact that the RANS models struggle to cope with the high unsteady flow of the Ahmed body.

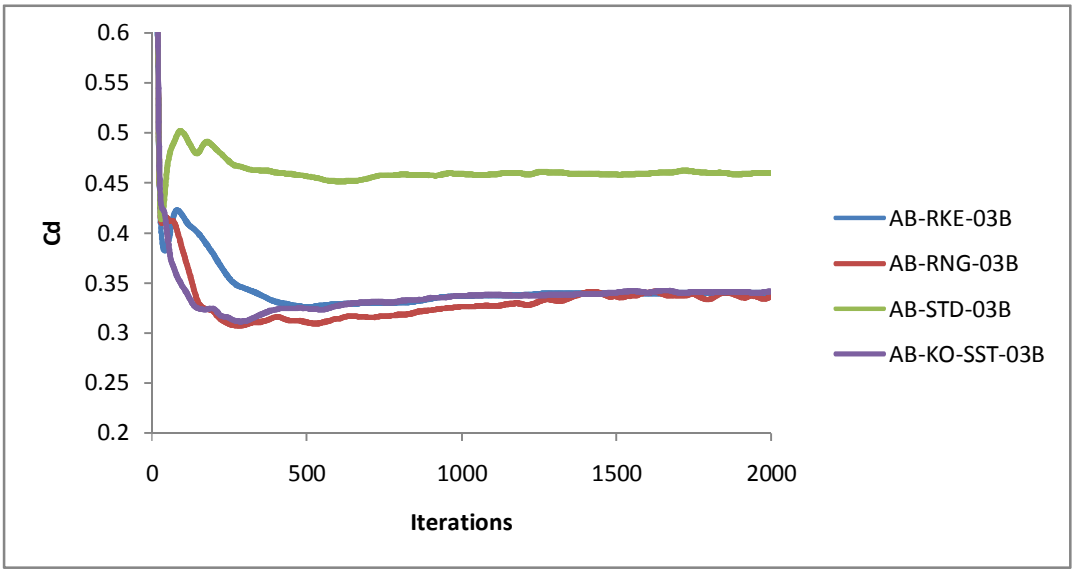

Figure 3-1: Cd values coarse grid.

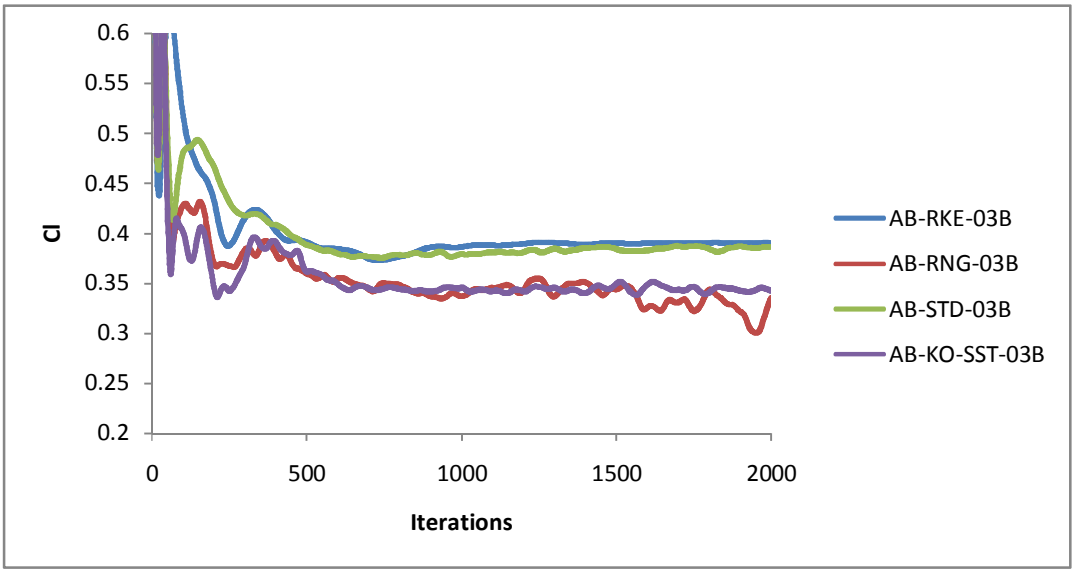

Figure 3-2: Cl values coarse grid.

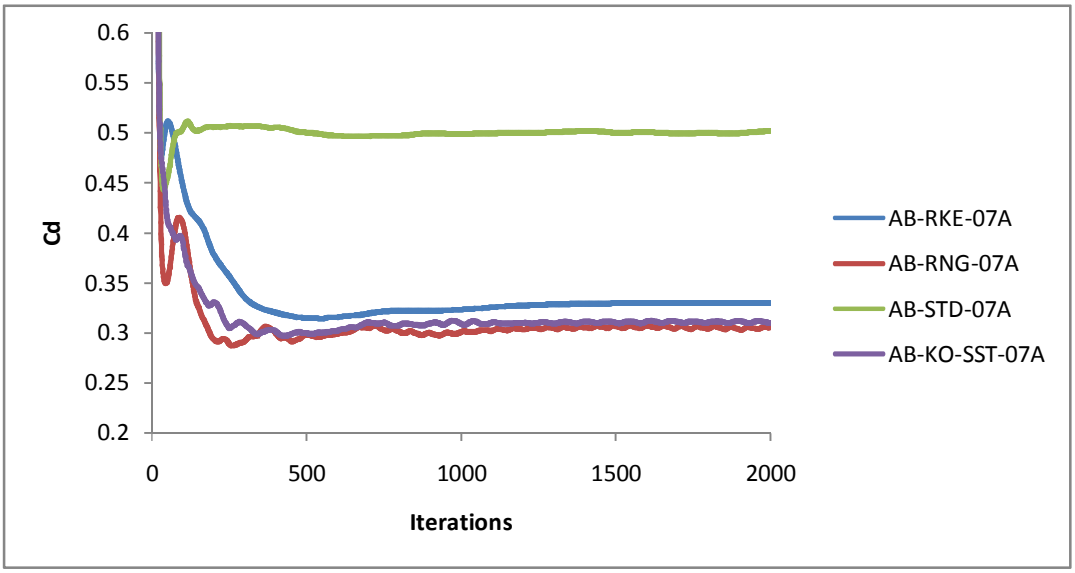

Figure 3-3: Cd values medium grid.

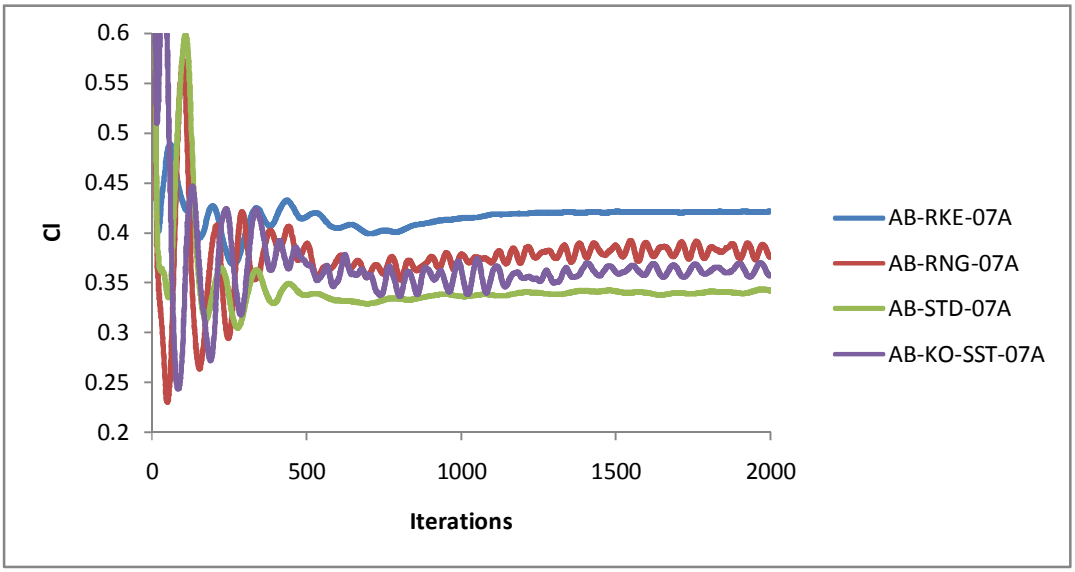

Figure 3-4: Cl values medium grid.

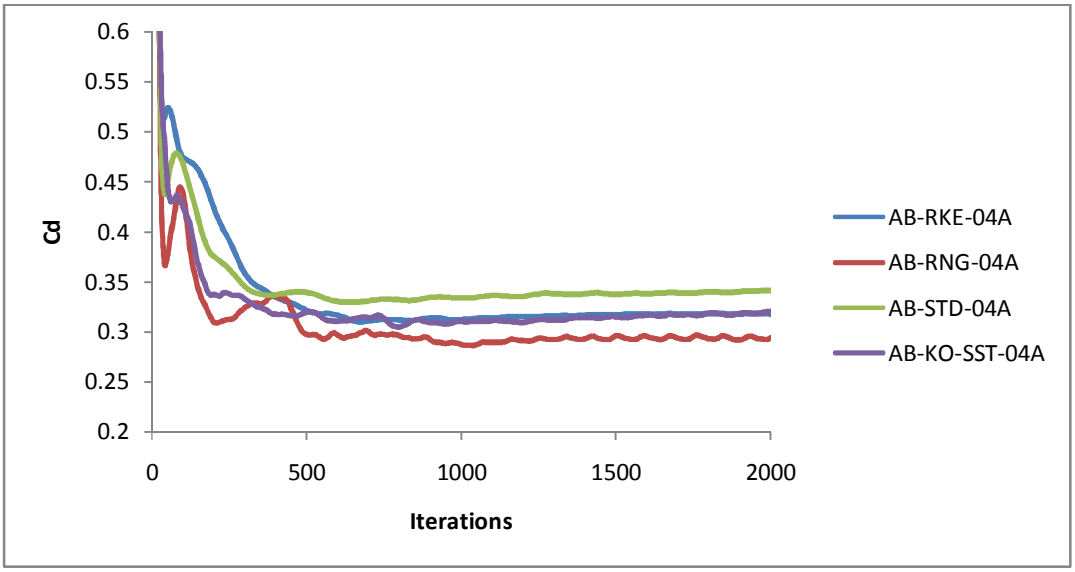

Figure 3-5: Cd values fine grid.

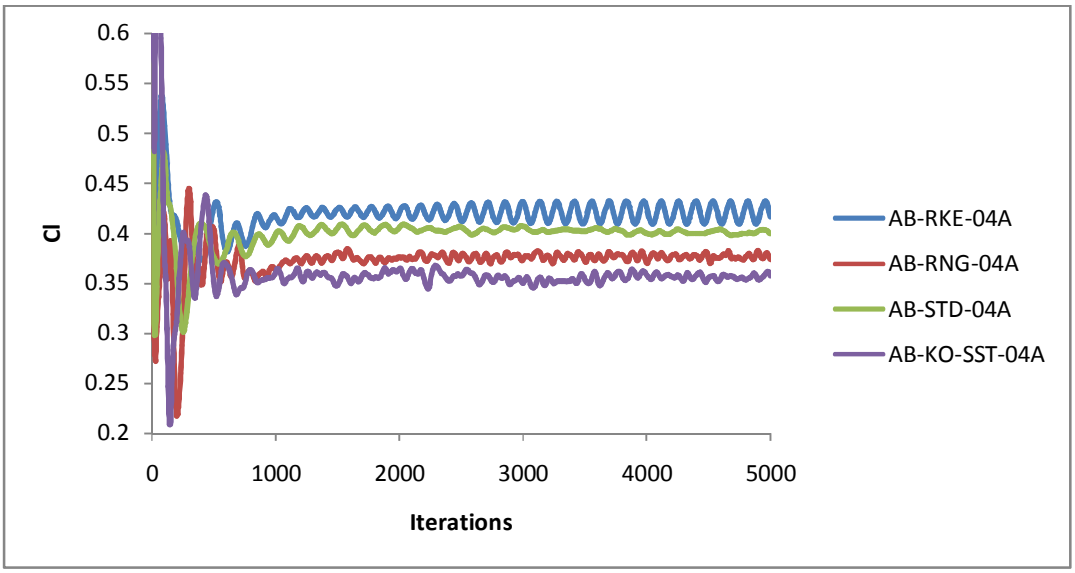

Figure 3-6: Cl values fine grid.

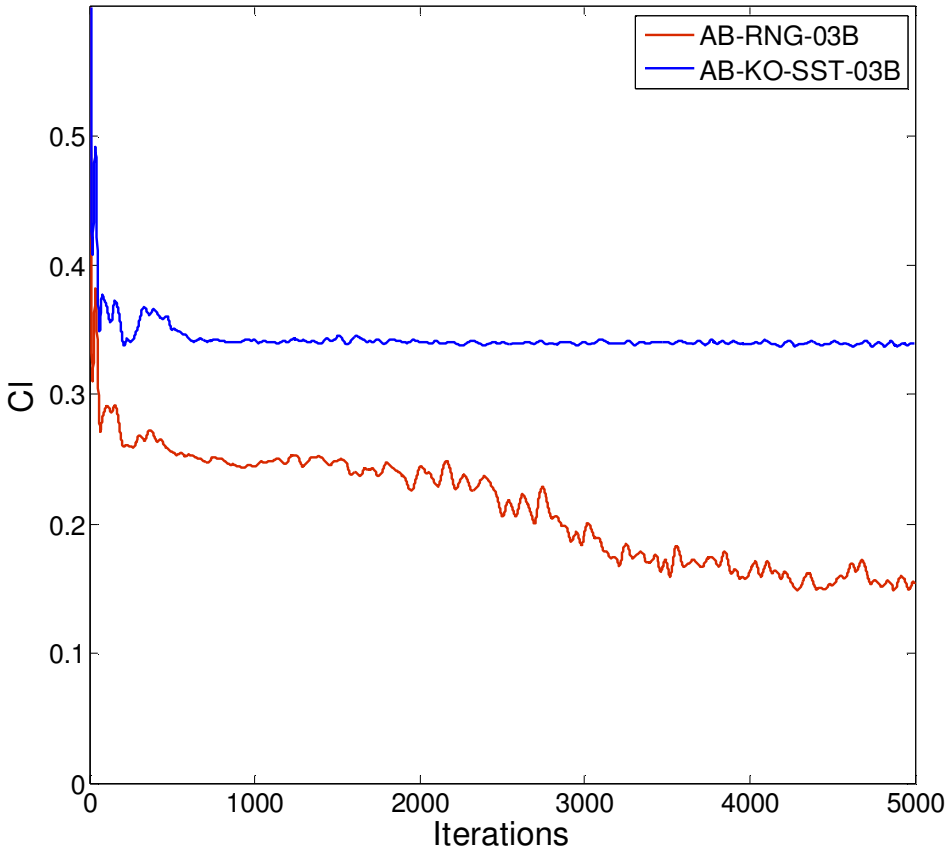

Figure 3-7: Reverse average Cl values coarse grid.

3.2 LES Simulations

The medium and fine grid resolutions were used for the LES simulations. Both meshes can be defined as hybrid meshes. This means that the volume mesh is created by three kinds of mesh element (prisms, pyramids and hexcore) and the cells size varies along the flow domain. By calculating the length scales associated with this flow, it is possible to have an estimate of what the grids should be able to resolve. Based on the work of Tennekes and Lumley [20], Kolmogorov and Taylor micro scales can be calculated using the following formulas:

$$\eta_k = A^{-\frac{1}{4}} Re^{-\frac{3}{4}} l \quad (3.1)$$

$$\eta_\tau = 15^{\frac{1}{2}} A^{-\frac{1}{2}} Re_l^{-\frac{1}{2}} l \quad (3.2)$$

The undetermined constant A was assumed to be equal to 0.5 and l is assumed to be equal to the Ahmed body length (1.044 m). Finally considering that the Reynolds number is equal to 2.78 million, the length scales associated with this flow are $\eta_k = 1.74\,x\,10^{-4}\,L$ and $\eta_\tau = 1.74\,x\,10^{-4}\,L$ where L is the Ahmed body length. Fine and medium grids share the same settings for the prismatic layers. The first layer is located at about $0.5\,x\,10^{-3}\,L$ from the Ahmed body while the top layer has a height of $14\,x\,10^{-3}\,L$. For the medium grid, next to the prism layers the hexcore grows up to $10\,x\,10^{-3}L$ in the wake region and around the Ahmed body. In the fine grid the refinement region limits the maximum hexcore size to $6.25\,x\,10^{-3}\,L$. The mesh spacing used for the prismatic elements is between the Kolmogorov and Taylor length scales. Based on these calculations both grids should be able to resolve the turbulent eddies down to the Taylor scales next to the Ahmed body surface.

Implicit time integration was used for the LES simulations. Consequently the stability of the solution is not limited by the Courant-Friedrich-Lewy condition and CFL greater than 1 are allowed. However, in order to retain accuracy a time step of 0.00001 s was used for the medium grid giving an average CFL of around 1, the simulation was run for 0.67 seconds. In order to decrease the computational time required for the fine grid a time step of 0.0005 s was used which resulted in an average CFL of 35. For the fine grid case the simulation was run up to 1.25 seconds. Both simulations were initialized from previous RANS solutions, the medium grid showed a large oscillation of Cd values during the initial time steps (Figure 3.8). The fine grid showed less marked oscillatory behaviour (Figure 3.9), however for both grids it was possible to notice that the drag values stabilized after 0.1s of simulation. Due to this the values recorded between 0 and 0.1 s were discharged from the data averaging process. In order to better visualize the drag coefficient behaviour a plot was generated by taking

the reverse and forward average of the drag signal [21]. For both simulations the reverse average shows that after about 0.1 seconds of simulation the drag signal tends to stabilize. A forward average is then taken between this point (0.1s) up to the end of the simulation. The forward average plot shows that the Cd signal for the medium grid (obtained from the forward average between 0.1s and 0.67s of simulation) stabilizes at around 0.2 seconds of simulation. For the fine grid the Cd values obtained from the forward average between 0.1 and 1.25s of simulation stabilize after approximately 0.56 seconds of the simulation.

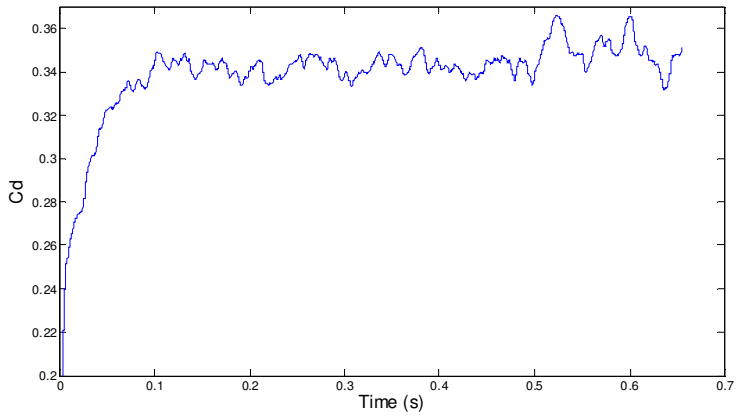

Figure 3-8: LES simulation medium grid Cd signal.

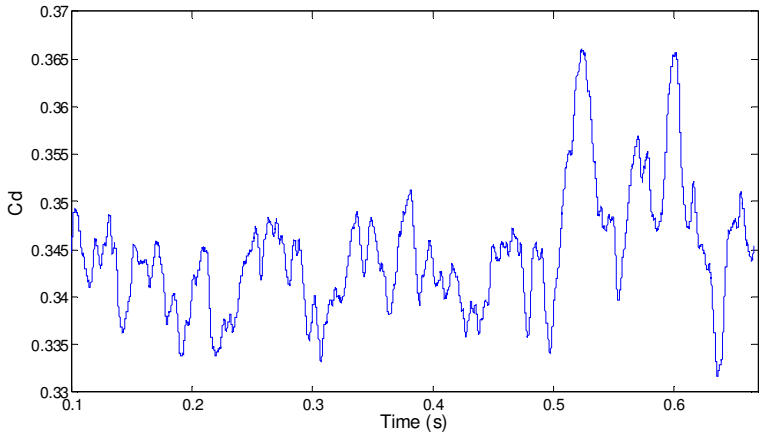

Figure 3-9: LES simulation medium grid Cd signal from 0.1 to 0.67.

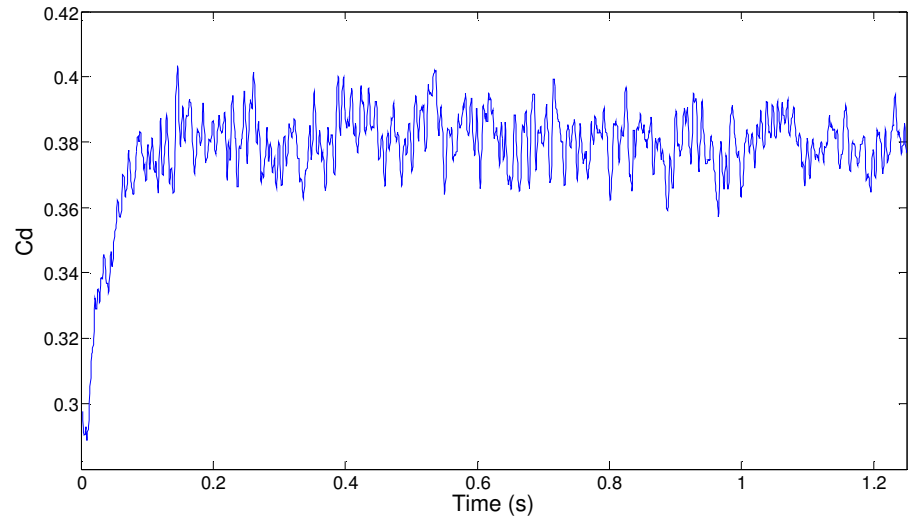

Figure 3-10: LES simulation fine grid Cd signal.

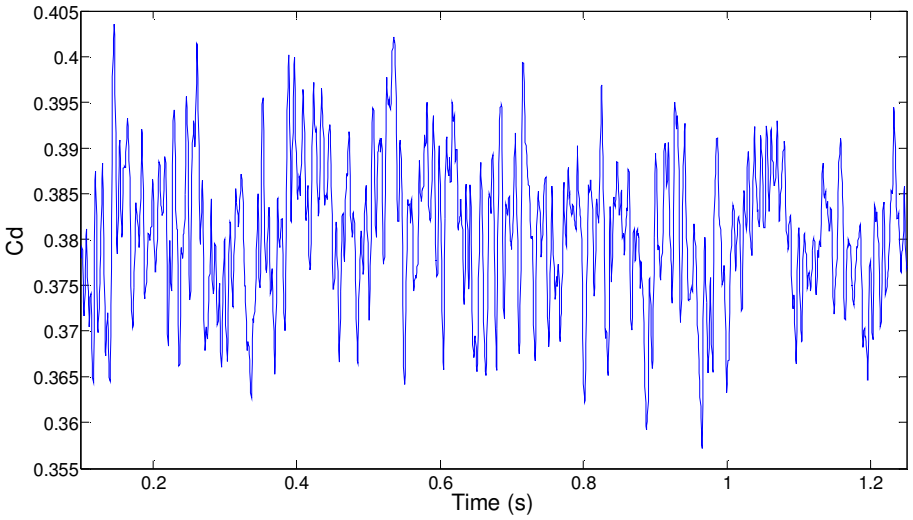

Figure 3-11: LES simulation fine grid Cd signal from 0.1s to 1.25s.

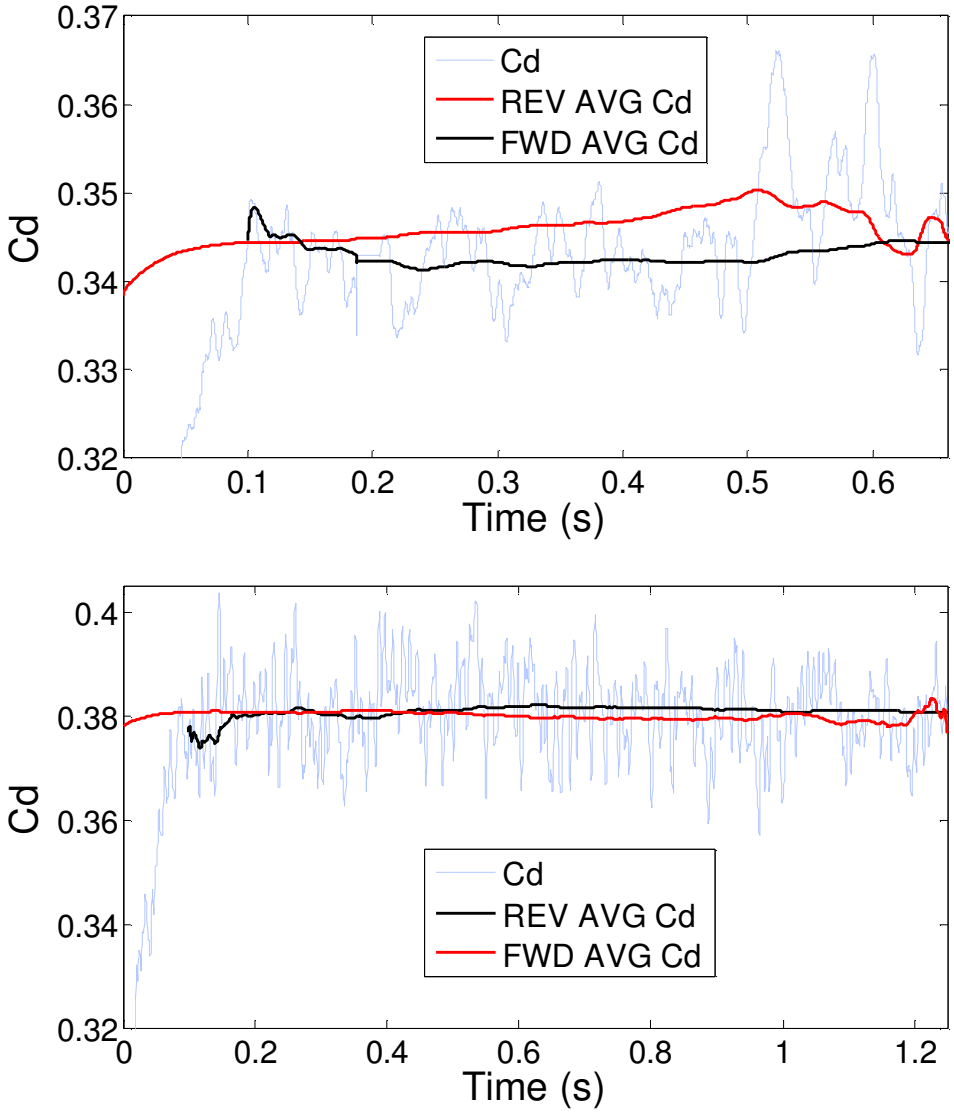

Figure 3-12: Reverse and forward average of the Cd signal for the medium grid (upper) and fine grid (lower)

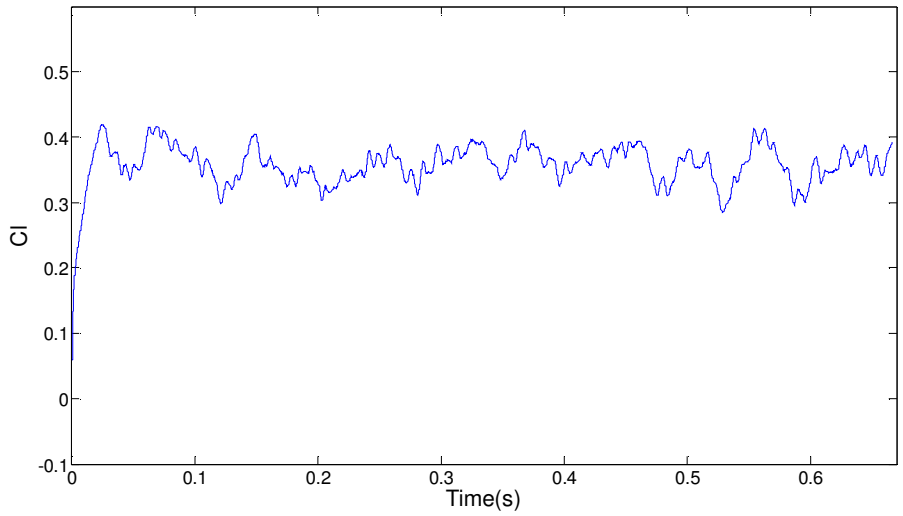

Figure 3-13: LES simulation medium grid Cl signal

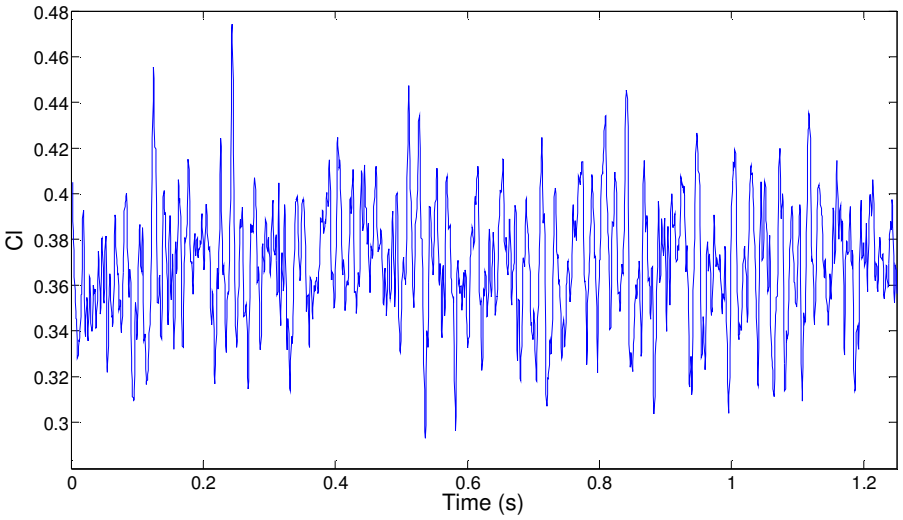

Figure 3-14: LES simulation medium grid Cl signal

3.3 Y plus

The three different mesh resolutions created shared the same Ahmed body surface mesh of 5 mm which was then extruded to create the seven layers of prismatic elements. These elements have the same size for all the meshes. The first layer height was intended to be suitable for wall treatments and hence

satisfy the Y + values recommended by the Fluent manual. Although the first layer height has the constant values of 0.5 mm, the velocity variation along the Ahmed body surfaces resulted in variation of Y+ values. This means that in some location the values recommended by the Fluent manual are not satisfied. The table below reports the average, maximum and minimum Y+ values obtained from the fine grid simulations.

Simulation	Average Y +	Maximum Y+	Minimum Y+
AB-KO-SST-04A	28	58	1
AB-RKE-04A	29	69	2
AB-RNG-04A	28	57	1
AB-STD-04A	30	71	1
AB-LES-04D	25	71	1

Table 3-1: Y + values extracted from the fine grid simulations.

The flow stagnates at the center part of the Ahmed body and then accelerates over the curved front edges. The Y+ values will tend to reach 0 where the velocity tends to reach 0. The Y+ value will tend to reach its maximum value where the velocity increase, which is over the curved front end. At the rear of the body where the flow separates, the Y+ values will then decrease towards zero.

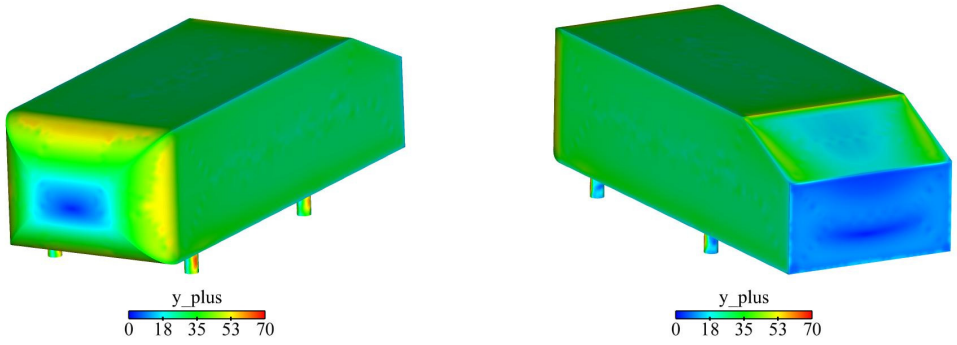

Figure 3-15: Y+ at the front and rear of the Ahmed body. Realizable K−ε fine grid.

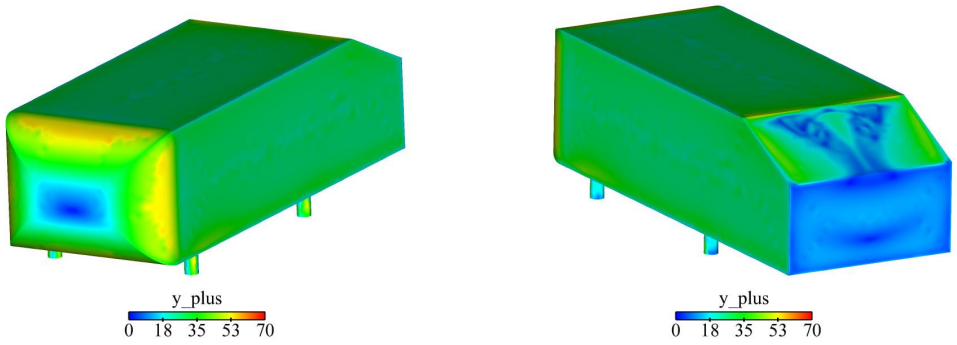

Figure 3-16: Y+ at the front and rear of the Ahmed body. K-ϖ SST fine grid.

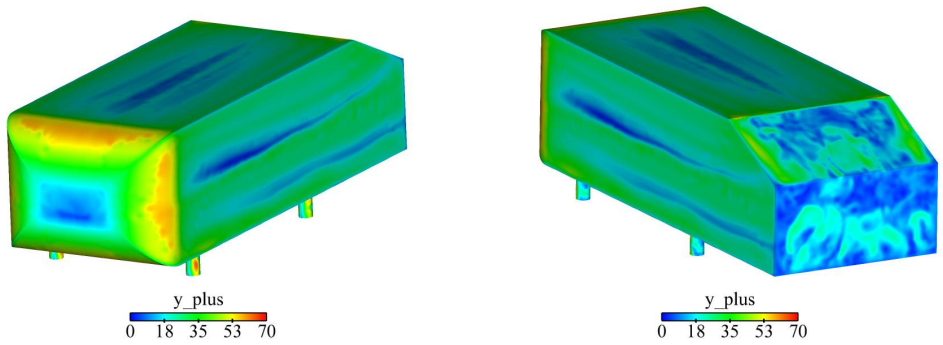

Figure 3-17: Y+ at the front and rear of the Ahmed body. LES fine grid at 1.25 s of simulations (unsteady instantaneous).

3.4 Flow description

In this section the Realizable k$-\varepsilon$, K-ϖ SST and LES simulations on the fine grid are used to describe the flow around the Ahmed body. The LES plots were obtained by averaging 24 data framse from 0.1 to 1.25 seconds.

A few studies available in literature analyze the flow around the Ahmed body front-end. The Ahmed body was designed in order to have a fully attached flow over its front-end. Spohn and Gilleron [11] showed the formation of Kelvin-Helmholts vortices due to flow separation on the top surface of the Ahmed body. None of the simulations conducted in this study showed flow separation over the top-front surface of the Ahmed body. The surface streamlines obtained from the Realizable K-ε , K-ω *SST* and LES on the finest grid show that the flow remains attached over the top surface of the Ahmed body. This is in contrast with the LES study conducted by Krajnovic' and Davidson [16,17] where flow separation and re-attachment over the top and sides front part of the Ahmed body was clearly shown. This difference may be due to the fact that the LES simulation presented in this study used a coarse mesh around the Ahmed body surfaces and the Werner Wengle wall function was applied.

Figure 3-18: Ahmed body surface streamlines. Realizable K$-\varepsilon$ fine grid.

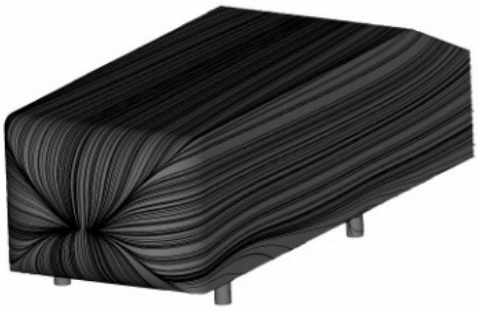

Figure 3-19: Ahmed body surface streamlines. K-ϖ SST fine grid.

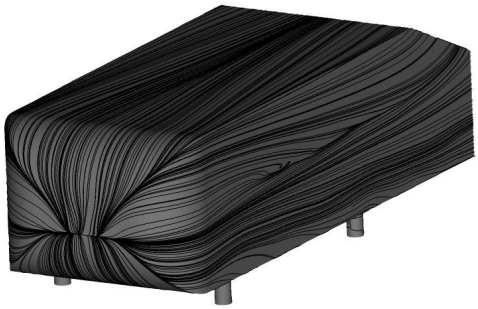

Figure 3-20: Ahmed body surface streamlines. LES fine grid (time averaged).

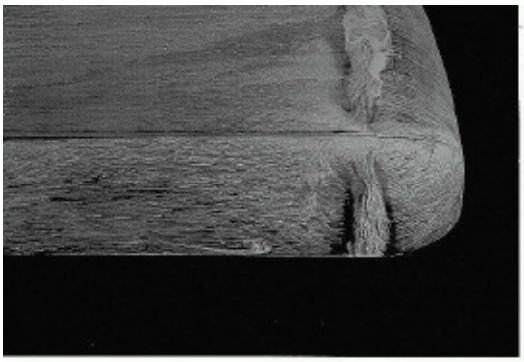

Figure 3-21: Oil film visualization [22].

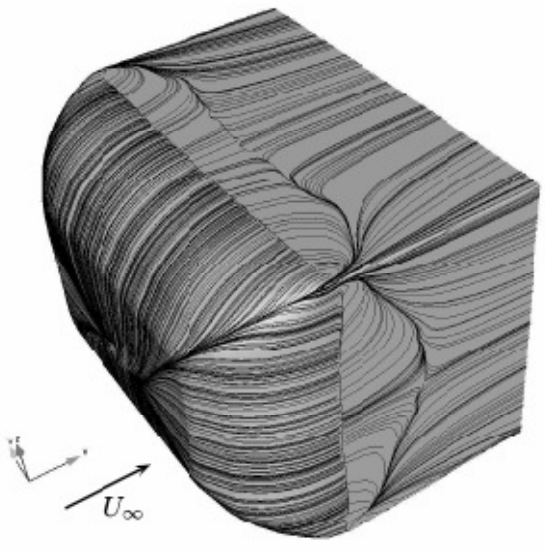

Figure 3-22: Ahmed body surface streamlines [23].

On the side surfaces there is no evidence of separation or re-attachments regions but it is evident that the streamlines are deviated towards the edge created by the side and lower surfaces of the model. The LES also shows also signs of separation on the mid section of the side surfaces. The boundary layer formation on the lower surface of the Ahmed body and the boundary layer formed on the stationary ground generate two longitudinal vortices (one on each side) as shown in the figures 3-25, 3 -26 and 3-27.

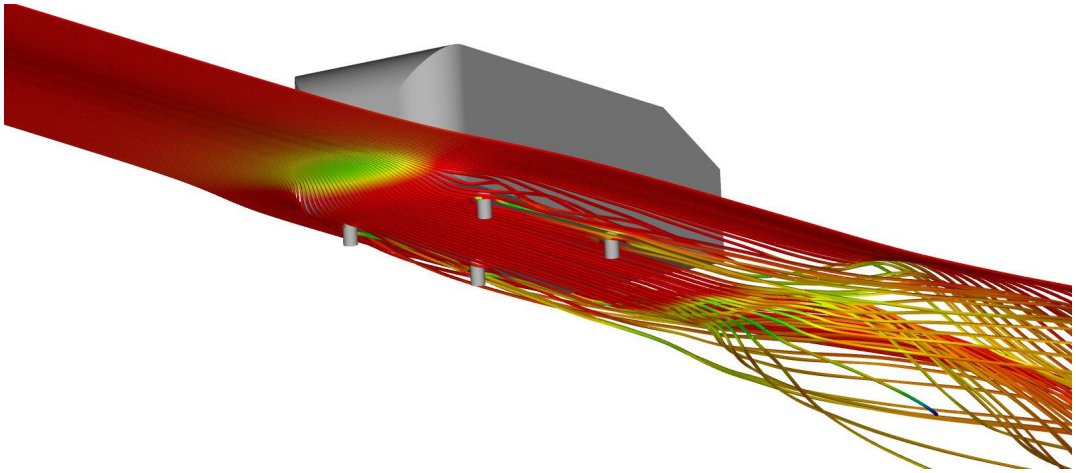

Figure 3-23: 3D streamlines coloured by velocity. Realizable k$-\varepsilon$ fine grid.

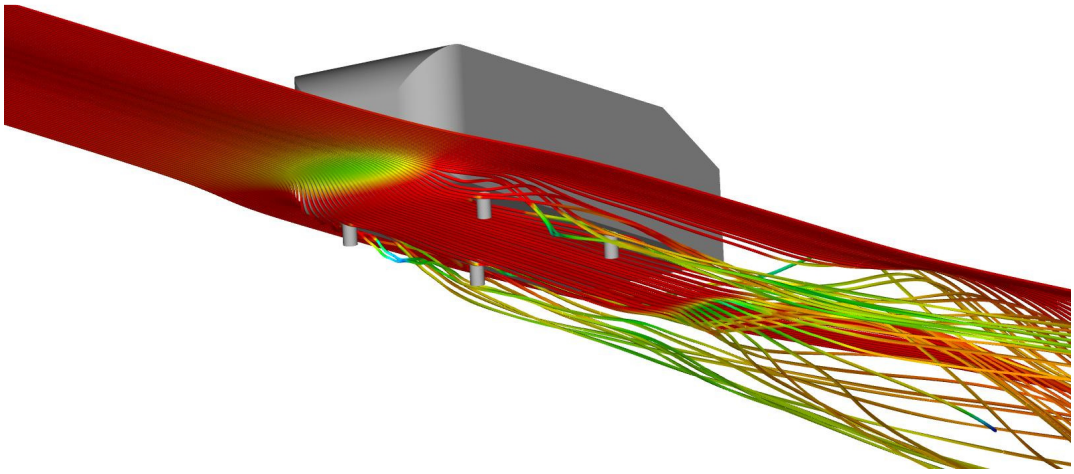

Figure 3-24: 3D streamlines coloured by velocity. K-ϖ SST fine grid.

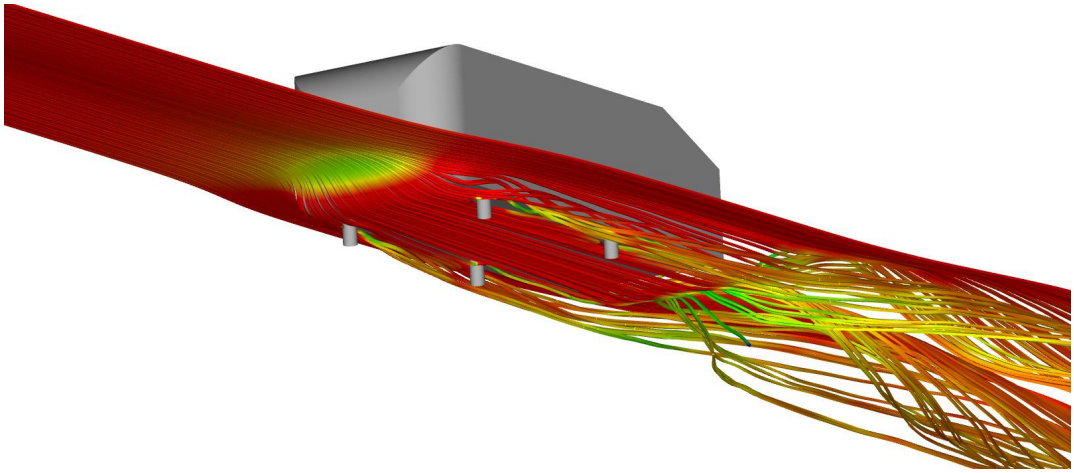

Figure 3-25: 3D streamlines coloured by velocity. LES fine grid (time averaged)

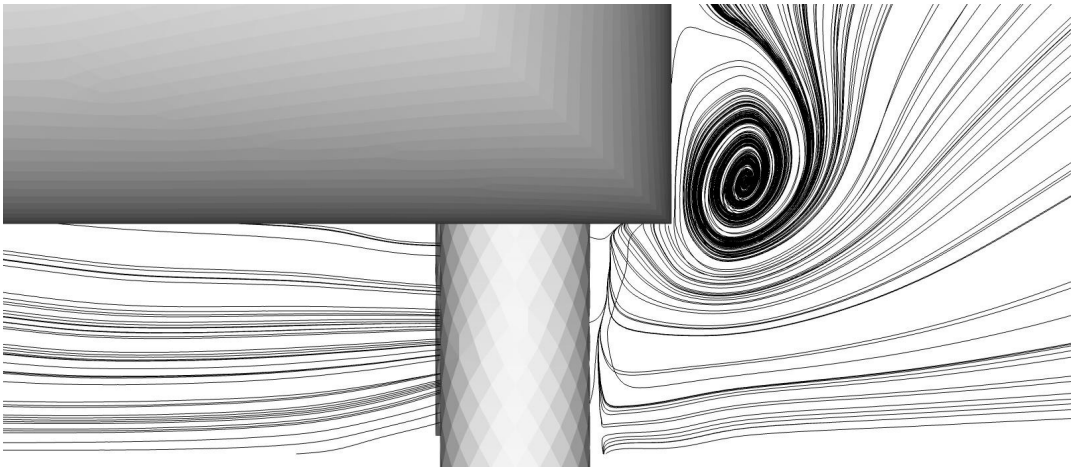

Figure 3-26: Streamlines on plane located at X=0.8. Realizable k$-\varepsilon$ fine grid.

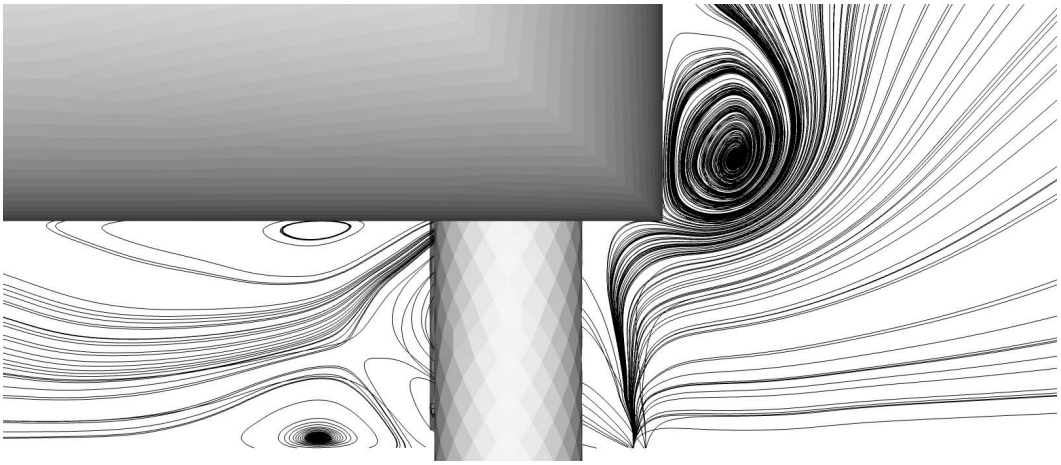

Figure 3-27: Streamlines on plane located at X=0.8. K-ϖ SST fine grid.

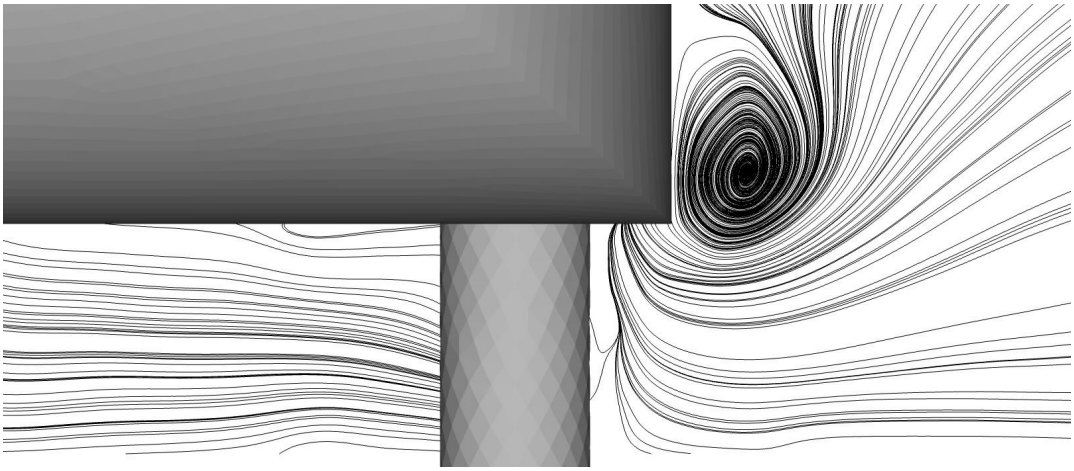

Figure 3-28: Streamlines on plane located at X=0.8. LES fine grid (time averaged).

Although both RANS and LES models predict these longitudinal vortices, the intensity and location are slightly different. Looking at the vortex on the left side of the Ahmed model it is possible to notice that the K-ω SST shows a stronger vortex with a slightly higher core location than the one predicted by the other RANS model. In addition, the K-ω SST predicts the presence of two flow recirculation regions, one on the lower surface of the Ahmed body and one on ground surface. The surface streamlines obtained from the LES simulations shows the presence of the longitudinal vortex but there is no evidence of the two regions of flow recirculation under the Ahmed body as predicted by the K-ω SST model.

Ahmed described that on the slant angle edges the shear layer rolls up and generates two counter rotating vortices. The experiment showed that the strength of these vortices are dependent on the slant angle used and are responsible for keeping the flow attached over a portion of the slant angle. Both the RANS and LES models predict the presence of the two counter rotating vortices. The velocity magnitude plots and projected streamlines over the symmetry plane (y=0) provide evidence for the differences of wake prediction obtained by the turbulence models tested.

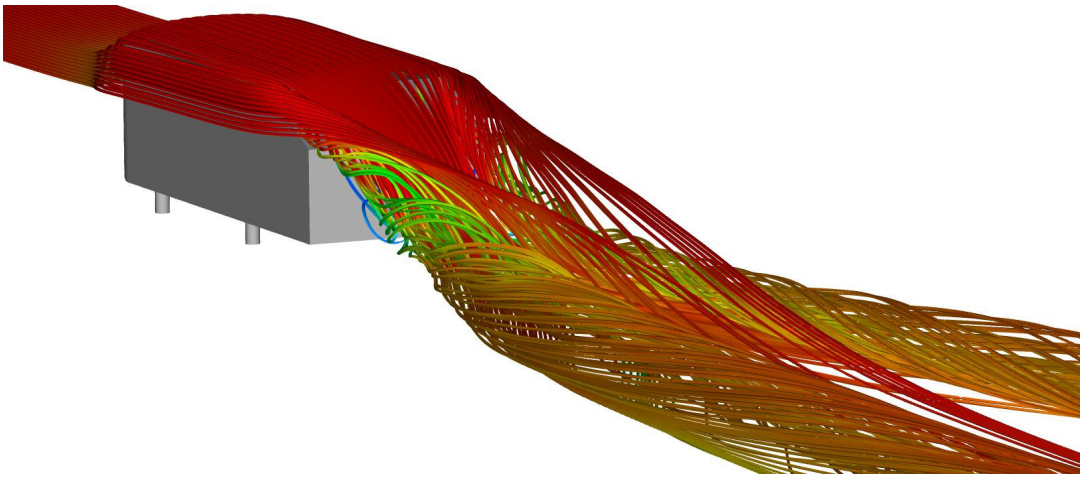

Figure 3-29: 3D streamlines coloured by velocity. Realizable k$-\varepsilon$ fine grid.

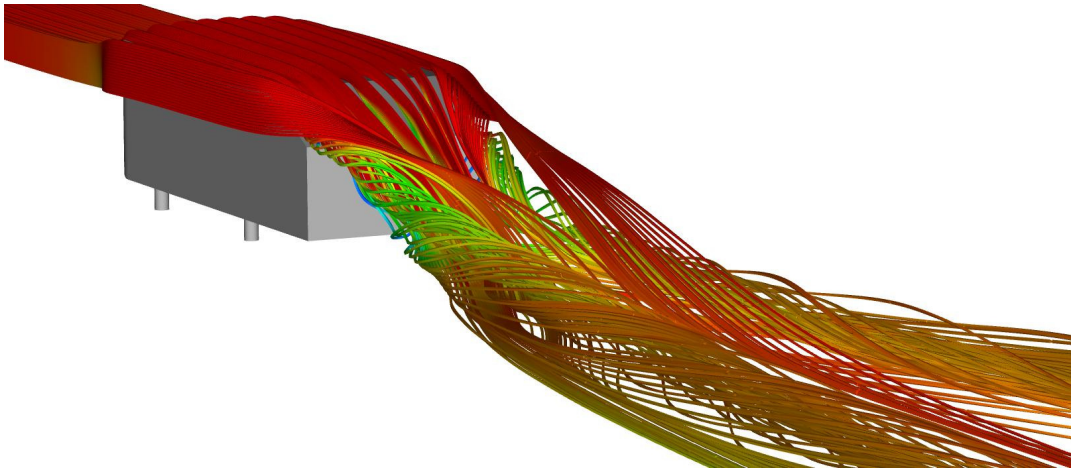

Figure 3-30: 3D streamlines coloured by velocity. K-ϖ SST fine grid.

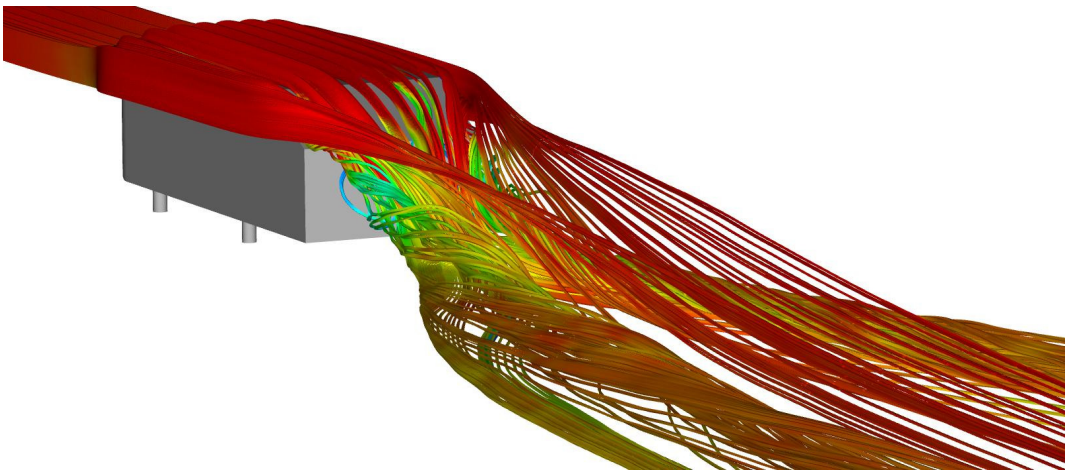

Figure 3-31: 3D streamlines coloured by velocity. LES fine grid (time averaged).

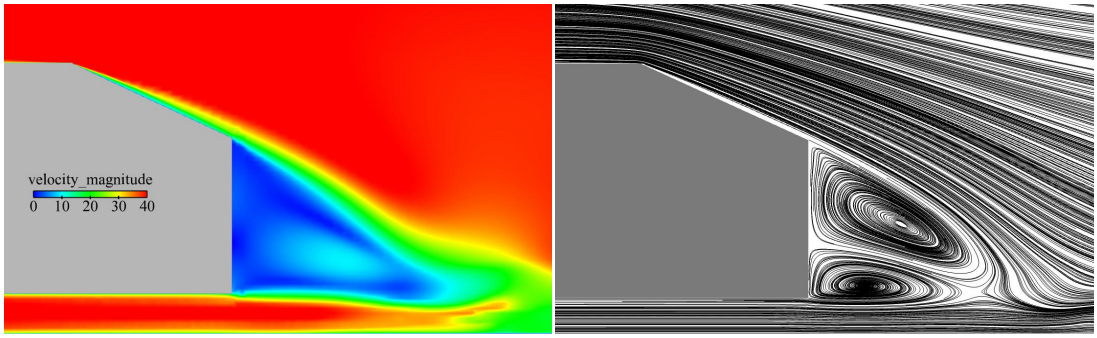

Figure 3-32: Velocity magnitude and streamlines on symmetry plane (y=0). Realizable k$-\varepsilon$ fine grid.

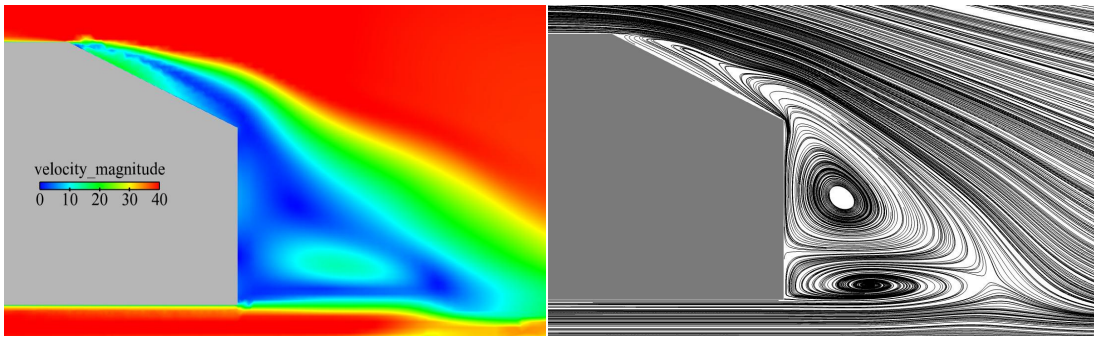

Figure 3-33: Velocity magnitude and streamlines on symmetry plane (y=0). K-ϖ SST fine grid.

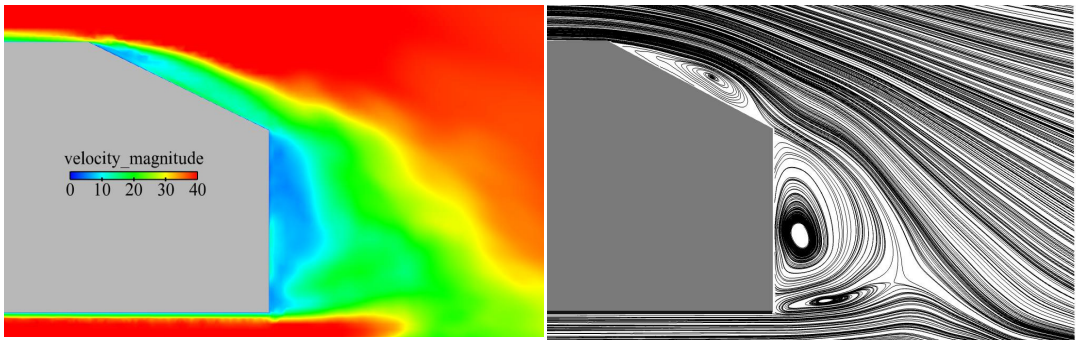

Figure 3-34: Velocity magnitude and streamlines on symmetry plane (y=0). LES fine grid (time averaged).

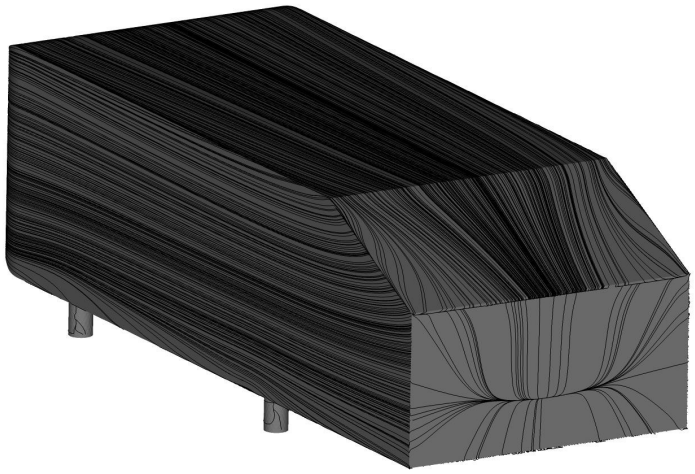

Figure 3-35: Ahmed body surface streamlines. Realizable K$-\varepsilon$ fine grid.

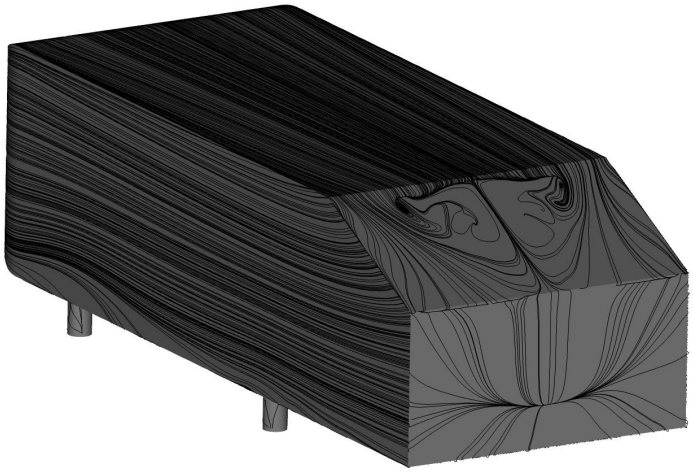

Figure 3-36: Ahmed body surface streamlines. K-ϖ SST fine grid.

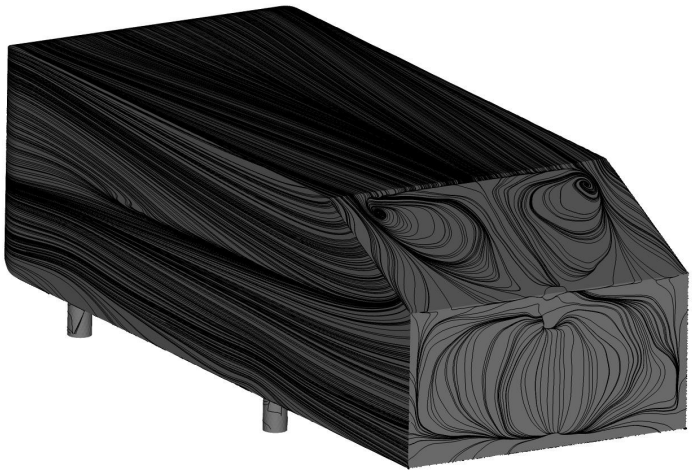

Figure 3-37: Ahmed body surface streamlines. LES fine grid (time averaged).

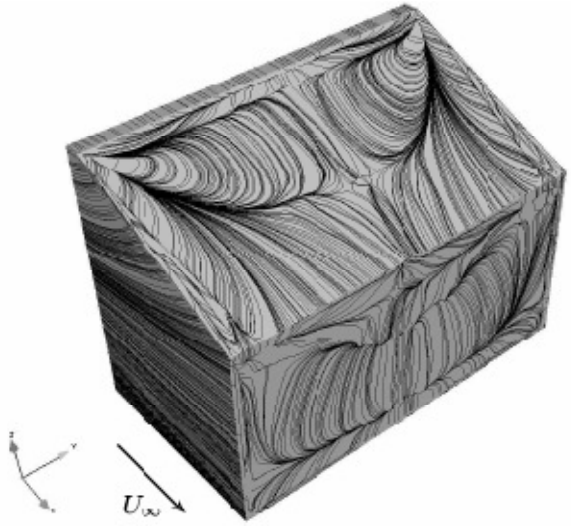

Figure 3-38: Ahmed body surface streamlines on 25° slant angle [23].

Figure 3-39: Oil film visualization on 25° slant angle [12].

Experiments have demonstrated that the flow initially separates over the top part of the slant angle and then re-attaches over the same surface due to the presence of the two longitudinal vortices. Looking at the streamlines plotted on the symmetry plane and at the surface streamlines over the slant angle, the Realizable K-ε shows attached flow over the entire slant angle. The flow then finally separates at the lower edge of the slant angle. In the K-ω SST the flow separates at the upper edge of the slant angle. The flow remains fully separated for the entire length of the slant angle and there are not areas of flow re-attachment. The LES simulation on the finest grid shows separation at the edge created by the Ahmed upper body surface and the slant angle surface as shown by K-ω SST. The flow then re-attaches towards the end of the slant angle and it separates at the lower end of the slant angle. Only the LES was able to predict the flow re-attachment over the slant angle but the length of the separation is over predicted in comparison to the data presented by Davidson et al [16,17]. Their LES simulations showed that the flow re-attaches before reaching the mid section of the slant angle. Their study also showed that the coarsening of the mesh resulted in an extension of the separation bubble. The over prediction of the separation region observed in this study is due to the fact that the mesh is quite coarse around the Ahmed body wall surfaces. It should be noted that the LES simulation conducted by Hinterberg et al [15] using a grid of around 18 million elements using a wall function approach similar to Werner and Wengle's faied to predict the reattachment region completely.

Observing the streamwise (U) velocity profiles graphs it is possible to notice that, as shown previously by the surface streamlines, the flow remains attached over the top surface of the Ahmed body and it then separates over the slant angle. The U velocity profiles taken from the experimental data start to show separation at the position x=-183. At this location the velocity profiles taken from the LES and K-ω SST are in good agreement with the experimental data as they both show separation. Realizable K-ε is in contrast with the simulations and experimental data by showing attached flow for the entire length of the slant angle. At the position x=-83 the velocity profiles coming from experimental data shows attached flow while the LES and K-ω SST still show detached flow. The latest position available from the experimental data is x=-3. At this position the U velocity plot shows that the flow is attached but LES and K-ω SST still show separated flow. The LES surface streamlines plot on the symmetry plane shows flow re-attachment. It is possible that the flow re-attaches in a position very close to x=0 which is where the slant angle meets the rear vertical Ahmed body surface.

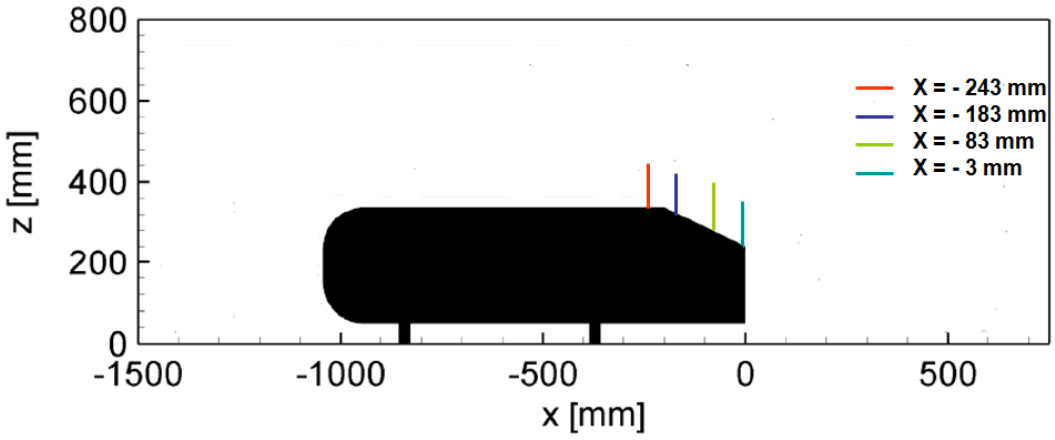

Figure 3-40 : Velocity profiles measurement locations.

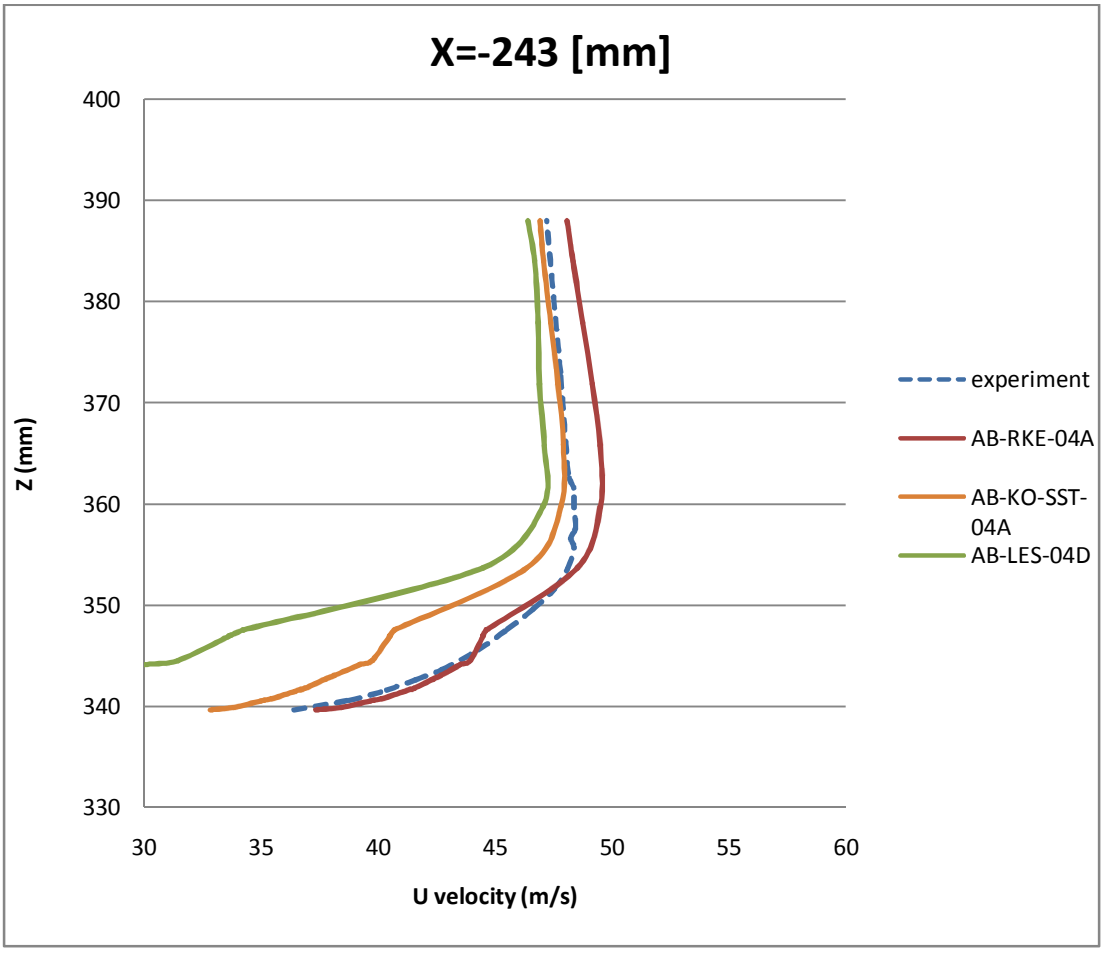

Figure 3-41 U velocity profiles on symmetry plane (y=0) at x=-243 (mm)

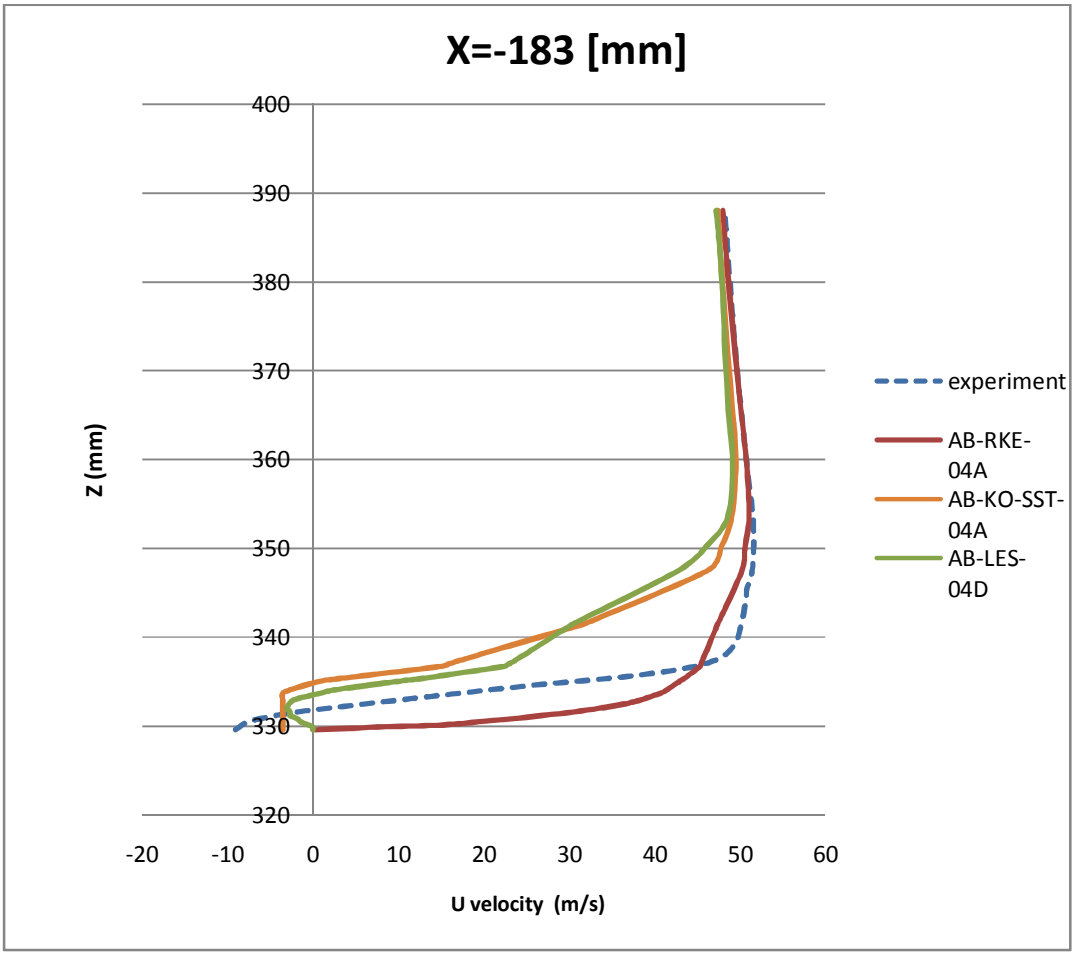

Figure 3-42 U velocity profiles on symmetry plane (y=0) at x=-183 (mm)

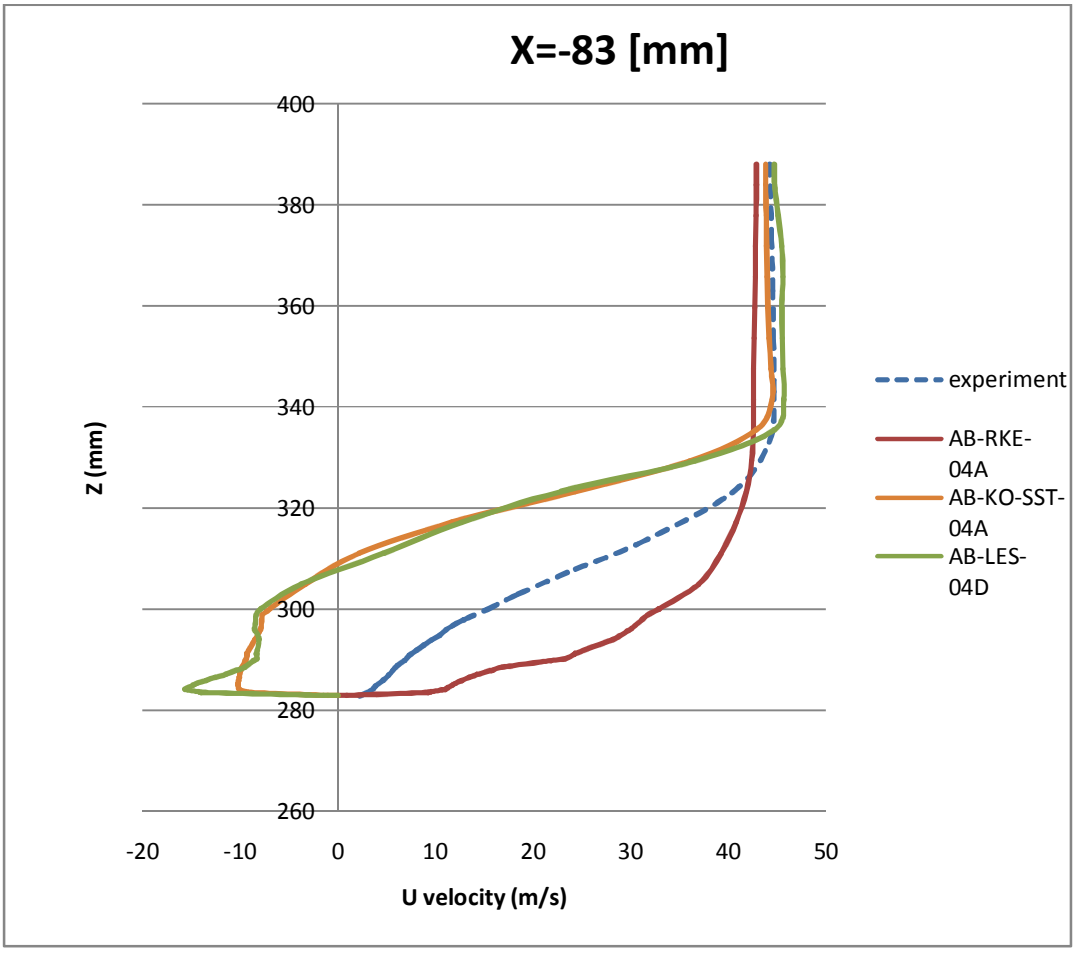

Figure 3-43 U velocity profiles on symmetry plane (y=0) at x=-83 (mm)

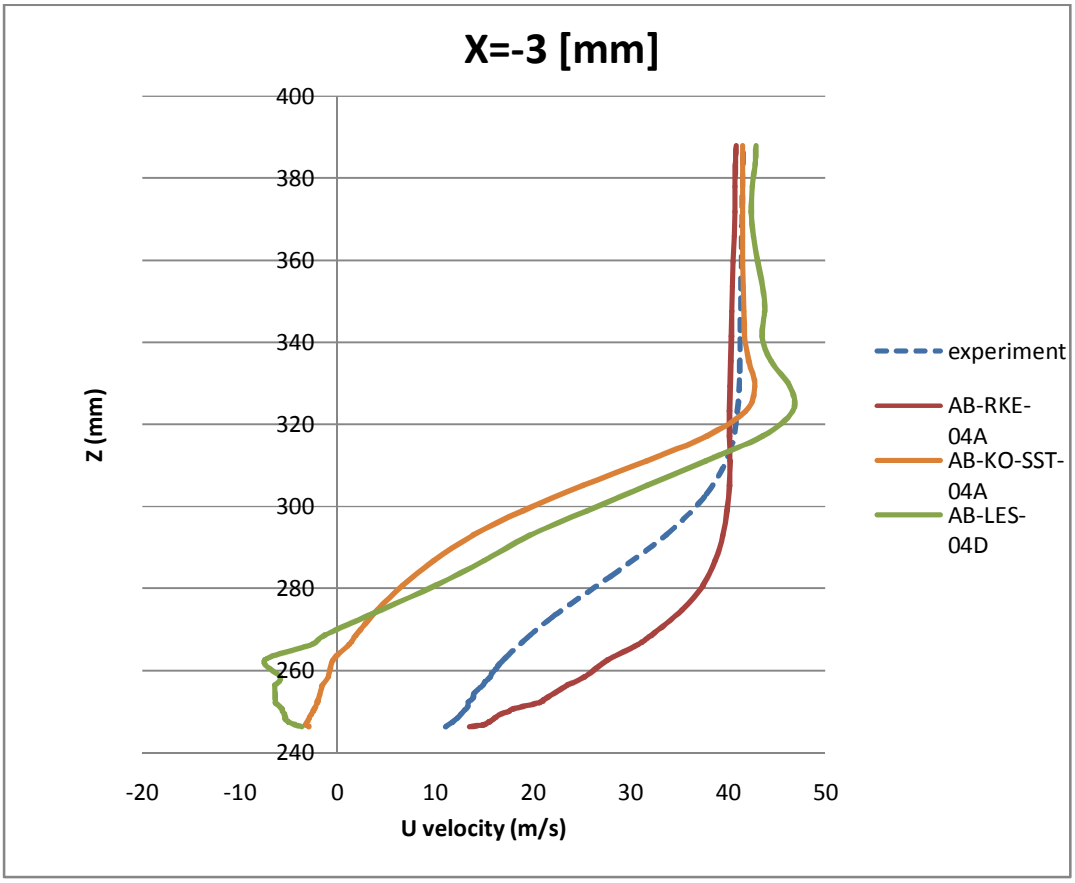

Figure 3-44 velocity profiles on symmetry plane (y=0) at x=-3 (mm)

Both RANS and LES models predict the presence of the two horseshoe vortices next to the Ahmed body rear vertical surface as described by S.R. Ahmed. The upper vortex is considerably bigger than the lower vortex. Compared to the Krjonovic' and Davidson [16,17] LES study, the K-ω SST over predicts the size of the upper vortex. In fact, the vortex seems to reach the upper edge of the slant angle. This is also in contrast with the flow description given by S.R. Ahmed. Previous studies presented at the ERCOFTACT using the K-ω SST turbulent model showed the same flow behaviour. The Realizable K-ε shows an upper vortex much more contained than in the one predicted by the K-ω SST model. The size of the upper and lower vortices is still over predicted. The LES simulation shows better agreement with previous LES studies. The upper vortex reaches the upper edge of the rear vertical face while the lower vortex is much

smaller than the upper vortex as shown by LES simulations conducted by Krajnovic' and Davidson[16,17].

Considering the distribution of turbulent kinetic energy (TKE) obtained on the symmetry plane the peak values is obtained at the rear of the Ahmed body where the flow is separated and in coincidence of the lower horseshoe vortex. The TKE values for the LES simulations were estimated using the RMS values. All the simulations shows peak TKE values around this separation area. The LES simulation also shows the same peak of TKE over the slant angle. Further in the wake at x=200 the Realizable K-ε shows a top TKE values of around 150 m^2/v^2. At the same location the K-ω SST and LES simulations still show top values of around 200 m^2/v^2. Overall, the TKE plots obtained from the K-ω SST and LES simulations are in better agreement with the experimental data.

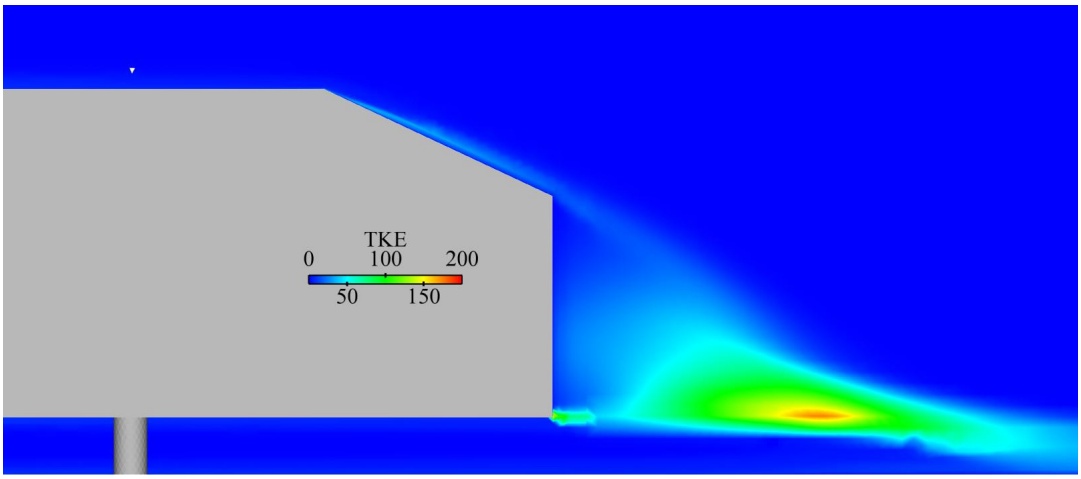

Figure 3-45: Turbulent Kinetic Energy on symmetry plane (y=0). Realizable k$-\varepsilon$ fine grid.

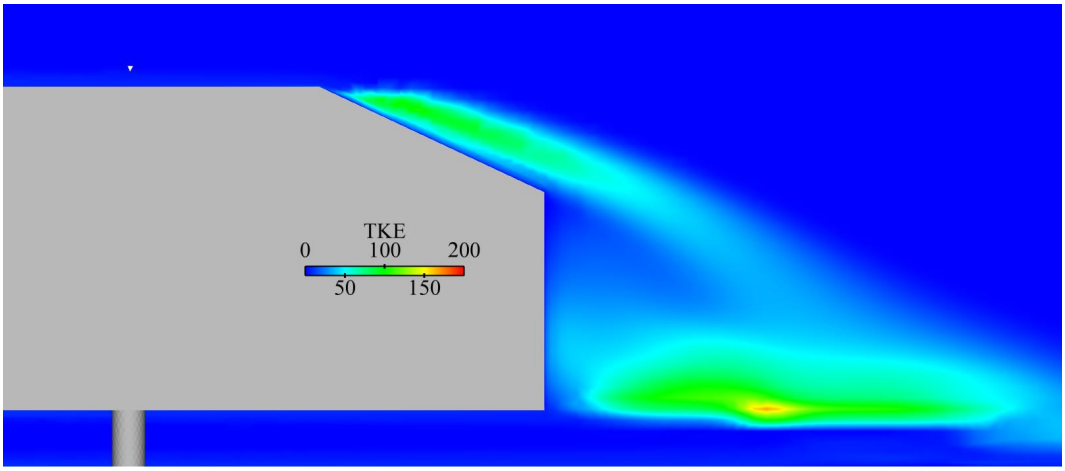

Figure 3-46: Turbulent Kinetic Energy on symmetry plane (y=0). K-ϖ SST fine grid.

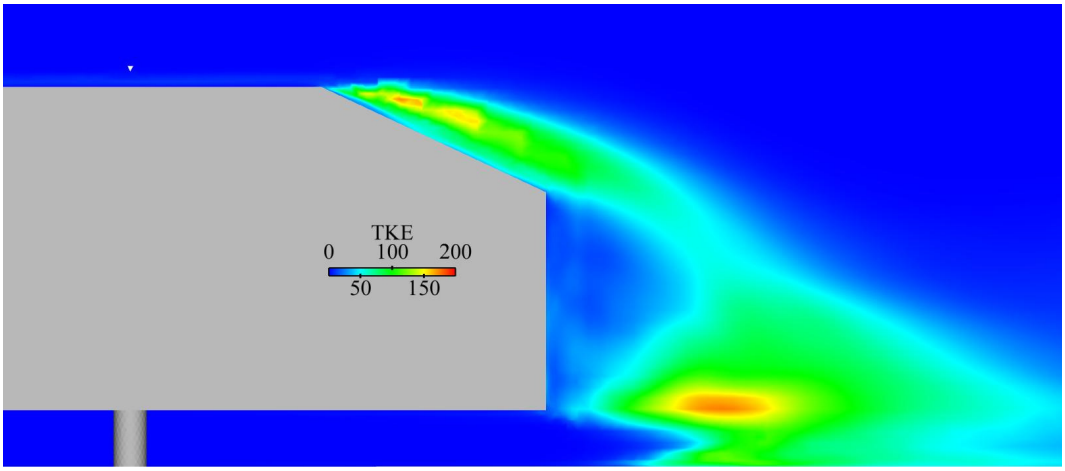

Figure 3-47: Turbulent Kinetic Energy on symmetry plane (y=0). LES fine grid (time averaged).

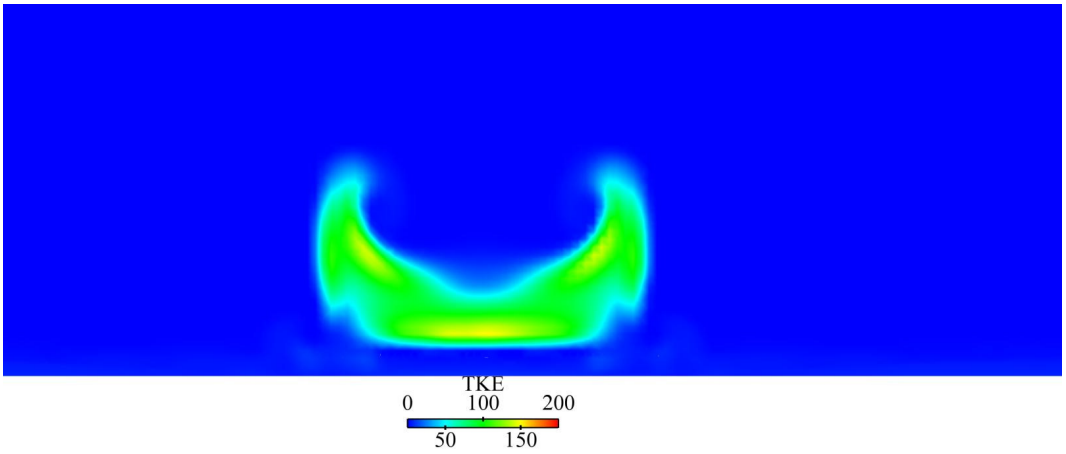

Figure 3-48: Turbulent Kinetic Energy at x=200. Realizable k$-\varepsilon$ fine grid.

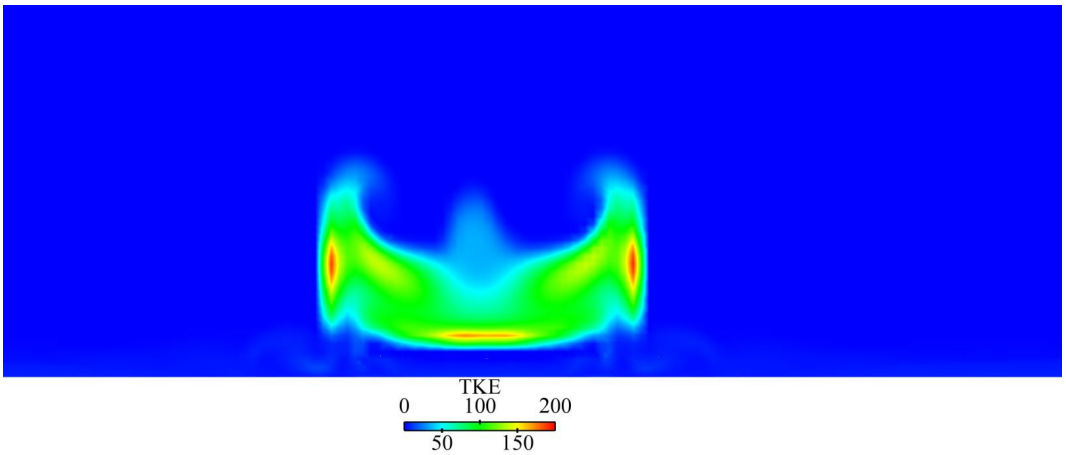

Figure 3-49: Turbulent Kinetic Energy at x=200. K-ϖ SST fine grid.

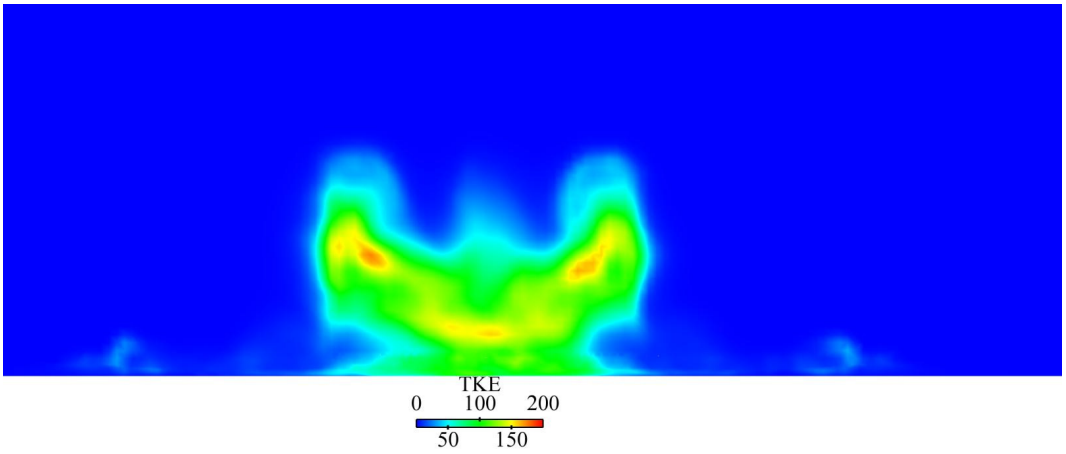

Figure 3-50: Turbulent Kinetic Energy at x=200. LES fine grid (time averaged).

3.5 Drag and lift coefficient comparison

Looking at table 3-2 and 3-3 is possible to state that the Cd values obtained with the Realizable k$-\varepsilon$ are consistent with the mesh refinement. In fact, the error between experimental and CFD data is 12.05 % for the coarse gird, 9.39 % for the medium grid and 6.59 % for the fine grid. The Cl values are not consistent with the mesh refinement, there is an error of 11.58 % for the coarse grid which then increases to around 18% using with medium and fine grids. For the other turbulence models tested, there is not consistency with the mesh refinement. Drag and lift coefficients for the LES simulation were obtained by averaging drag and lift data from 0.1s to 1.25s (fine grid) and from 0.1 to 0.67 s (medium gird). The medium grid obtained better agreement with the experimental data. The results obtained are still grid dependent.

Overall the K-ϖ SST model shows better agreement with the experimental data than the k$-\varepsilon$ models and LES model.

	AB-RKE	AB-RNG	AB-STD	AB-KO-SST	AB-LES
coarse grid	0.340	0.337	0.459	0.342	-
medium grid	0.330	0.305	0.501	0.311	0.344
fine grid	0.320	0.294	0.337	0.319	0.379
Graz wind tunnel	0.299	0.299	0.299	0.299	0.299
Error coarse gird	12.05%	11.18%	34.89%	12.62%	-
Error medium grid	9.39%	1.85%	40.29%	3.78%	13.20%
Error fine gird	6.59%	-1.60%	11.34%	6.33%	21.19%

Table 3-2: Cd values for the coarse, medium and fine grids.

	AB-RKE	AB-RNG	AB-STD	AB-KO-SST	AB-LES
coarse grid	0.390	0.163	0.384	0.339	-
medium grid	0.422	0.377	0.401	0.356	0.357
fine grid	0.421	0.381	0.341	0.363	0.371
Graz wind tunnel	0.345	0.345	0.345	0.345	0.345
Error coarse gird	11.58%	-111.26%	10.05%	-1.73%	-
Error medium grid	18.05%	9.56%	-1.08%	4.89%	3.24%
Error fine gird	18.15%	8.38%	13.92%	3.14%	7.08%

Table 3-3: Cl values for the coarse, medium and fine grids.

3.6 Pressure and viscous drag coefficient comparison

The viscous and pressure forces were not measured by the University of Graz nor by Lienhart and Becker [12]. Due to this the S.R. Ahmed original data [10] was used for comparison. Ahmed measured pressure drag for three configuration angles: 5°, 12.5° and 30°. The data obtained for the 25° angle configuration was not measured directly during the experiment but was obtained by interpolation.

Simulation	Pressure drag	Viscous drag	Total drag
AB-LES-04A	0.343	0.036	0.379
AB-KO-SST-04	0.273	0.047	0.320
AB-RKE-04A	0.271	0.050	0.321
Experiment (S.R. Ahmed)	0.241	0.057	0.298

Table 3-4: Viscous and pressure drag comparison. Fine grids.

All the models overestimate the pressure drag obtained by S.R Ahmed. The K-ω SST and Realizable K-ε gives the best accuracy in comparison to the experimental data obtained by S.R Ahmed. Also in terms of viscous drag these models give the best accuracy from the interpolated S.R. Ahmed values. The LES gave the worst accuracy by underestimating the viscous drag and by over predicting pressure drag. As explained by Krajnovic' and Davidson [16,17] the poor correlation obtained by the LES model is due to poor wall definition. This is especially true in this study were a wall function is used and Y+ is much higher than 1. Due to this is very likely that most of the eddies have been modelled by the sub grid scale model instead of been directly resolved.

3.7 Pressure coefficients comparison

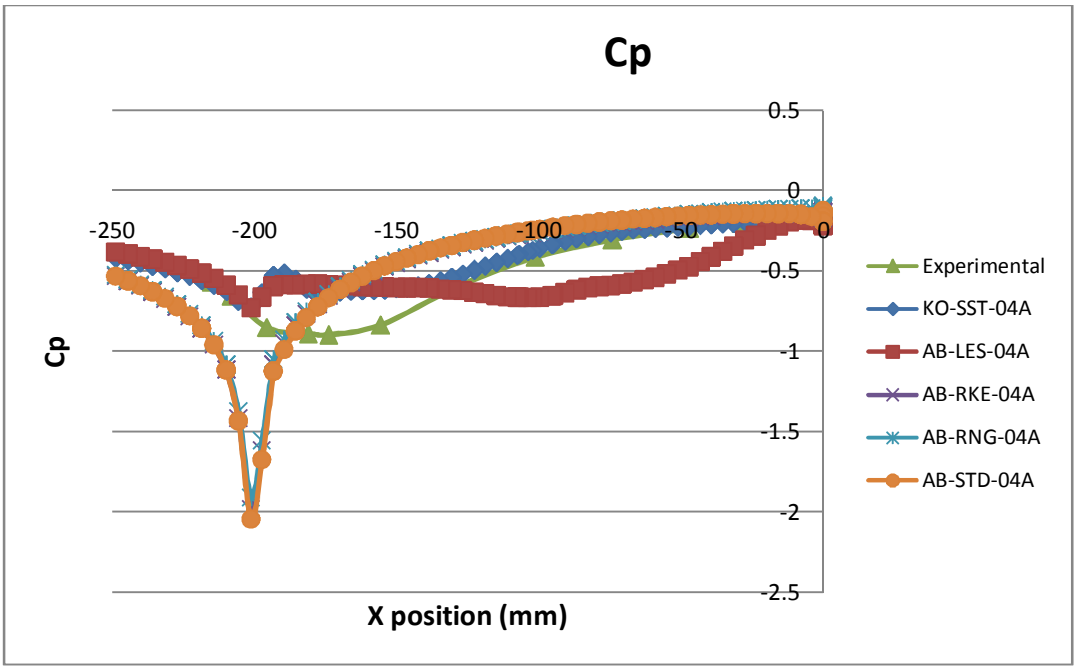

Figure 3-51: Pressure coefficient on slant angle at y=0

The LES and K-ω SST shows very good agreement with the experimental data up to X=-200 which is where the slant upper edge is located. The K-ε models are not in good agreement with the experiment, the predicted pressure is too low in comparison to the experimental data. All the models show a pressure drop at around x=-200. The K-ε models shows a Cp=-1.7 while LES and K-ω SST shows a Cp=-0.7. The different pressure drop between the simulations and the experimental data can be explained by the way the data was extracted from the simulations. In fact the pressure coefficient lines of the simulations were obtained by projecting a line on the rear slant surface at y=0. Due to this the number of data points is much higher than the ones obtained by the experiment. Krajnovic' and Davidson [16] suggested that the difference in pressure drop shown by the experimental and computational data could be due to the fact that the mesh of pressure tappets used in the experiment was too coarse. All the three LES simulations of their study showed a considerable pressure drop as shown by the K-ε models used in this study. Between x=-220 and x=-150 the K-ε models show a rapid pressure recovery which is not in good agreement with

the experimental data. At the same locations LES and K-ω SST over predicts the pressure coefficient. Soon after x=-150 the K-ω SST shows very good agreement with the experimental data.

3.8 FFT analysis for the LES simulations

Fast Fourier Transform was applied to the Cd history signal of both meshes, the medium grid showed a peak at around 1 Hz while the fine grid showed a peak at 15 Hz. These frequencies correspond to a Strouhal number (St) of 0.009 (medium grid) and 0.13 (fine grid) respectively based on the square root of the Ahmed body frontal area. The St number of 0.13 obtained with the fine is in good agreement with the results obtained by Krajnovic' and Davidson [16,17]. Their LES simulation on a fine structured grid (16 million elements) showed two dominant frequency of the Cd signal corresponding to St = 0.13 and St = 0.26.

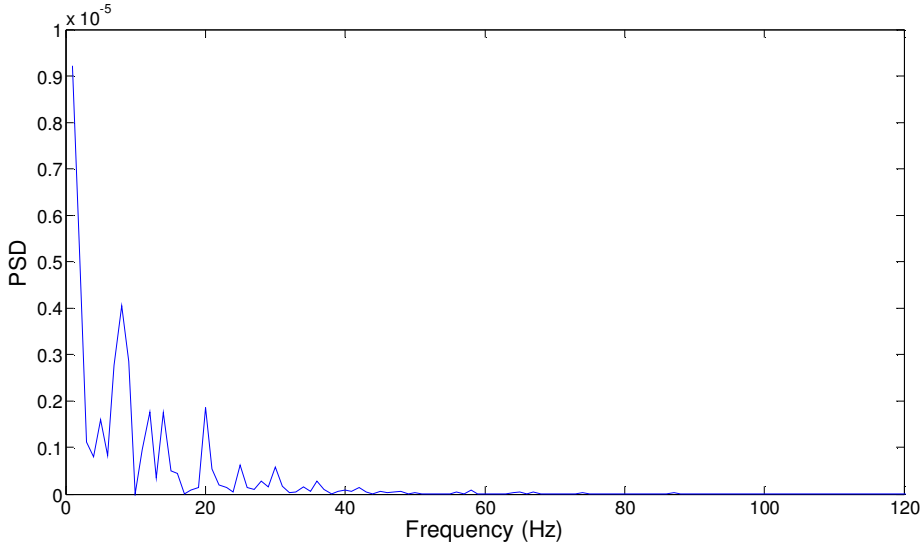

Figure 3-52: FFT on the Cd signal from medium grid.

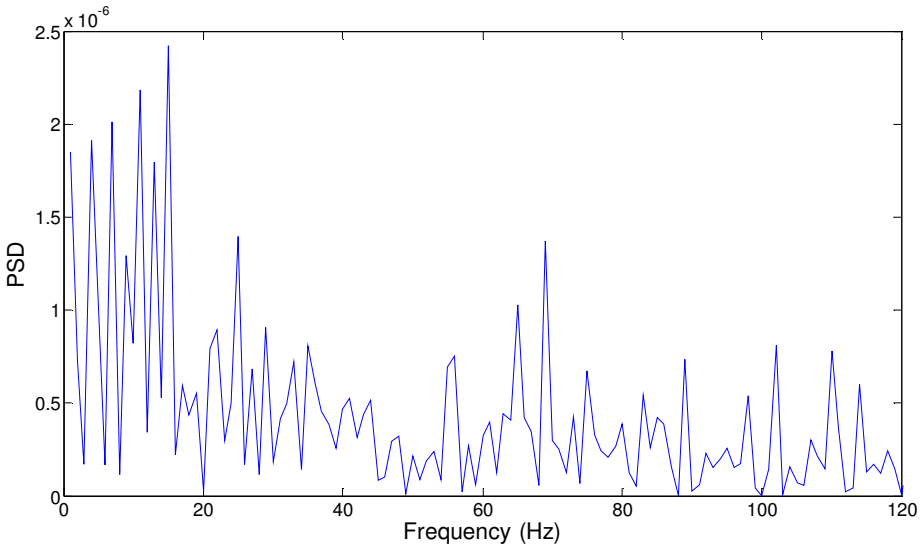

Figure 3-53: FFT on the Cd signal from fine grid.

Three temporal measurement points were located close to the Ahmed body's slant angle side edge as shown in Figure 3-54. Power spectral density of the time variation of the velocity magnitude showed a peak frequency of around 1Hz for the medium grid. The fine grid showed a peak frequency of around 1 Hz for point A and B, while a peak frequency of around 23 Hz was found at point C.

The velocity magnitude signal at point A was then plotted against Kolmogorov's slope. Observing the gradient it is possible to say that both grids are in good agreement with Kolmogorov's slope.

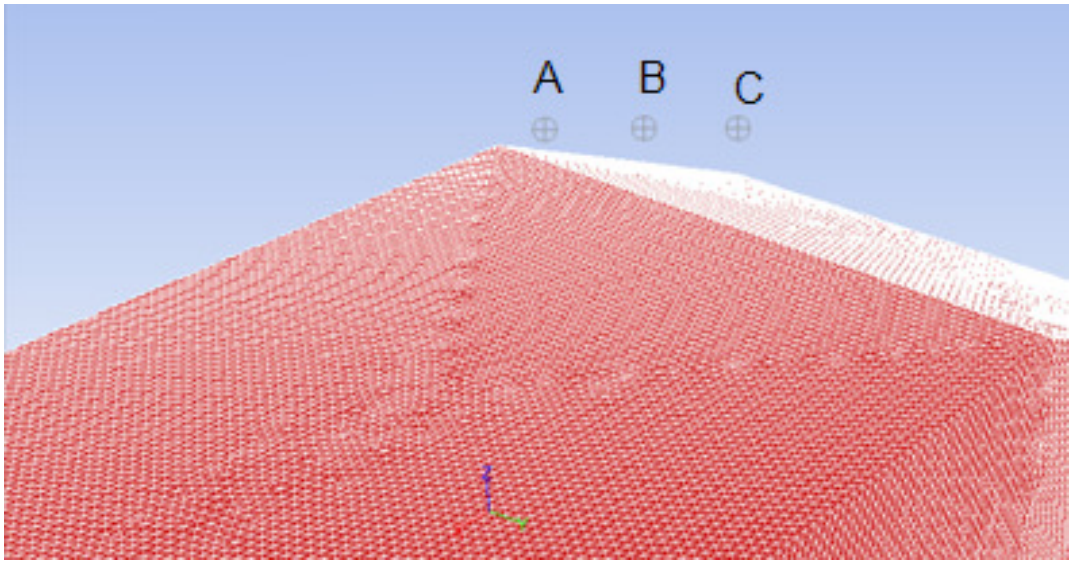

Figure 3-54: Velocity magnitude measurement points.

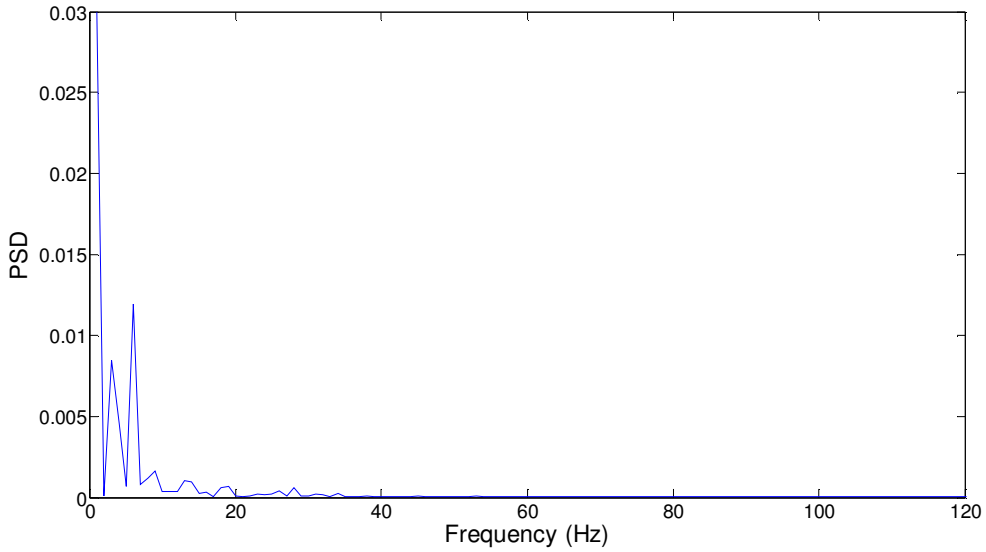

Figure 3-55: FFT on point A (medium grid).

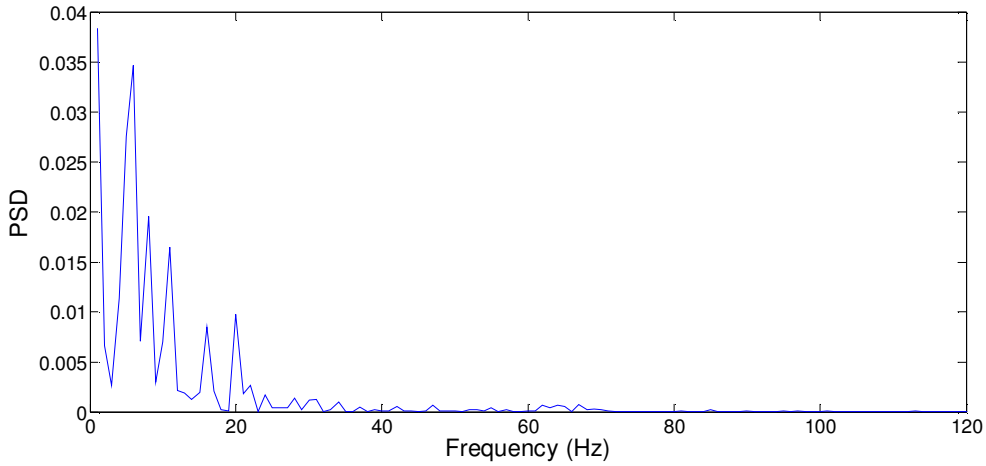

Figure 3-56: FFT on point A (fine grid).

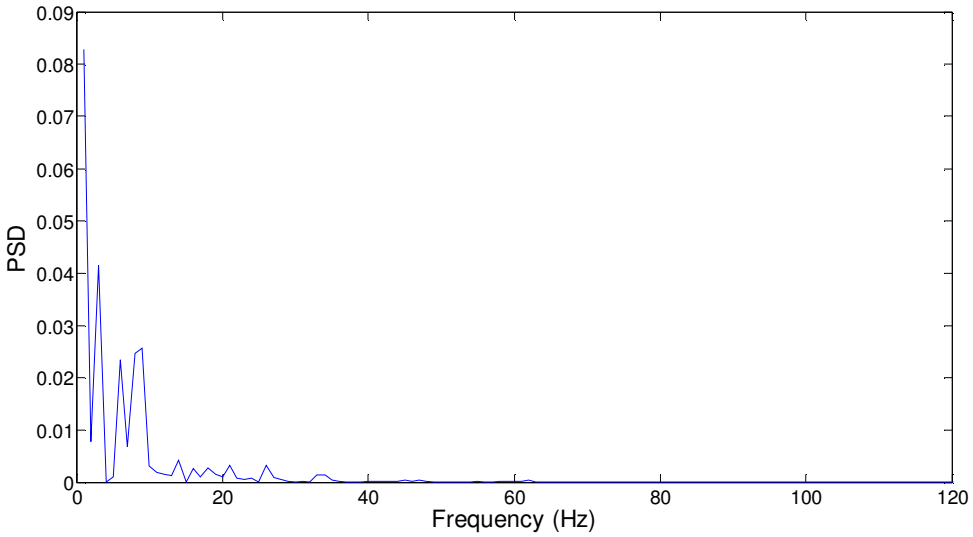

Figure 3-57: FFT on point B (medium grid).

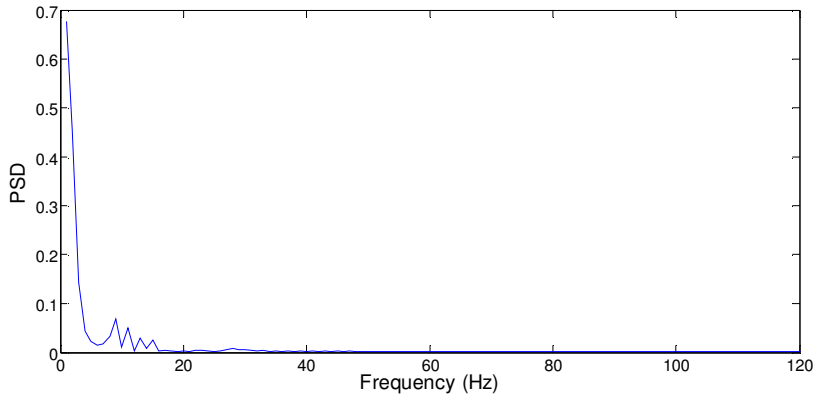

Figure 3-58: FFT on point B (fine grid).

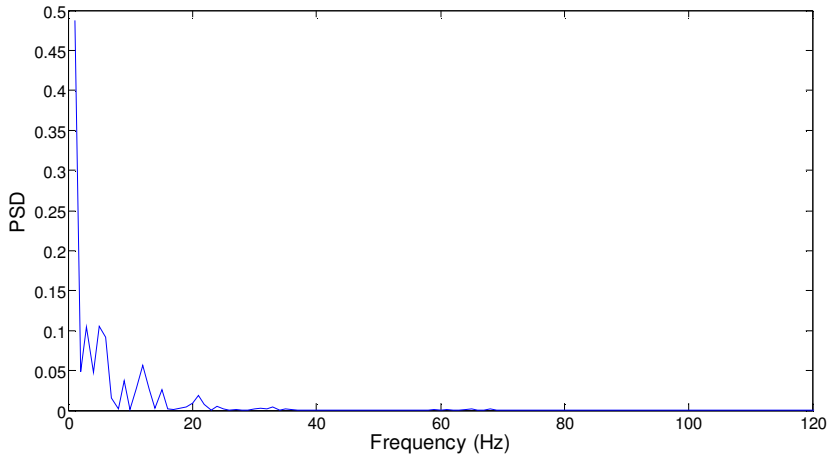

Figure 3-59: FFT on point C (medium grid).

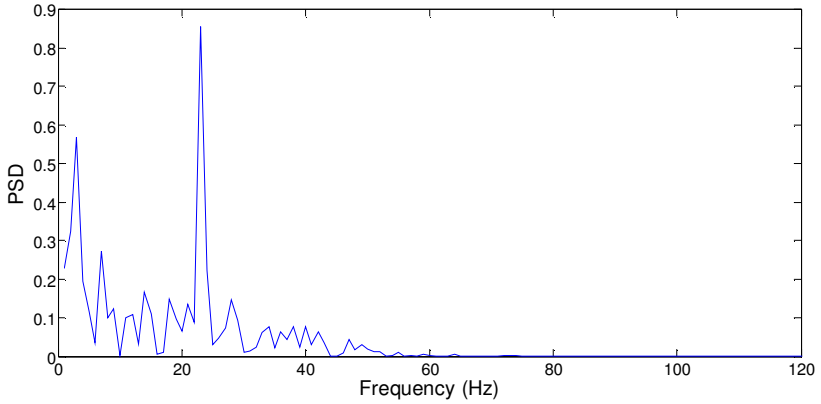

Figure 3-60: FFT on point C (fine grid).

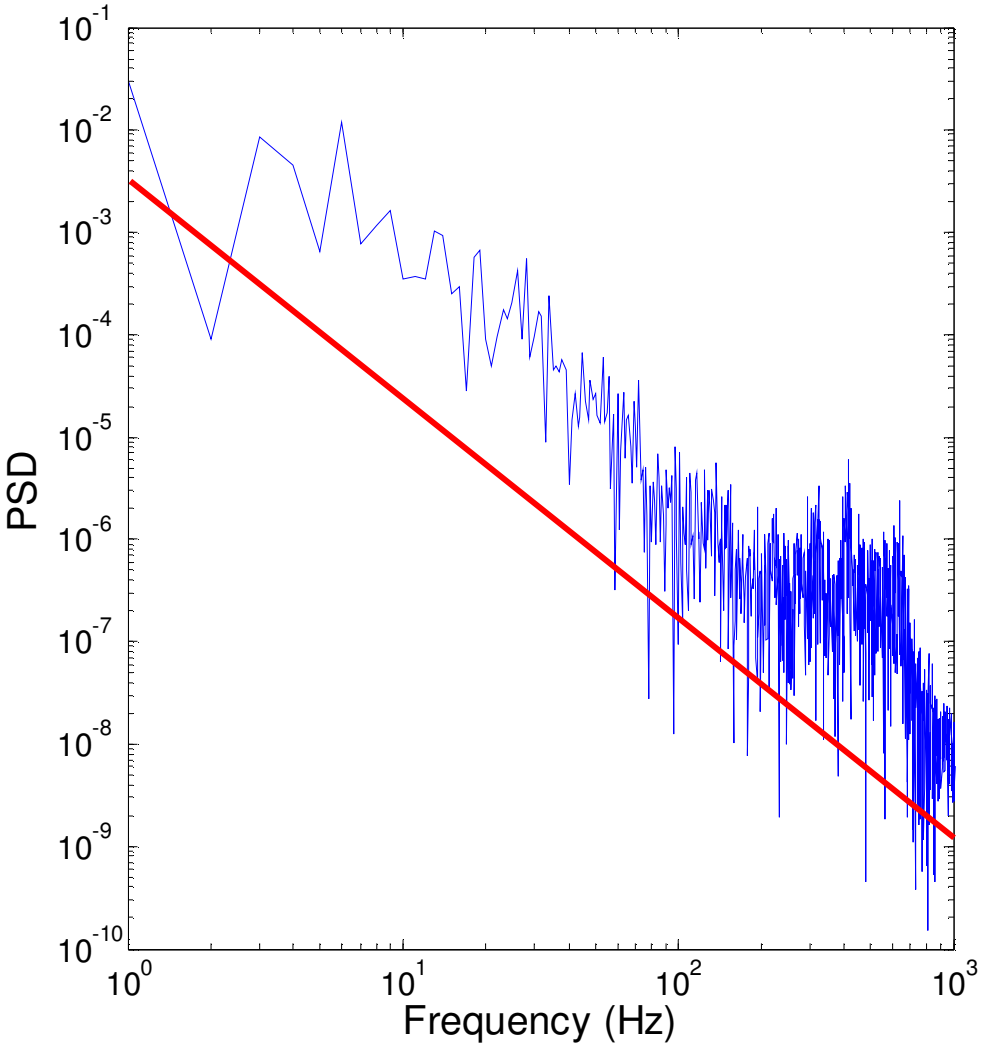

Figure 3-61: Kolmogorov slope (red line) compared to the velocity signal at point A. Medium grid.

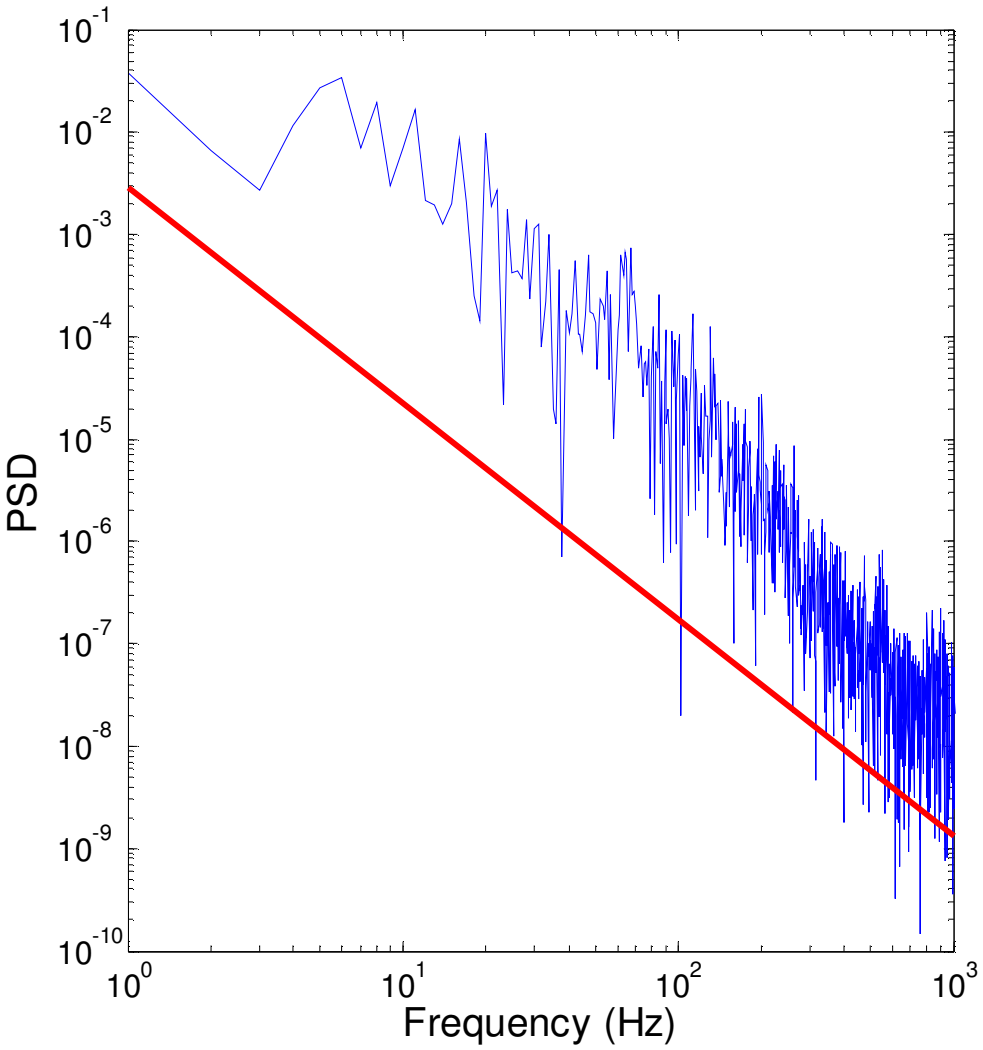

Figure 3-62: Kolmogorov slope (red line) compared to the velocity signal at point A. Fine grid.

3.9 Computational costs.

Automotive manufacturers and motorsport organizations can count on HPC facility with several thousand cores. Although more than one hundred cores is used for a CFD run, the computational time is still a dominant factor when considering a turbulence model approach. In order to compare the computational time required, the simulations using the fine grid resolution were

run on the same hardware. The CPUs were Xeon 5570 running with a LINUX operating system and using FLUENT 12 as a solver. The timing reported in the table below does not take into account reading and writing operations.

Table 3-5 Computational time requirement

Run	Number of iterations/time-steps	Total cpu time
AB-RKE-04A	5000	487597.13 s
AB-RNG-04A	5000	509811.72 s
AB-STD-04A	5000	479541.72 s
AB-KO-SST-04A	5000	582344.29 s
AB-LES-04D	2500	4237233.92 s

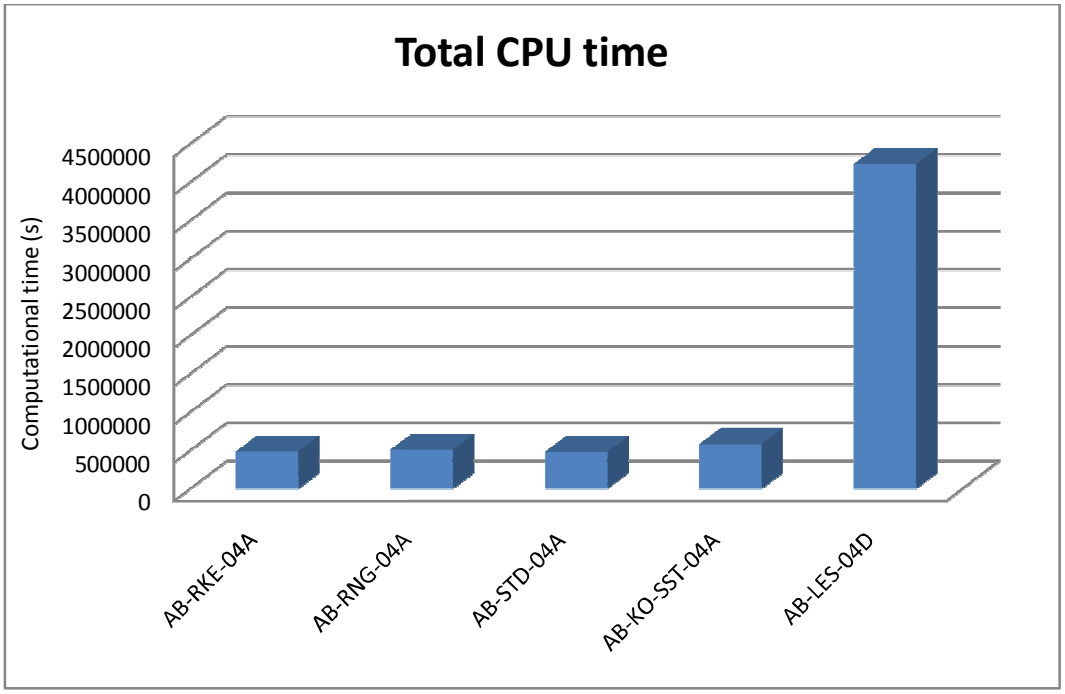

Figure 3-63 CPU time comparison

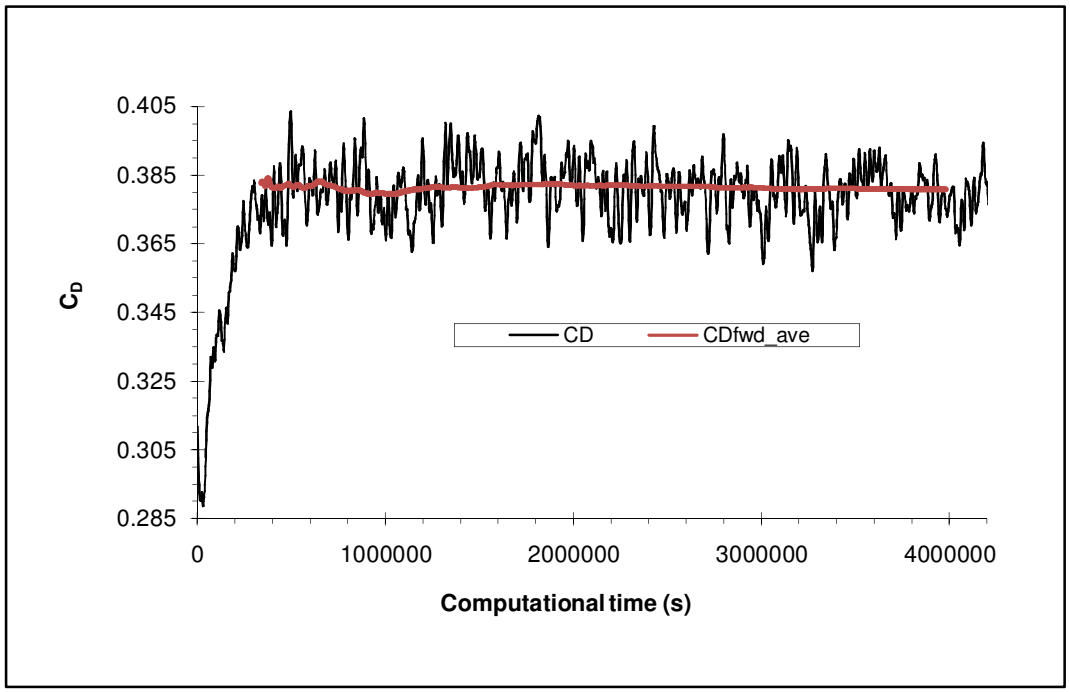

Figure 3-64 Drag coefficient (Cd) and forward averaged of Cd signal against computational time

Using the RANS models on 8 cores, the computational time required vary from around 16 hours to 20 hours of simulation only time. For the LES simulation, the computational time required was around 6 days. Note to mention that the LES model on the finest grid was run up to 1.25 seconds with a CFL value of around 35 and the flow field was initialized from a previous RANS simulation. As expected the computational time required for the LES simulation is several times higher than the RANS simulations. A more conservative CFL value of 1 and without flow initialization would most likely extent the simulation time to several weeks. In terms of drag and lift coefficients the K-ω SST model showed better correlation with the experimental data. Computationally inexpensive, especially when compared to LES simulation, this is the model that offers the best ratio between accuracy and computational time.

4 Conclusion and Future work

This thesis investigated the applicability and scalability of RANS and LES turbulence models applied to the classical Ahmed body test case with the challenging 25° slant angle configuration. Three different grid resolutions were used for the simulations. A viscous hybrid mesh approach was used in order to be aligned with the most up to date mesh methodology used by automotive manufacturers and motorsport organizations. The standard wall function was adopted for all of the RANS simulations and the Werner and Wengle wall function was adopted for the LES simulations.

At the front-end of the Ahmed body both RANS and LES models correctly predict the presence of two longitudinal vortices between the ground and the lower surfaces. However, the models fail to predict separation and re-attachment regions on the front and side surfaces of the Ahmed body. The two rear longitudinal vortices are well predicted by all the simulations but the different turbulence model approach showed substantial differences in predicting the flow behaviour over the rear slant angle. Realizable K-ε predicts attached flow over the rear slant surface while K-ω SST predicts fully separated flow on the same region. The LES initially shows flow separation and then re-attachment at the lower edge of the slant surface as shown by experimental results and previous LES investigations. The separation over the slant is over predicted but overall the LES is in better agreement with the experimental data.

In terms of forces, the K-ω SST showed better agreement with the experimental data than the other turbulence models. In fact the drag coefficient with this model using the medium gird resolution is only 3.78% off the experimental data. In terms of lift coefficient the K-ω SST model still has the lead in comparison to the other RANS models and LES models. For the fine grid simulation this model shows an error of 3.14% when compared to the experimental data. In terms of pressure coefficient, the K-ω SST and LES under predict the peak pressure while the K-ε models over predict the pressure peak over the slant.

The frequency extracted from the drag coefficient signal from the LES simulations shows that the St number obtained from the fine grid is in good agreement with the LES simulations conducted by Krajnovic' and Davidson [16,17] . Both grids show good agreement with Kolmogorov theory.

Finally, in terms of computational requirements, the LES simulation is clearly more computationally expensive when compared to the RANS models. Even if a wall function was used and a previous RANS simulation was used to initialize the simulation, the LES needed around 6 days of simulation to simulate from 0 to 1.25s flow time. For reference, the K-ω SST model showed better drag and lift coefficient agreement with the experimental data and it required only 20 hours of simulations. It has to be said that computational time apart the LES showed a better agreement in terms of flow topology over the rear slant. In addition, the unsteady data coming from the LES simulations can be used for a better understanding of the flow around the vehicle and it can also be used for aero-acoustic analysis.

For future work, a suggestion may be to use the double precision solver for the fine grid resolution. It would be useful to see if this can improve the grid convergence of the RANS simulations and improve overall the accuracy of RANS and LES simulations when compared to experimental data. At the same time a computational time comparison can be made for the single/double precision solver settings. The LES with the medium grid resolution was run up to 0.67 s of simulation due to time constraints. The Cd signal showed a certain gradient after about 0.5 s of simulation. For further work more simulation time is needed in order to observe the gradient of the Cd signal. Finally, future work into the investigation of sub grid scale models would be of use.

REFERENCES

[1] W. Hucho, "Aerodynamics of Road Vehicles", Fourth Edition, Society of Automotive Engineers, Warrendale Pa, 1998.

[2] J.Katz, “Race car Aerodynamics - Designing for speed” Robert Bentley publishing, 2002.

[3] A. Kebler, “Simulation of Air Flow Around an Opel Astra Vehicle with Fluent”, JA132, Journal Articles by Fluent Software Users, 2001.

[4] P.Drage, A.Grabiel and G.Lindbichler, "Efficient Use of Computational Fluid Dynamics for the Aerodynamic Development Process in the Automotive Industry", AIAA 2008-6735.

[5] A.Scotto d’Apollonia, S.Contini, F.Mathey, Y.Ducret, “Large Eddy simulation of a semi Realistic Vehicle Shape under Crosswind Conditions”, 3rd European Automotive CFD Conference, Frankfurt, Germany, 2007.

[6] Reynolds, O. “An experimental investigation of the circumstances which determine whether the motion of water shall be direct or sinuous and the law of resistance in parallel channels”, Philosophical Transactions of the Royal Society, 174, p 935-982, 1883.

[7] L. F. Richardson. “Weather Prediction by Numerical Process”, Cambridge University Press, 1922.

[8] Kolmogorov, A.N. Local structure of turbulence in an incompressible fluid for very large Reynolds numbers, Doklady Acad Sci. USSR 31, 1941.

[9] H.K. Versteeg,W. Malalasekera “An Introduction to Computational fluid Dynamics - The finite Volume Method", Second Edition, 2007.

[10] S.R. Ahmed, G. Ramm, G. Faltin, “Some Salient Features of the Time Average Ground Vehicle Wake”, SAE paper 840300, SAE International Congress and Exposition, 1984.

[11] A.Spohn,P.Gillieron, "Flow Separations Generated by a Simplified Geometry of an Automotive Vehicle", IUTAM, 2000.

[12] H.Lienhart, C.Soots and S.Becker, “Flow and turbulence structures in the wake of a simplified car model (Ahmed Model)", SAE Techinical Paper 2003-01-0656, 2003.

[13] S.Kapadia, S.Roy, K.Wurtzler, "Detached eddy simulation over a reference Ahmed car model". AIAA paper no.2003-0857, 2003.

[14] G. Martinat, R. Bourguet, Y. Hoarau, F. Dehaeze, B. Jorez, and M. Braza, "Numerical simulation of the flow in the wake of Ahmed body using Detached Eddy Simulation and URANS modelling", Notes on Numerical Fluid Mechanics. vol. 97, 2008.

[15] C. Hinterberger, M. García-Villalba, W. Rodi, "Large Eddy Simulation of flow around the Ahmed body", "Lecture Notes in Applied and Computational Mechanics / The Aerodynamics of Heavy Vehicles: Trucks, Buses, and Trains", R. McCallen, F. Browand, J. Ross (Eds.), Springer Verlag, ISBN: 3-540-22088-7, 2004.

[16] S.Krajnović, S.Davidson “Flow around a Simplified Car, Part1:Large Eddy Simlation”, Journal of Fluids Engineering, 2005.

[17] S.Krajnović, S.Davidson, “Flow around a Simplified Car, Part2: Understanding the Flow”, Journal of Fluids Engineering, 2005.

[18] E.Shapiro Dr., “CFD for Automotive flows :CFD Process”, Department of Fluid Mechanics and Computational Science, Cranfield University, 2011.

[19] ANSYS FLUENT 12 Theory Manual.

[20] Tennekes, H. and Lumley J.L., “A First Course in Turnulence”, MIT Press Cambridge MA., 1972.

[21] Gaylard, A., Private Communication, Jaguar Land Rover, 2011.

[22] D. B. Sims-Williams and R. G. "Experimental investigation into unsteadiness and instability in passenger car aerodynamics", SAE Paper 980391, 1998.

[23] S.Krajnovic’, L.Davidson,"Large-Eddy Simulation of the Flow Around Simplified Car Model", SAE Paper No. 2004-01-0227, Detroit, USA, 2004.

APPENDICES

Appendix A Simulations parameters

A.1 Realizable K-E simulations parameters

Solution Methods	
Pressure-Velocity Couplings	SIMPLEC
Gradient	Green-Gauss Cell Based
Pressure-Velocity Couplings	standard
Momentum	Third-Order MUSCL
Turbulent Kinetic Energy	Third-Order MUSCL
Turbulent Dissipation Rate	Third-Order MUSCL
Specific Dissipation Rate	N/A
Transient Formulation	N/A
Solution controls	
Pressure	0.2
Density	1
Body Forces	0.5
Momentum	0.5
turbulent Kinetic Energy	0.5
Turbulent Dissipation Rate	0.5
specific dissipation rate	N/A
turbulent viscosity	0.5
Velocity inlet	
Velocity inlet	40 m/s
Turbulent Intensity(%)	0.2
Turbulent Viscosity Ratio	10
Pressure Outlet (Intensity and Viscosity Ratio)	
Backflow Turbulent Intensity (%)	0.2
Backflow Turbulent Viscosity Ratio	10

Table A-1: Solver settings. Realizable K-ε

A.2 Standard K-E simulations parameters

Solution Methods	
Pressure-Velocity Couplings	SIMPLEC
Gradient	Green-Gauss Cell Based
Pressure-Velocity Couplings	standard
Momentum	Third-Order MUSCL
Turbulent Kinetic Energy	Third-Order MUSCL
Turbulent Dissipation Rate	Third-Order MUSCL
Specific Dissipation Rate	N/A
Transient Formulation	N/A
Solution controls	
Pressure	0.2
Density	1
Body Forces	0.5
Momentum	0.5
turbulent Kinetic Energy	0.5
Turbulent Dissipation Rate	0.5
specific dissipation rate	N/A
turbulent viscosity	0.5
Velocity inlet	
Velocity inlet	40 m/s
Turbulent Intensity(%)	0.2
Turbulent Viscosity Ratio	10
Pressure Outlet (Intensity and Viscosity Ratio)	
Backflow Turbulent Intensity (%)	0.2
Backflow Turbulent Viscosity Ratio	10

Table A-2: Solver settings. Standard K-ε.

A.3 RNG K-E simulations parameters

Solution Methods	
Pressure-Velocity Couplings	SIMPLEC
Gradient	Green-Gauss Cell Based
Pressure-Velocity Couplings	standard
Momentum	Third-Order MUSCL
Turbulent Kinetic Energy	Third-Order MUSCL
Turbulent Dissipation Rate	Third-Order MUSCL
Specific Dissipation Rate	N/A
Transient Formulation	N/A
Solution controls	
Pressure	0.2
Density	1
Body Forces	0.5
Momentum	0.5
turbulent Kinetic Energy	0.5
Turbulent Dissipation Rate	0.5
specific dissipation rate	N/A
turbulent viscosity	0.5
Velocity inlet	
Velocity inlet	40 m/s
Turbulent Intensity(%)	0.2
Turbulent Viscosity Ratio	10
Pressure Outlet (Intensity and Viscosity Ratio)	
Backflow Turbulent Intensity (%)	0.2
Backflow Turbulent Viscosity Ratio	10

Table A-3: Solver settings. RNG K-ε.

A.4 K-O SST simulations parameters

Solution Methods	
Pressure-Velocity Couplings	SIMPLEC
Gradient	Green-Gauss Cell Based
Pressure-Velocity Couplings	standard
Momentum	Third-Order MUSCL
Turbulent Kinetic Energy	Third-Order MUSCL
Turbulent Dissipation Rate	N/A
Specific Dissipation Rate	First-order Upwind
Transient Formulation	N/A
Solution controls	
Pressure	0.2
Density	1
Body Forces	0.5
Momentum	0.5
turbulent Kinetic Energy	0.5
Turbulent Dissipation Rate	
specific dissipation rate	0.8
turbulent viscosity	0.5
Velocity inlet	
Velocity inlet	40 m/s
Turbulent Intensity(%)	0.2
Turbulent Viscosity Ratio	10
Pressure Outlet (Intensity and Viscosity Ratio)	
Backflow Turbulent Intensity (%)	0.2
Backflow Turbulent Viscosity Ratio	10

Table A-4: Solver settings. K-ω SST.

A.5 LES simulations parameters

Solution Methods	
Pressure-Velocity Couplings	SIMPLEC
Gradient	Green-Gauss Cell Based
Pressure-Velocity Couplings	standard
Momentum	Bounded Central Differecing
Turbulent Kinetic Energy	N/A
Turbulent Dissipation Rate	N/A
Specific Dissipation Rate	N/A
Transient Formulation	Second Order Implicit
Solution controls	
Pressure	0.2
Density	1
Body Forces	0.5
Momentum	0.5
turbulent Kinetic Energy	N/A
Turbulent Dissipation Rate	N/A
specific dissipation rate	N/A
turbulent viscosity	N/A
Velocity inlet	
Velocity inlet	40 m/s
Turbulent Intensity(%)	N/A
Turbulent Viscosity Ratio	N/A
Pressure Outlet (Intensity and Viscosity Ratio)	
Backflow Turbulent Intensity (%)	N/A
Backflow Turbulent Viscosity Ratio	N/A

Table A-5: Solver settings. LES.

Appendix B Simulations Residuals

B.1 Coarse grid

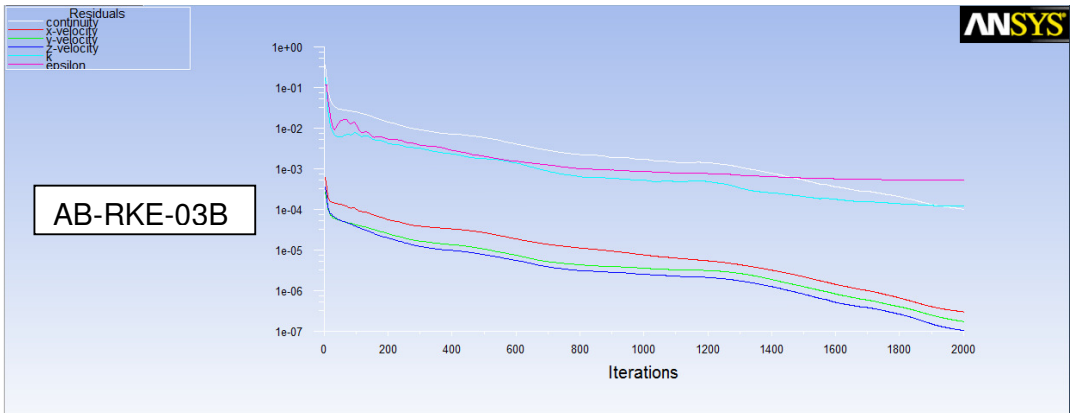

Figure B-1: Simulation residuals. Realizable K-ε coarse grid.

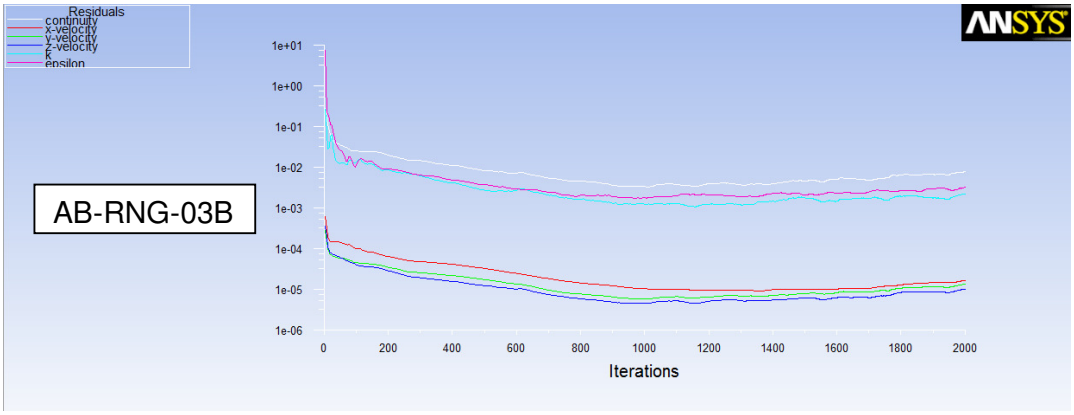

Figure B-2: Simulation residuals. RNG K-ε coarse grid.

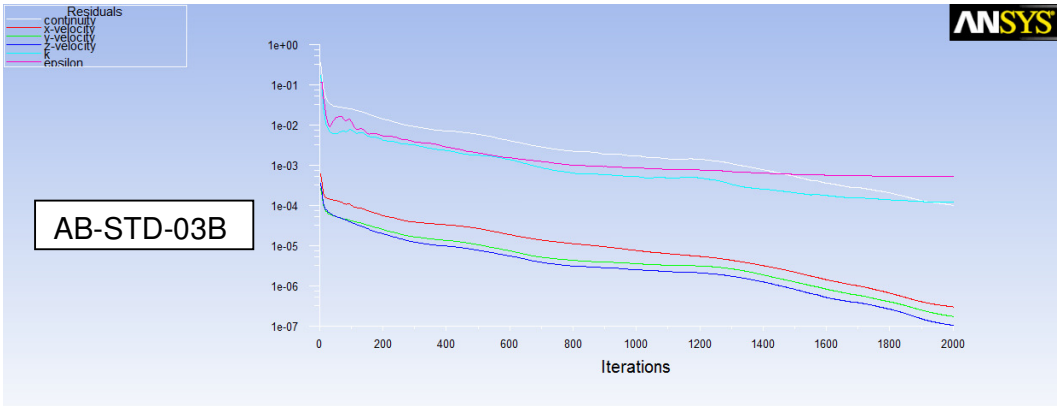

Figure B-3: Simulation residuals. Standard K-ε coarse grid.

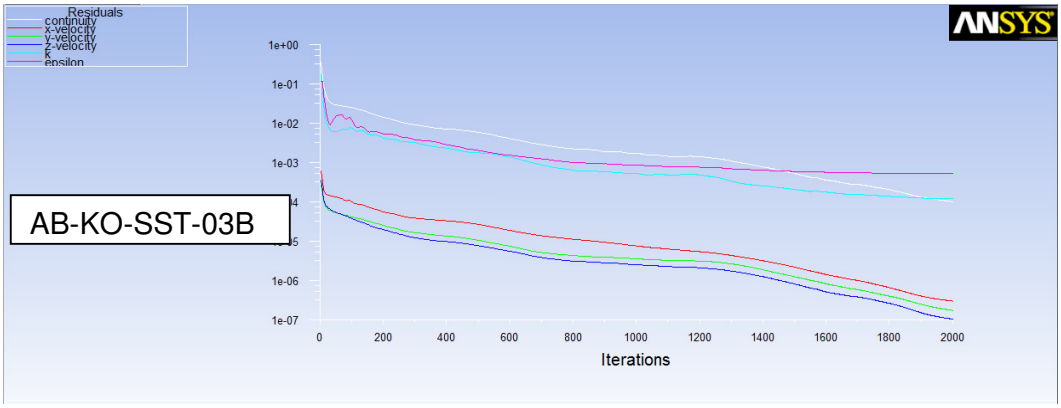

Figure B-4: Simulation residuals. K-ω SST coarse grid.

B.2 Medium grid

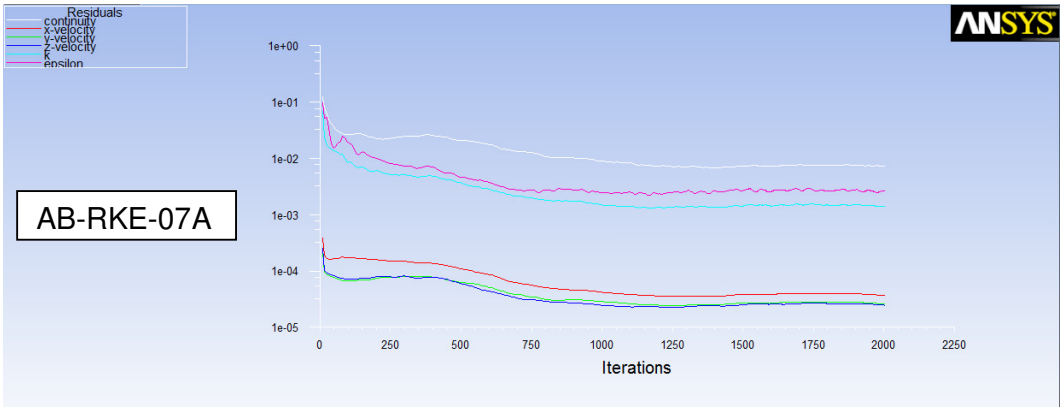

Figure B-5: Simulation residuals. Realizable K-ε medium grid.

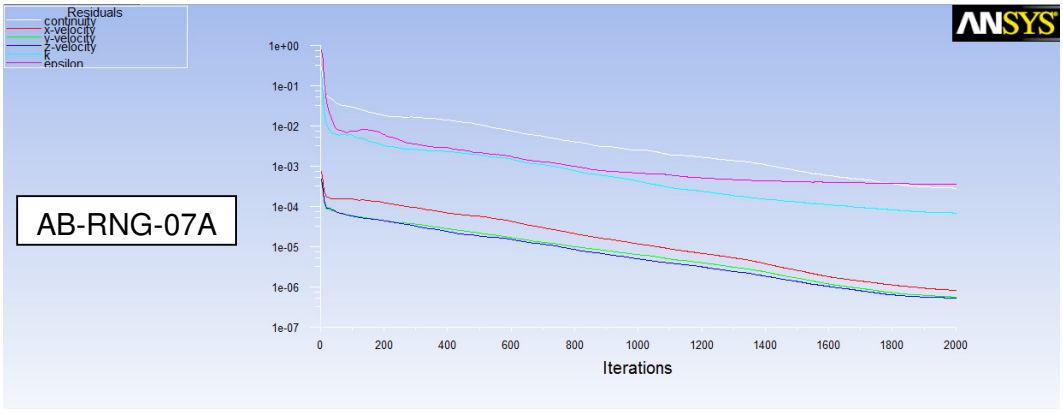

Figure B-6: Simulation residuals. RNG K-ε medium grid.

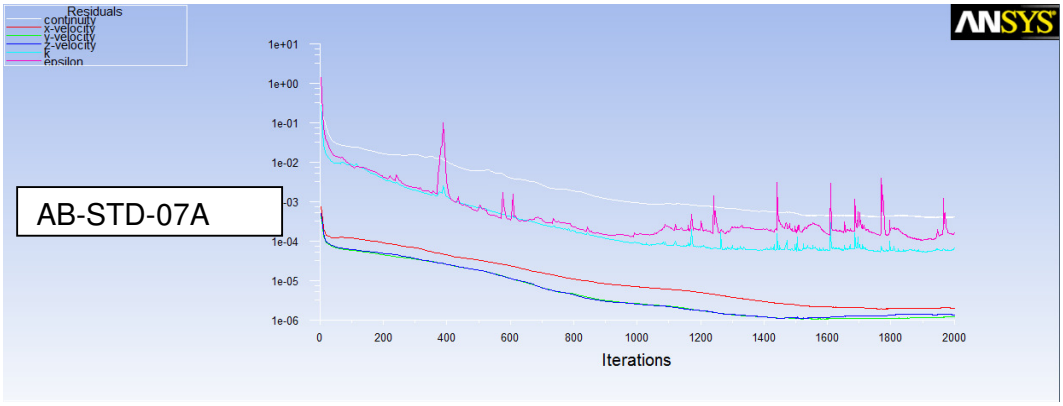

Figure B-7: Simulation residuals. Standard K-ε medium grid.

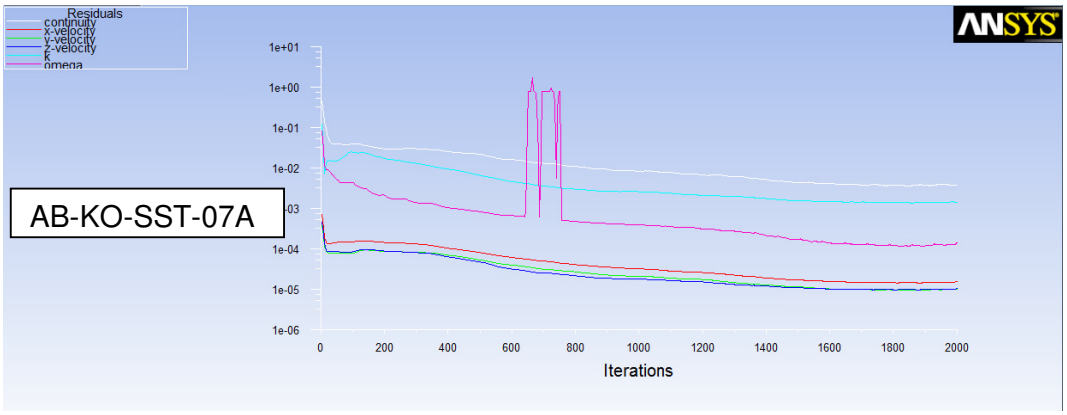

Figure B-8: Simulation residuals. K-ω SST medium grid.

B.3 Fine grid

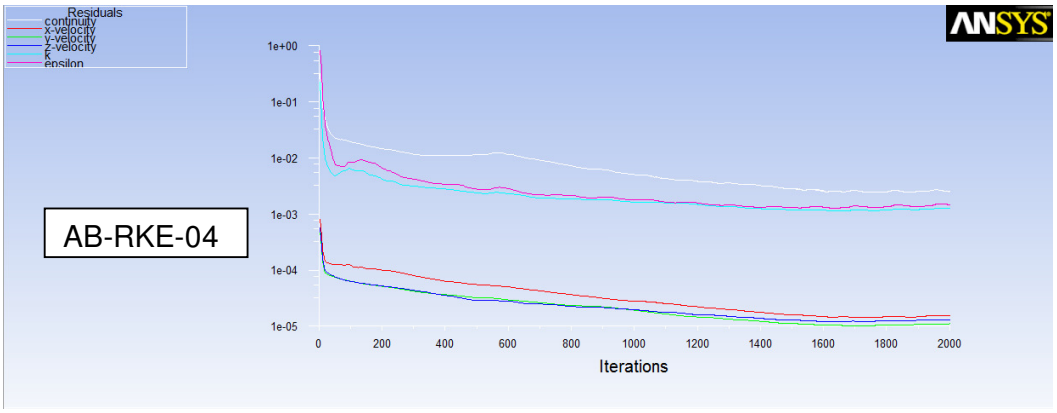

Figure B-9: Simulation residuals. Realizable K-ε fine grid.

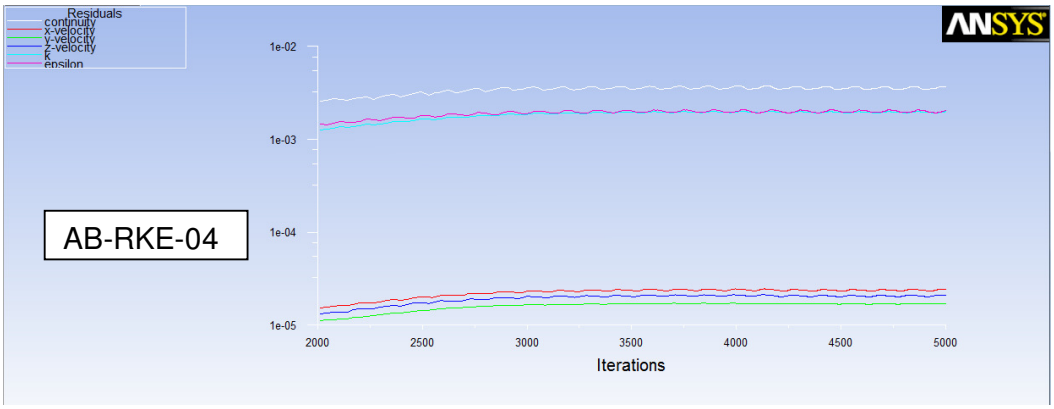

Figure B-10: Simulation residuals (from 2000 to 5000). Realizable K-ε fine grid.

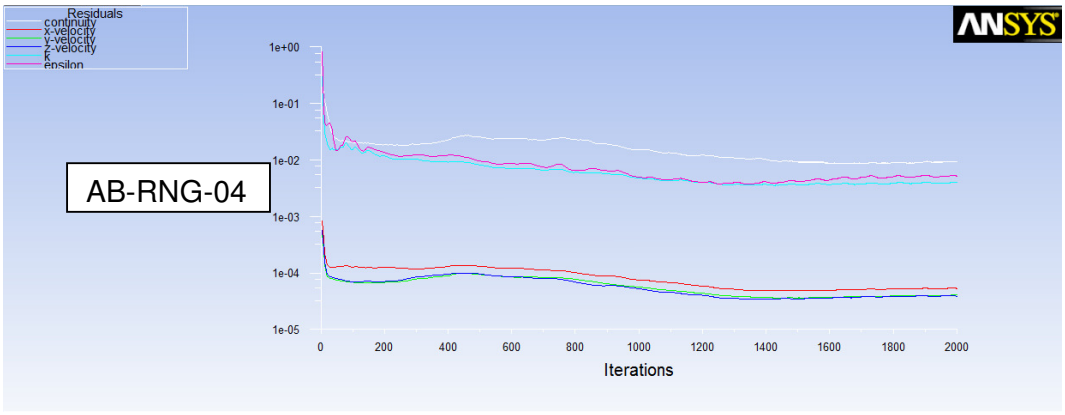

Figure B-11: Simulation residuals. RNG K-ε fine grid.

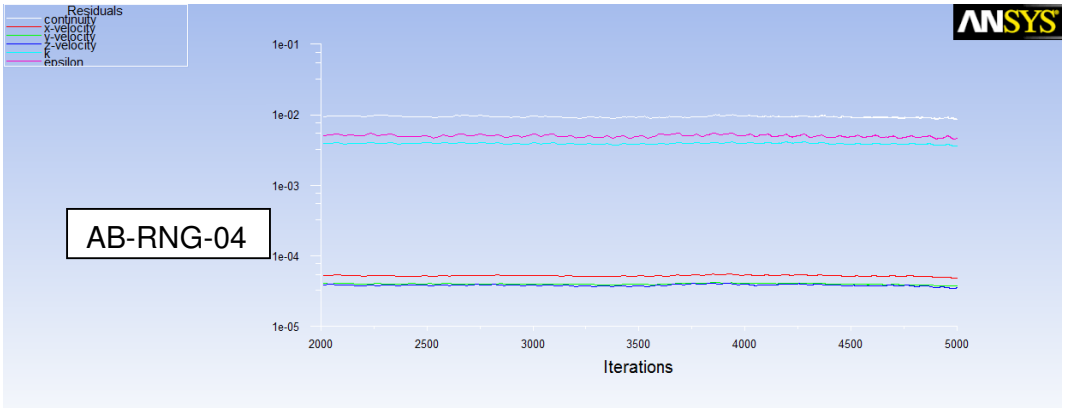

Figure B-12: Simulation residuals (from 2000 to 5000). RNG K-ε fine grid.

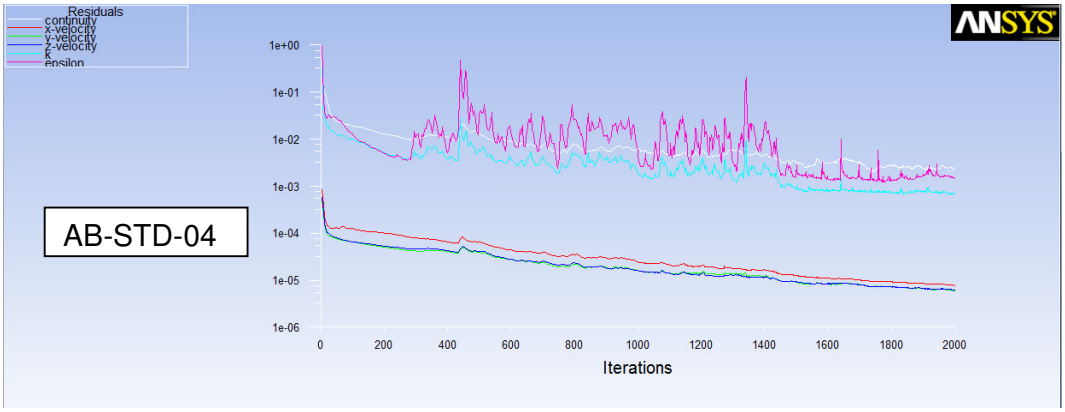

Figure B-13: Simulation residuals. Standard K-ε fine grid.

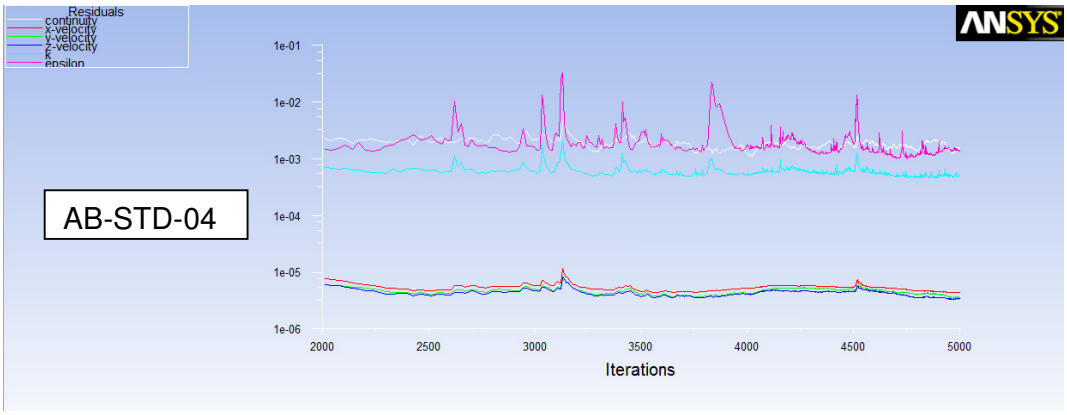

Figure B-14 : Simulation residuals (from 2000 to 5000). Standard K-ε fine grid.

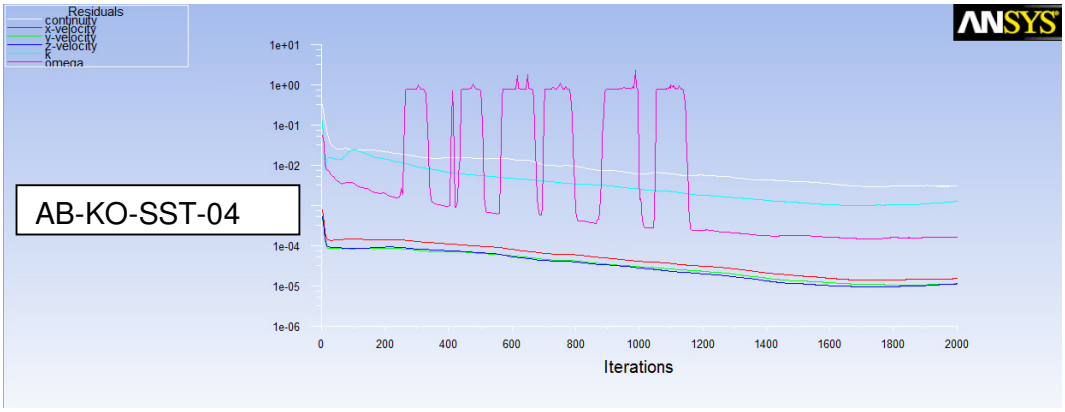

Figure B-15: Simulation residuals. K-ω SST fine grid.

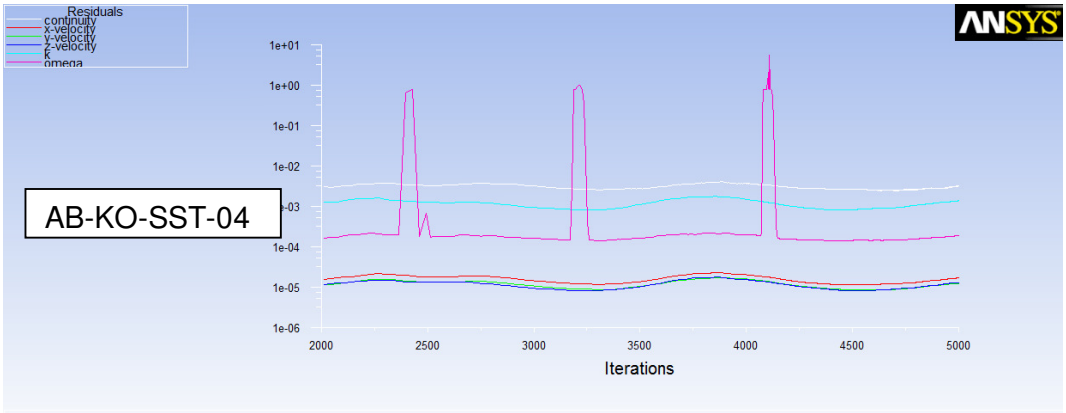

Figure B-16: Simulation residuals (from 2000 to 5000). K-ω SST fine grid.

Appendix C Streamwise velocity profiles

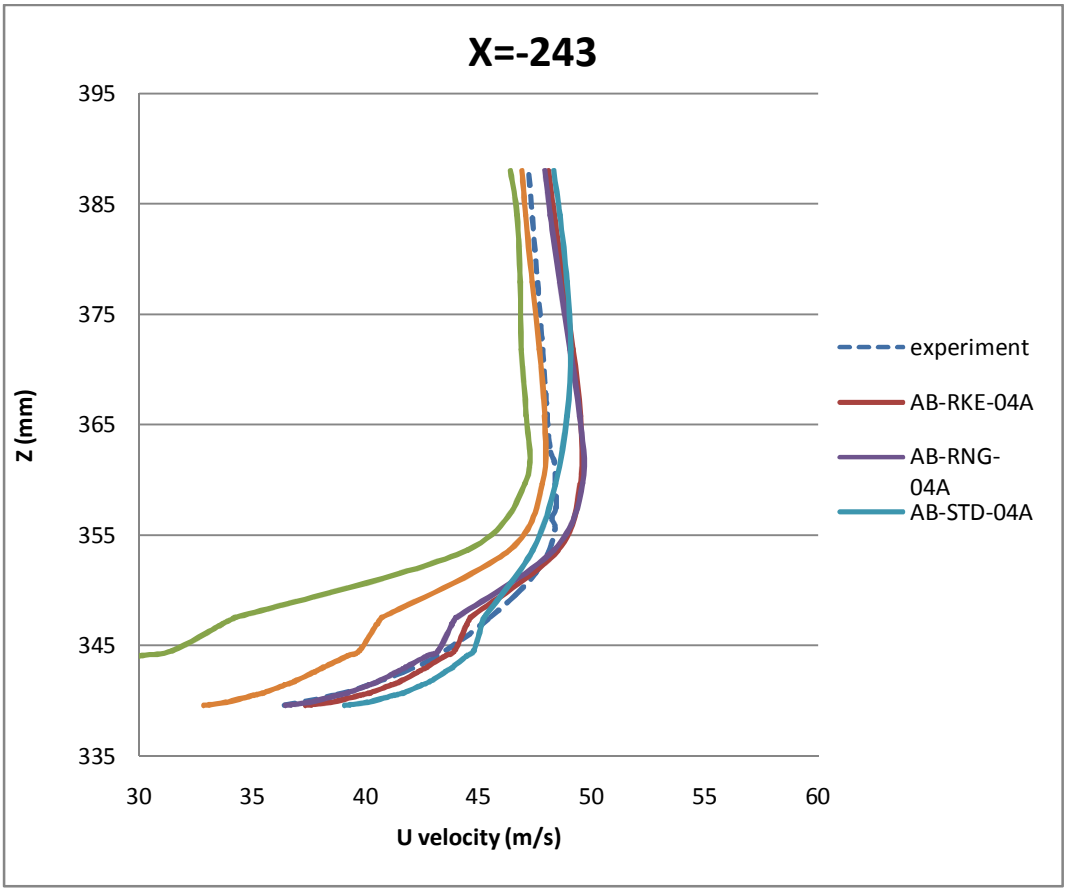

Figure C-1: U velocity profiles on symmetry plane (y=0) at x=-243.

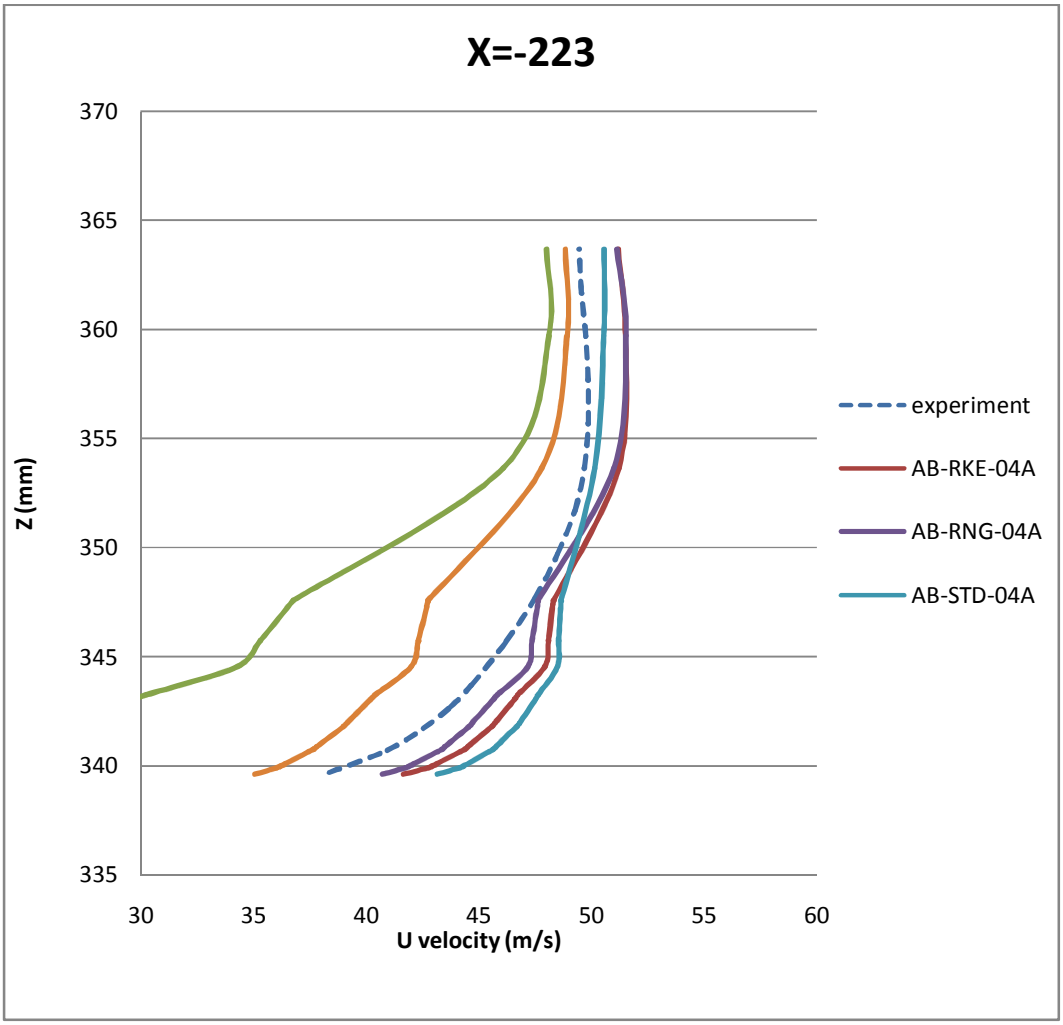

Figure C-2: U velocity profiles on symmetry plane (y=0) at x=-223.

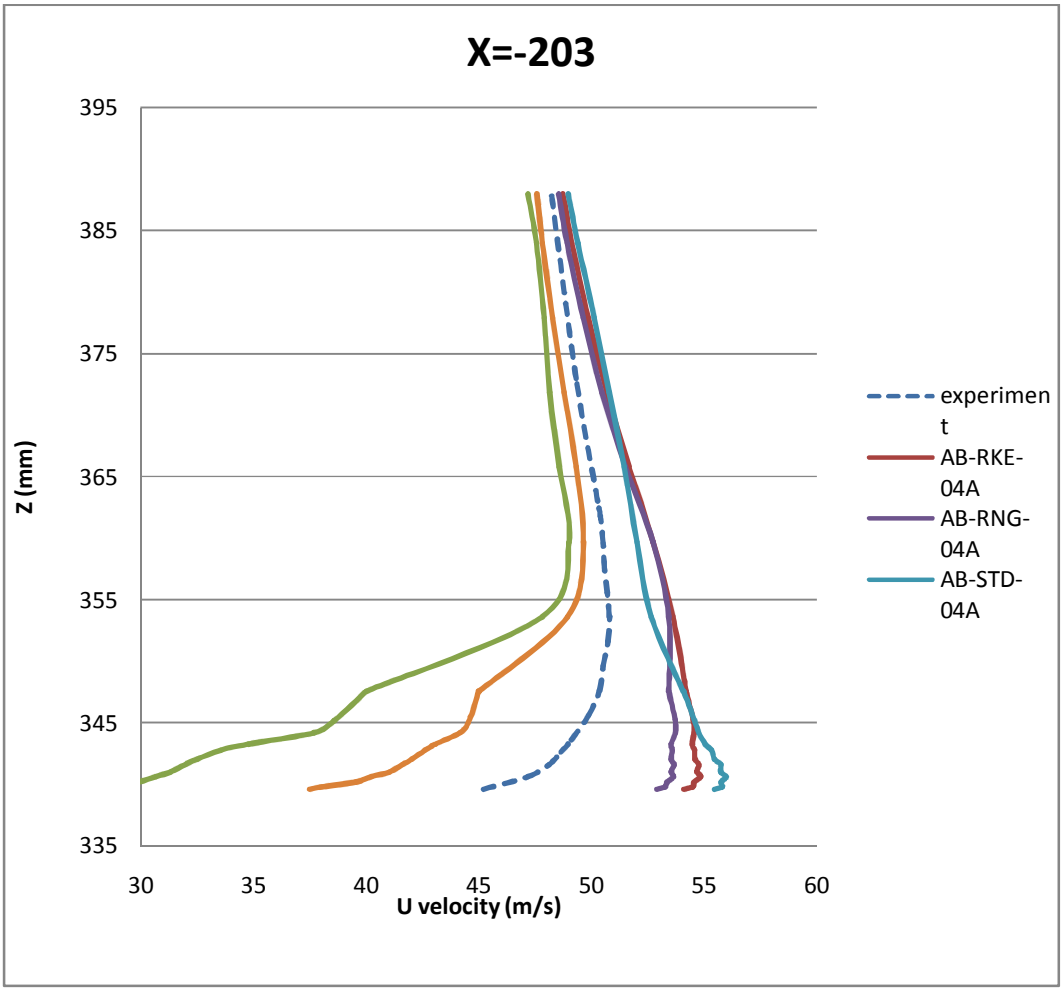

Figure C-3: U velocity profiles on symmetry plane (y=0) at x=-203.

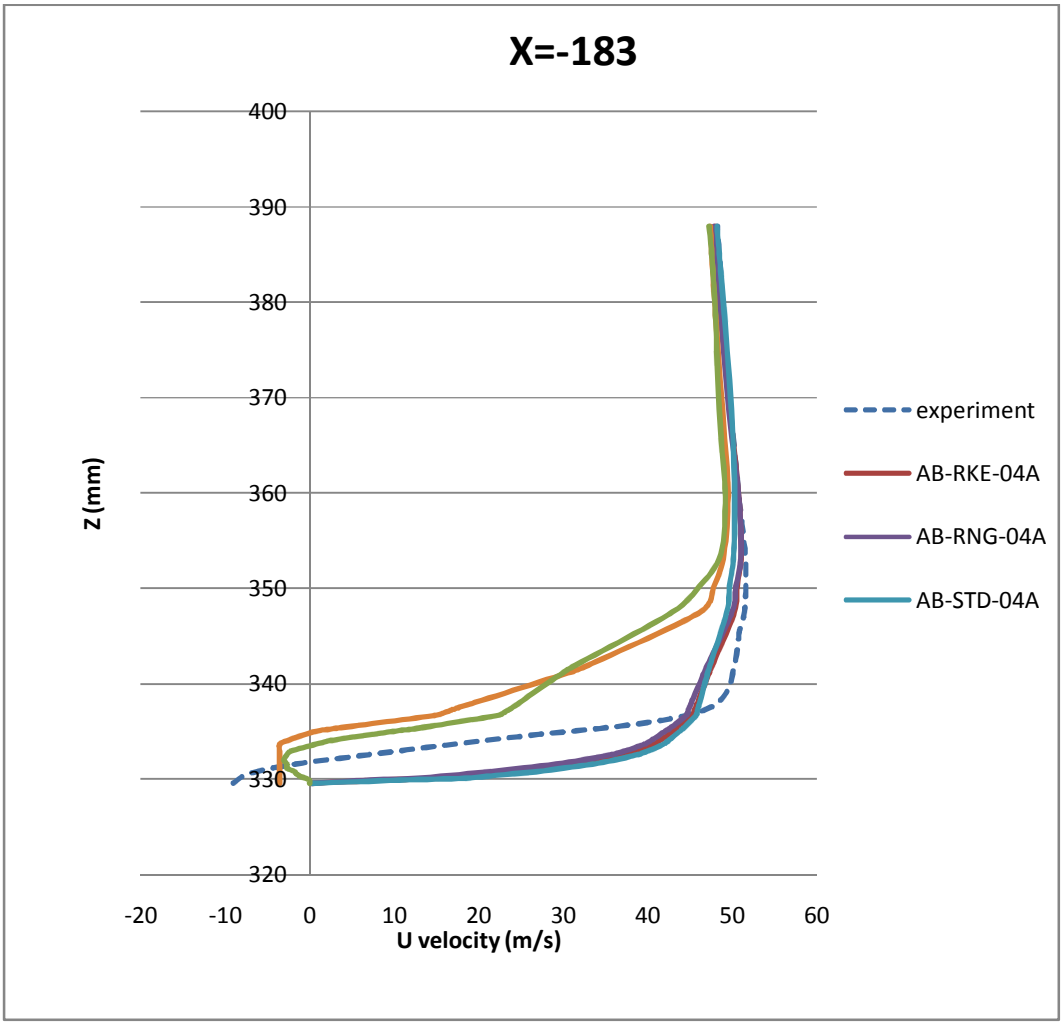

Figure C-4: U velocity profiles on symmetry plane (y=0) at x=-183.

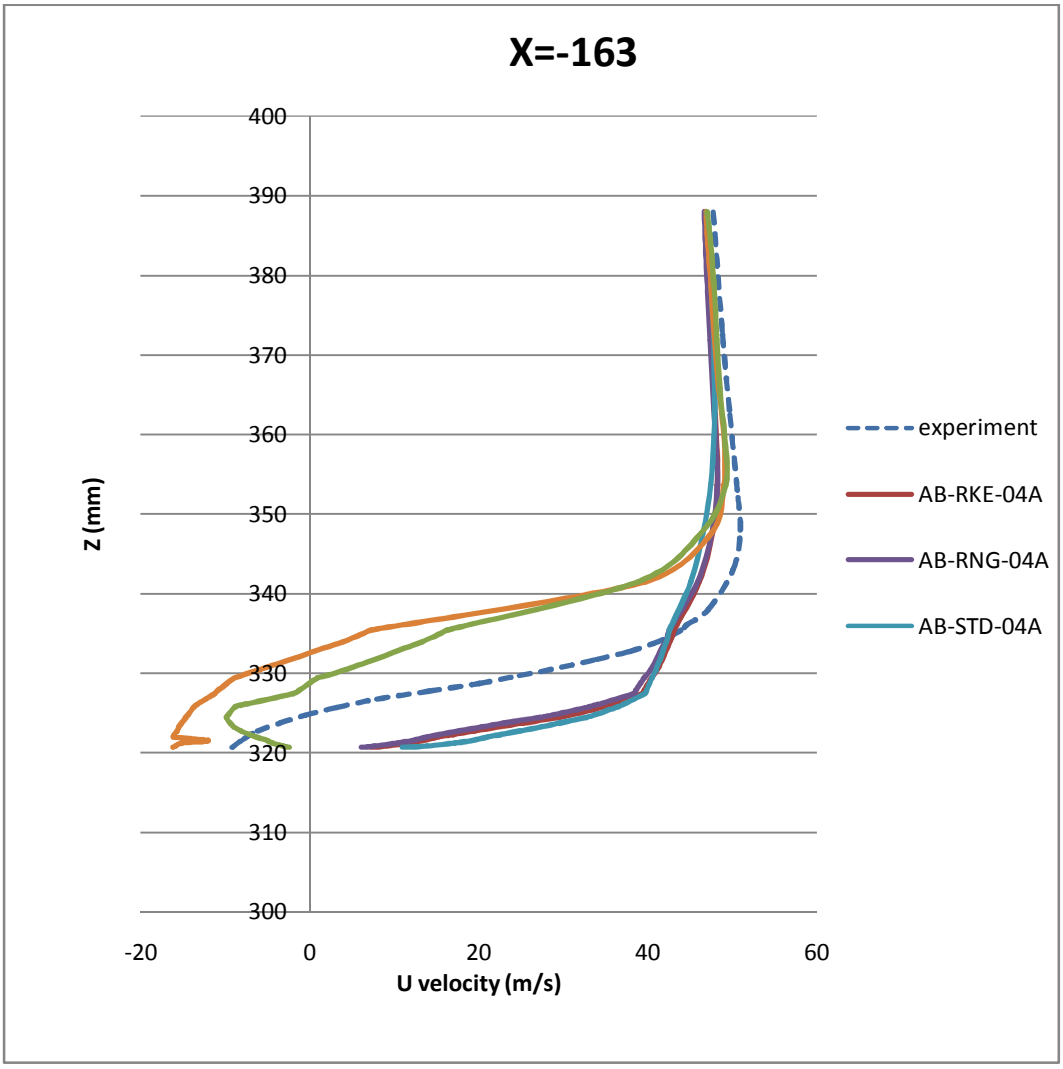

Figure C-5: U velocity profiles on symmetry plane (y=0) at x=-163.

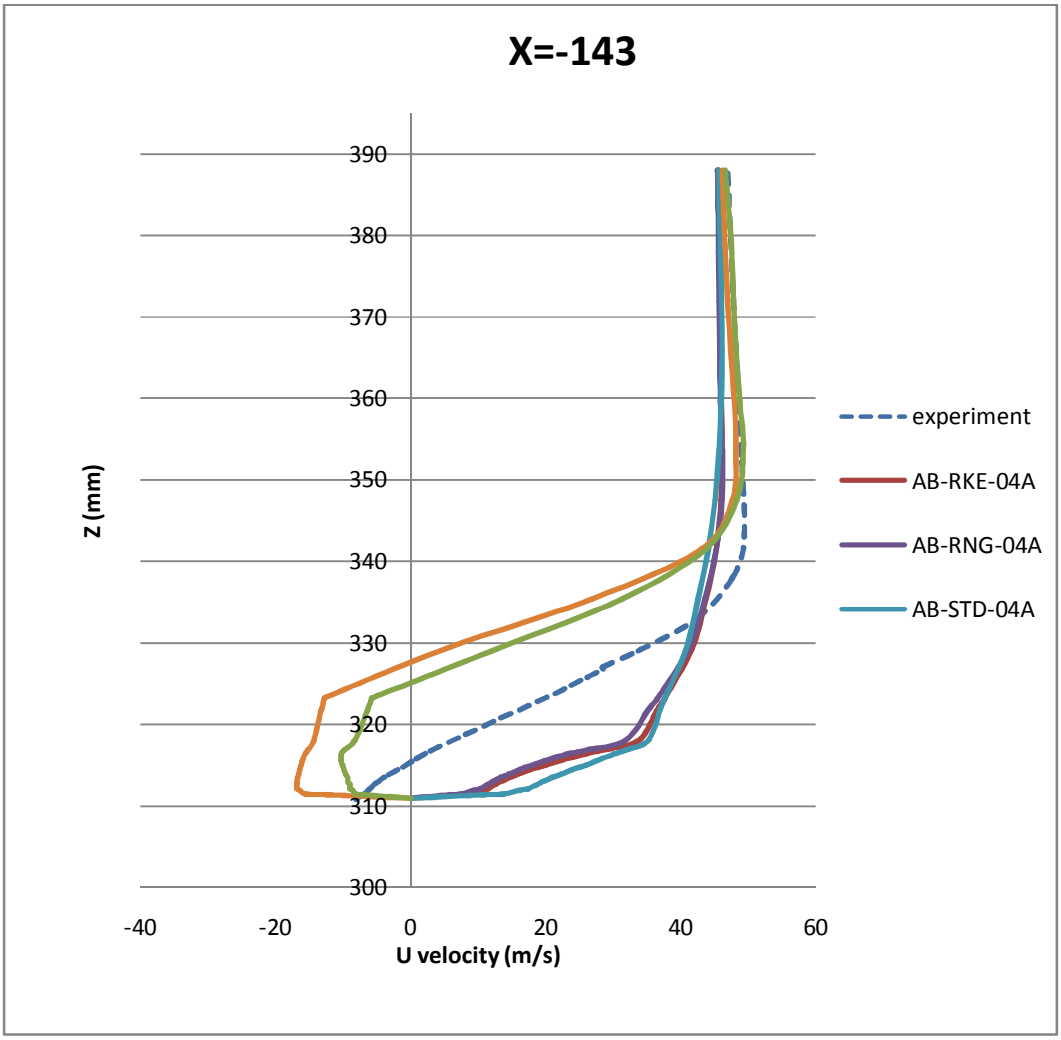

Figure C-6: U velocity profiles on symmetry plane (y=0) at x=-143.

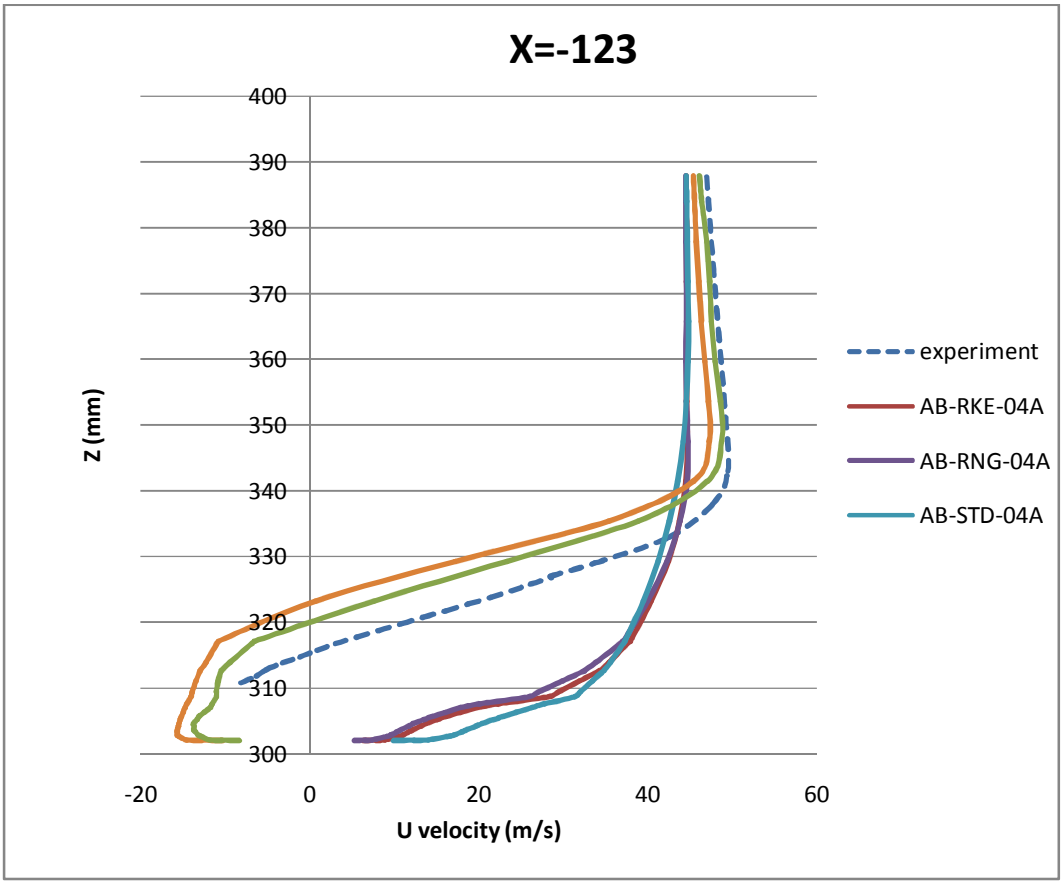

Figure C-7: U velocity profiles on symmetry plane (y=0) at x=-123.

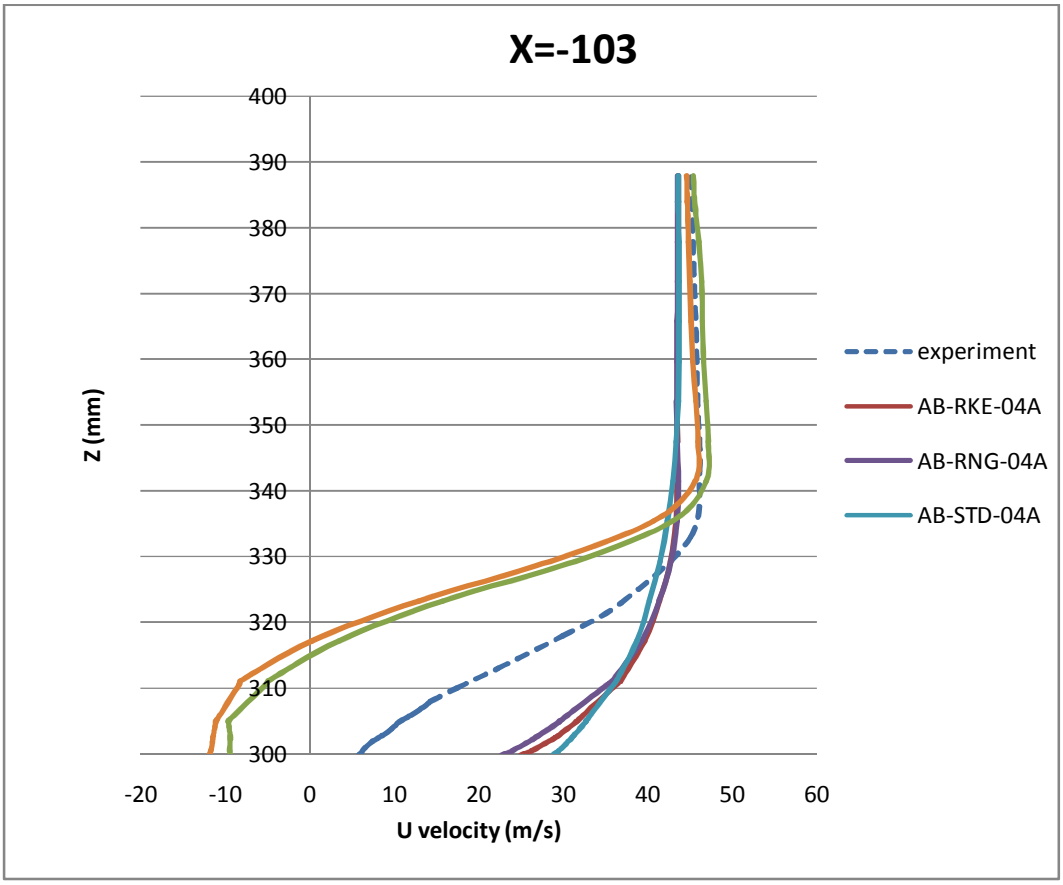

Figure C-8: U velocity profiles on symmetry plane (y=0) at x=-103.

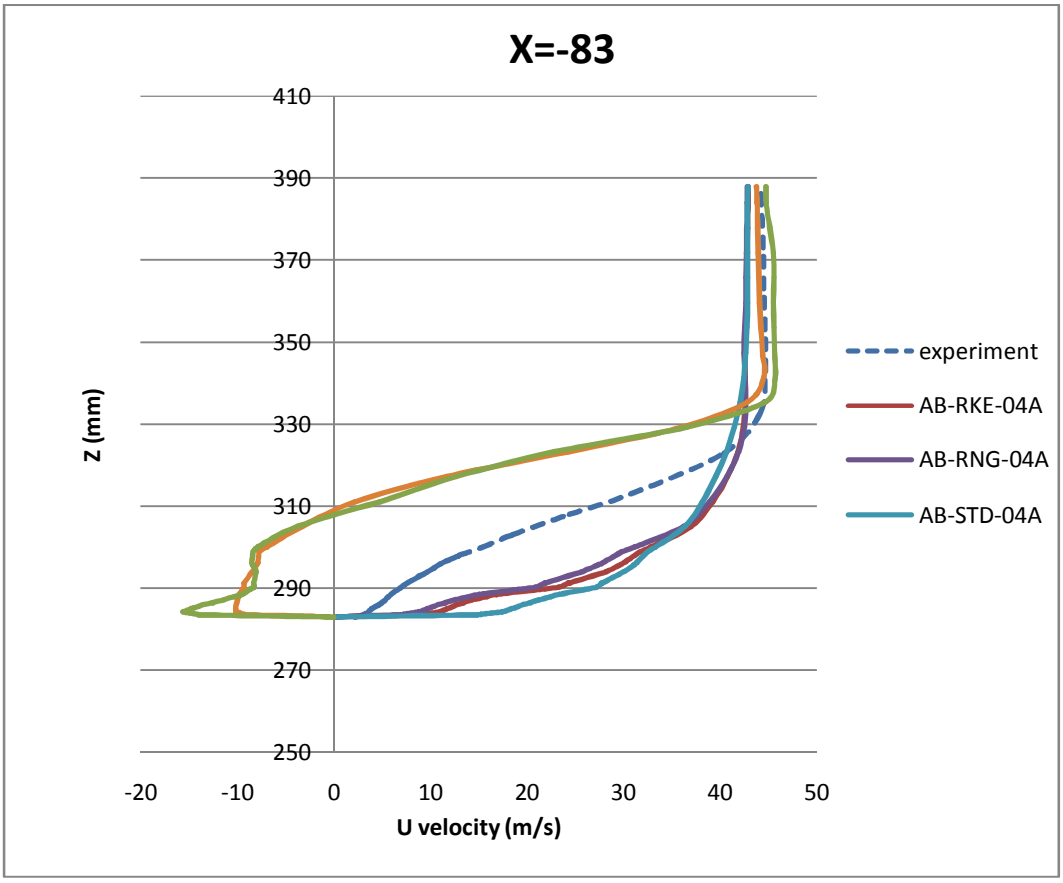

Figure C-9: U velocity profiles on symmetry plane (y=0) at x=-83.

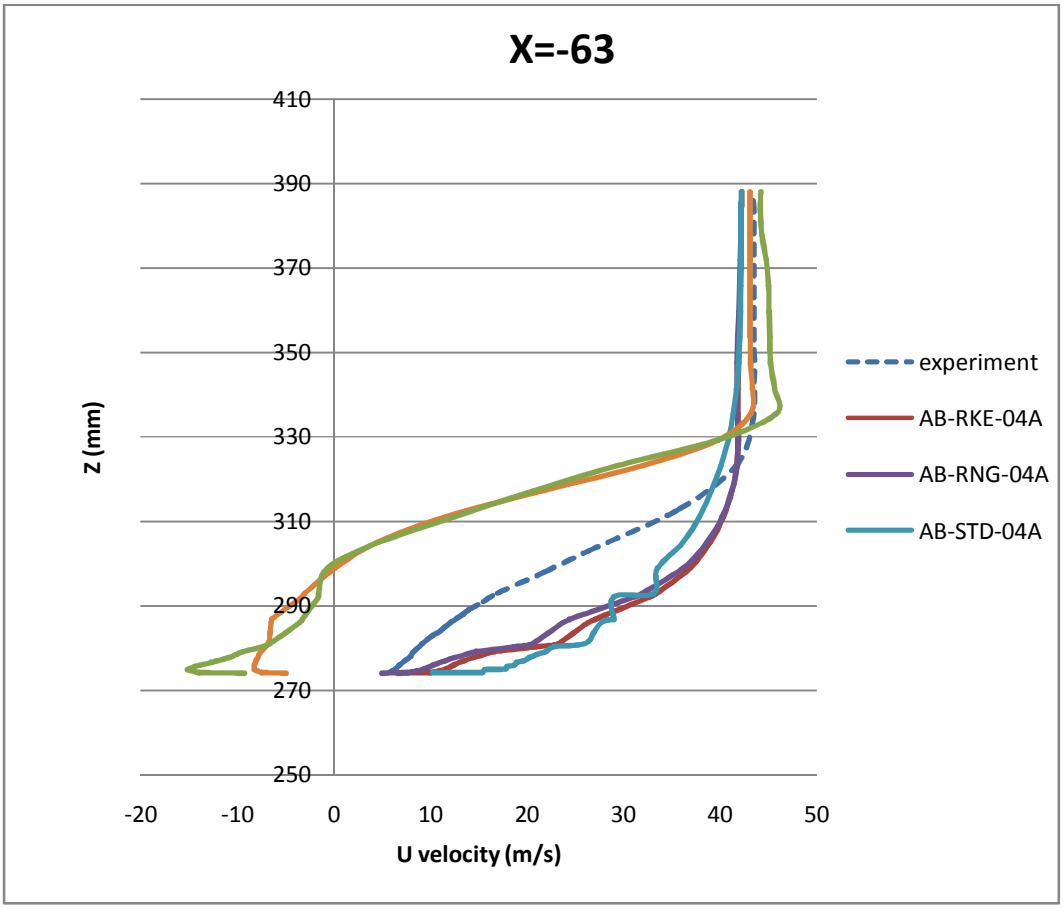

Figure C-10: U velocity profiles on symmetry plane (y=0) at x=-63.

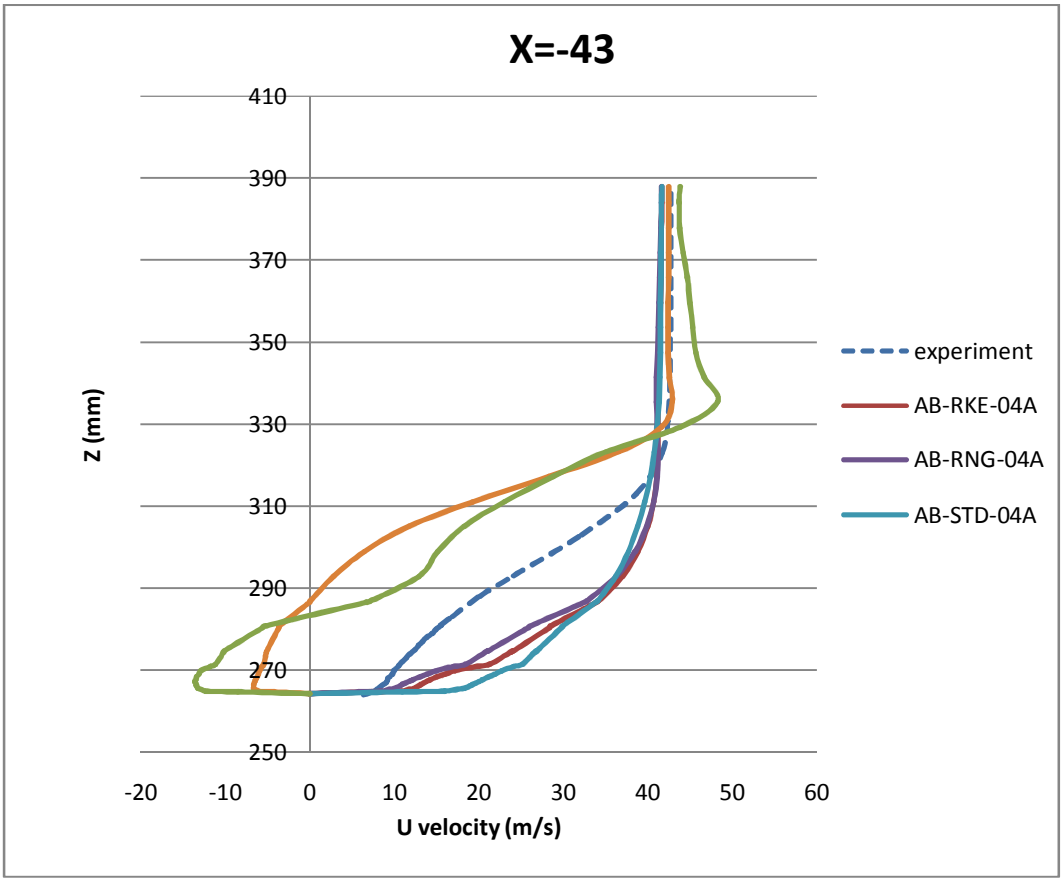

Figure C-11: U velocity profiles on symmetry plane (y=0) at x=-43.

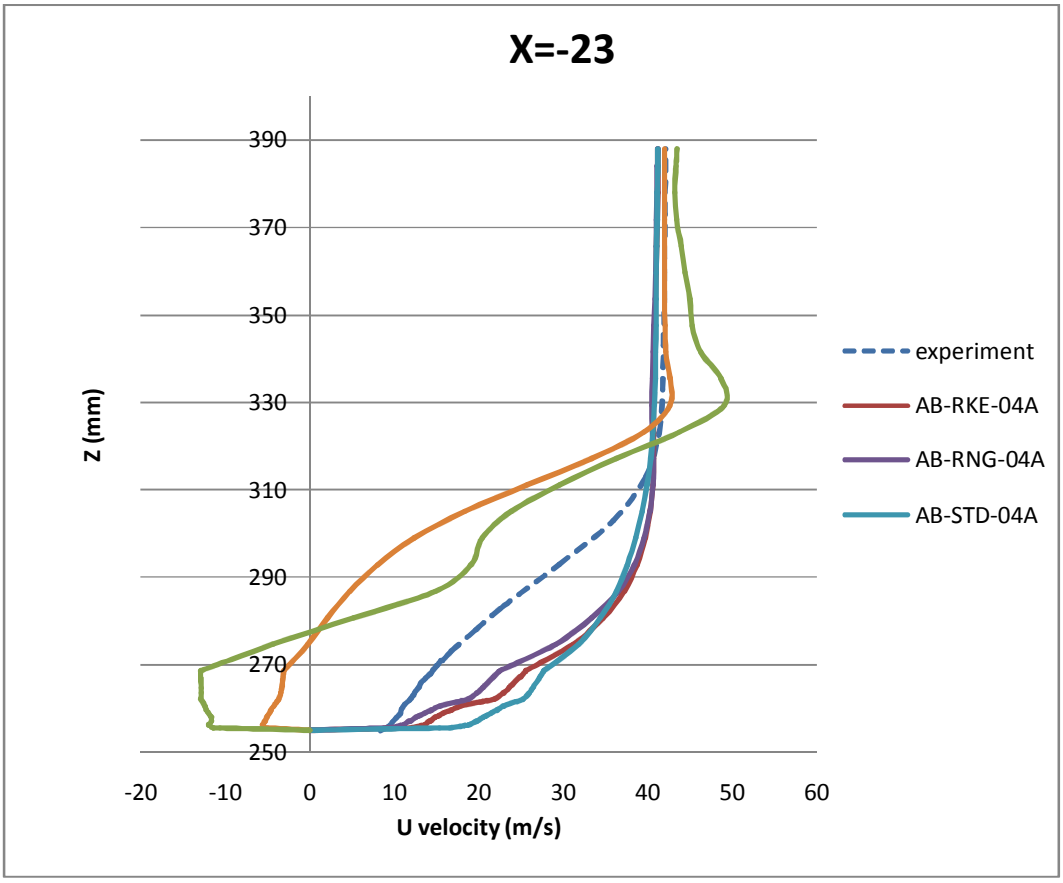

Figure C-12: U velocity profiles on symmetry plane (y=0) at x=-23.

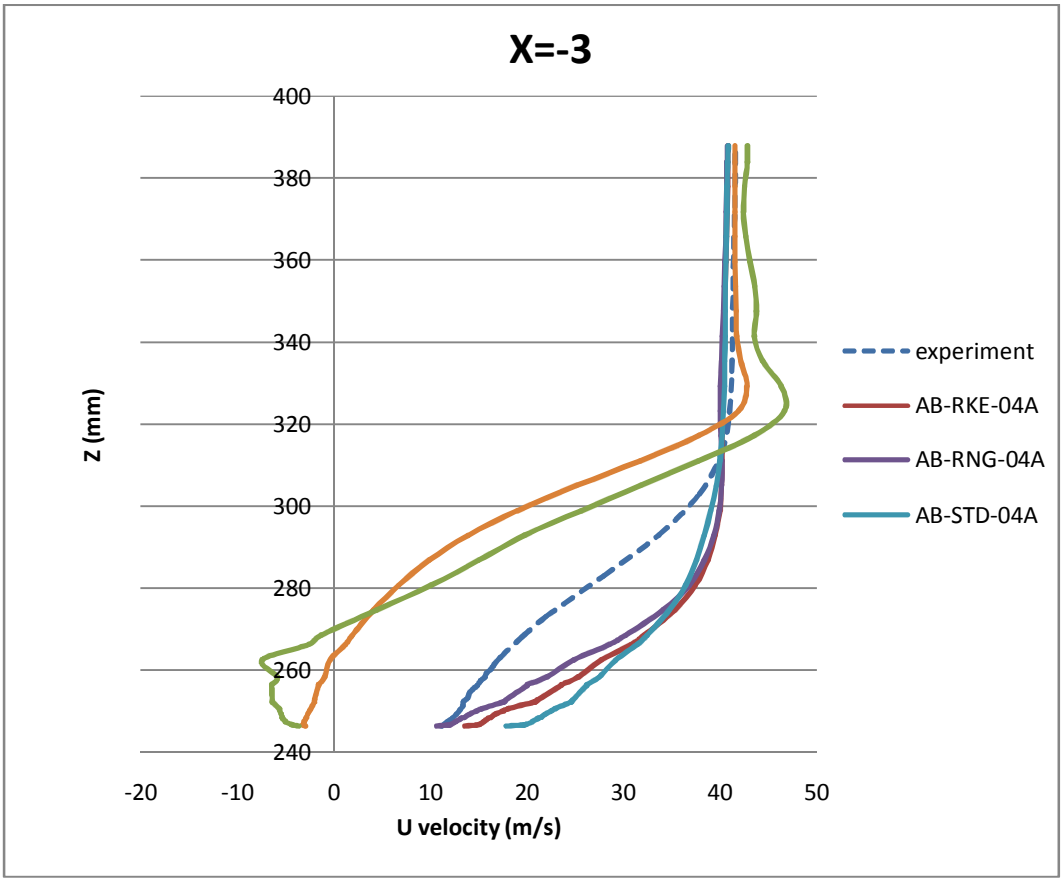

Figure C-13: U velocity profiles on symmetry plane (y=0) at x=-3.